

DESIGN OF INDUCTION COOKER FOR  
ALL TYPES OF METAL

by

Adriyan Manev

A thesis submitted to faculty of EEMC

Delft University of Technology

in partial fulfillment of the requirements for the degree of

Master of Science

Department of Electrical Sustainable Engineering

Delft University of Technology

June 2013

Adviser:

Ir. S.W.H. de Haan – TUDelft

Ir. F. Pansier – NXP Semiconductors



Copyright © 2013 NXP Semiconductors



# Abstract

The thesis presents a detailed design of 1.5kW induction cooker capable of heating all types of metals employed in the everyday cooking vessels. The design is based on newly developed control approach for resonant LLC DC-DC converters by NXP Semiconductors. The approach reduces the close loop transfer function of resonant converter to first order enabling control of resonant networks with very high quality factors. Additionally, the developed control idea regulates the power delivered to load in every cycle without the need of a power feedback. In that way the controller alleviates problems associated with power measurement and control in induction heating application, especially at high quality factors. The applicability of the control approach for induction heating application and resonant inverters is theoretically and practically verified by computer simulations and practical design. In the theoretical design possible approaches for estimation of required current ratings in the load, design of coil aiming for maximum efficiency and dimensioning of suitable resonant inverter are outlined. The output of theoretical investigation is used in the practical design of a complete induction cooking system. During the practical verification a power of 1kW was developed in aluminum cooking vessel which was limited by the maximum power ratings of the available DC power sources.



*To my Father and Mother*



# Acknowledgments

This project, and its successful completion, would not have been possible without the support of many people. I would like to thank to prof. Sjoerd W. H. de Haan and Frans Pansier for providing the thesis and allowing me that great opportunity to work on such topic as induction heating. I am very grateful for all their guidelines, help, support and encouragement which they gave me during the thesis.

Further, I would like to thank to the management of NXP Semiconductors for the opportunity which they gave me to share their knowledge, experience, facilities and the best available information on resonant converters. Also, to all members of the power and lightning laboratory, especially Humphrey de Groot, for their friendly attitude and all the help which they gave me during my practical design. To Hans Halberstadt for sharing his invention with me and the explanations and support which he gave me during simulations of the control idea.

Finally, I would like to thank to Radoslav Ralchev for providing me with his support and the components required for the successful completion of the project. To all my friends in Den Haag and Eindhoven who supported me during my entire master studies and helped me to successfully finish my thesis.



# Contents

<b>1</b>	<b>Introduction</b>	<b>1</b>
1.1	Overview of Metals Used in Cookware Appliance . . . . .	1
1.2	Induction Heating . . . . .	3
1.2.1	Induction Heating Basics . . . . .	3
1.2.2	Induction Heating System . . . . .	6
1.3	Problem Description . . . . .	8
1.3.1	Electrical Point of View . . . . .	9
1.3.2	Control Point of View . . . . .	9
1.3.3	Topological Point of View . . . . .	11
1.4	New Control Approach . . . . .	15
1.4.1	Description of the Patent . . . . .	16
1.5	Master Thesis Objective and Overview . . . . .	17
<b>2</b>	<b>Theoretical Background</b>	<b>19</b>
2.1	Influence of Frequency and Efficiency of Heating . . . . .	19
2.2	Coil Workpiece Interaction . . . . .	19
<b>3</b>	<b>Design and Calculations</b>	<b>23</b>
3.1	Preliminary Information . . . . .	23
3.2	Dimensioning of the Resonant Network . . . . .	23
3.2.1	Estimation of Required Workpiece Current . . . . .	23
3.2.1.1	Estimation of Workpiece Resistance . . . . .	24
3.2.1.2	Coil Design and Estimation of Switching Frequency . . . . .	26
3.2.2	Output of the Coil Design . . . . .	34
3.3	Dimensioning of the Inverter . . . . .	35
3.3.1	Calculation of Losses in Half Bridge Topology . . . . .	36
3.3.2	Full Bridge Topology . . . . .	41
3.3.2.1	Calculation of Snubber Capacitors . . . . .	44
3.3.2.2	Estimation of the Losses in the MOSFET . . . . .	45
3.3.2.3	Transformer Design . . . . .	46
3.4	Theoretical Efficiency of the Complete System . . . . .	51
3.5	Design Outputs . . . . .	52
<b>4</b>	<b>Simulation Results</b>	<b>53</b>
4.1	Simulation Setup . . . . .	53
4.2	Simulation Results . . . . .	56

<b>5</b>	<b>Practical Design</b>	<b>61</b>
5.1	Used Equipment . . . . .	61
5.2	Half Bridge Inverter . . . . .	62
5.2.1	Schematics and Practical Implementation . . . . .	62
5.2.2	Achieved Practical Results . . . . .	68
5.3	Full Bridge Inverter . . . . .	74
5.3.1	Schematics and Practical Implementations . . . . .	74
5.3.2	Achieved Practical Results . . . . .	76
5.4	Estimation of Injected Power in the Workpiece . . . . .	87
<b>6</b>	<b>Conclusions</b>	<b>91</b>
	<b>Appendix A</b>	<b>93</b>

# Chapter 1

## Introduction

The enormous advance of power semiconductors, digital electronics and digital signal processing, allowed the power electronics to become the dominant technology in many fields previously employing other means for power conversion and control. The flexibility which power electronics affords is not limited only to industrial applications, but is also widely employed in everyday home appliance.

One field of consumer electronics which attempts to benefit from power electronics is cooking appliance. Nowadays, the main and the most popular ways of food heating is either by employing indirect heating (electrical plates) or by burning fluids with high chemical energy such as natural gas. The main drawback of both approaches is the low efficiency which is reported to be 74.2% for smooth electric cooktops and 42% to 48% for conventional gas burners (53% for sealed burners) [1]. Additional drawback, in case of electrical plates, is the slow response due to heating of the interface body between the cooking vessel and the heating resistance.

The poor efficiency of the conventional food heating methods combined with the enormous advance of power semiconductors in recent years, gave a way for new areas of research and development. A new idea based on induction heating phenomena – that is inducing eddy currents in an electrically conducting material, was tested and proved to be very promising [2].

Presently, induction cooktops are well developed and produced world wide. The efficiency of induction cookers are as high as 90% [3] and surpass the conventional cooktops not only by efficiency, but also by allowing instantaneous adjustment of the heat, lack of hot surface after removal of the cooking vessel, safer and etc.. Unfortunately, present induction cookers are limited in heating only cooking vessels build from carbon steel. The main reason for this, is the low specific resistance and unity relative permeability ( $\mu_r \approx 1$ ) of the common metal alloys employed in production of cooking vessels. Contrary to them, the carbon steel exhibits higher specific resistance and  $\mu_r \gg 1$ .

### 1.1 Overview of Metals Used in Cookware Appliance

In the production of cookware appliance, mainly three type of metals are employed – namely, carbon steel, stainless steel and aluminum. The first one, carbon steel, have been used since long ago and was the main choice in the past. However, due to high chemical reaction of the iron with the food ions, different type of coatings (porcelain, glass or enamelware) must

be employed in order reaction to be prevented (Fig. 1.1(a)). However, once the integrity of the coating is violated the reaction between the food and the steel is unavoidable .

Less chemically reactive and one of the most preferred metal used for cookware, is the stainless steel. The combination of steel with chromium and nickel, produces a durable and corrosion resistant material which is considered by many as the best and safest choice for general use cookware. One drawback of the stainless steel, however, is its poor thermal conductivity (Table 1.1). This leads to uneven heat distribution and hot spots in the cooking vessel. The problem is eliminated by «sandwiching» aluminum plate between two layers of stainless steel (Fig. 1.1(b)). The extra operation, however, leads to higher cost and more complex manufacturing process.

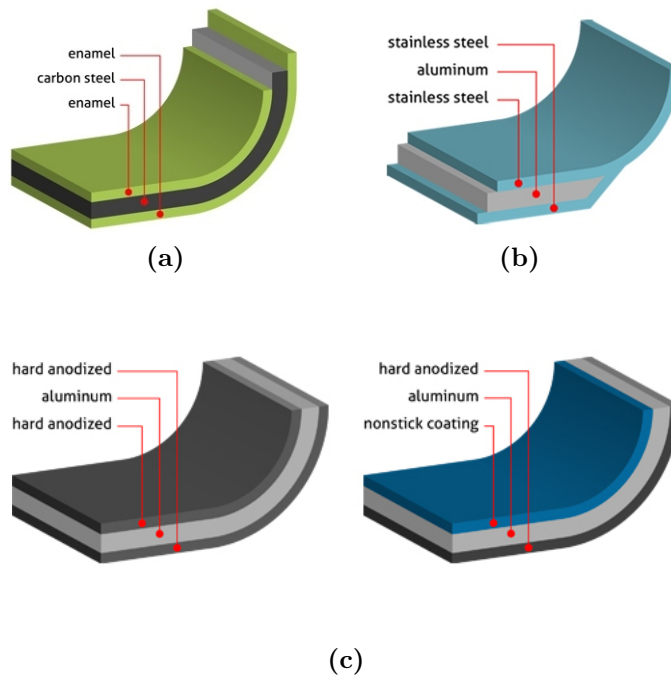


**Fig 1.1.** Design strategies of cookware appliance. (a) carbon steel, (b) stainless steel and (c) aluminum.

Owing to its excellent heat conductivity, low mass and low price, cookware based on aluminum is the most sold and used appliance worldwide. The aluminum, in fact, is easily scratched or pitted and is especially reactive to leafy vegetables and acid ingredient. Because of this a special coating, which in most of the cases is based on electrochemical anodization, is applied (Fig. 1.1(c)).

The physical properties of the alloys employed in cooking vessels are summarized in Table 1.1 [4] [5] [6] [7] [8] [9]. From the table it can be seen the superior thermal conductivity ( $k$ ) and low mass density ( $\rho$ ) of Aluminum 3004 (AL3004) which justifies its wide popularity. Also it can be seen the poor thermal conductivity of the Stainless Steel and the need of «sandwiching» with aluminum.

**Table 1.1.** Physical properties of alloys employed in cookware appliance.

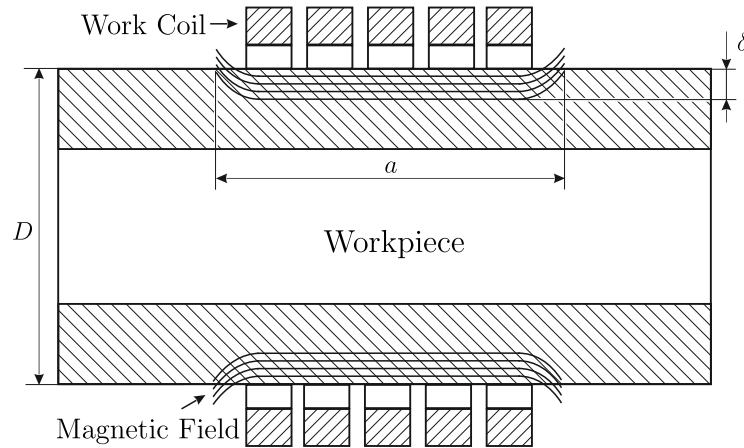
Alloy	Properties		
	Mass Density $\rho$ [kg/m <sup>3</sup> ]	Thermal Conductivity $k$ [W/(m · K)]	Specific Heat $c_p$ [J/(kg · K)]
Aluminum 3004	$2.72 \times 10^3$	163	893
Stainless Steel 304	$8.03 \times 10^3$	9.4	500
Grey Cast Iron	$7.06 \times 10^3$	53.3	490

## 1.2 Induction Heating

Induction heating have been employed in industry for many years. With the advance of the solid state switches, especially IGBTs, its popularity and role increased significantly and nowadays, the idea of energy transfer by induction, is widely employed.

### 1.2.1 Induction Heating Basics

The basic principle behind induction heating is generation of heat in an electrically conducting material (workpiece) by creation of an alternating electromagnetic field near it (Fig. 1.2). The alternating electromagnetic field is created by a coil (Work Coil) carrying an alternating current (AC). In that way, the AC electromagnetic field induces a voltage in the workpiece based on Faraday's law (1.7) which leads to circulating current in the workpiece (1.6). The circulating current in combination with the specific resistance of the material  $\rho_{wp}$  contributes to generation of Joule losses (heat)<sup>1</sup>:

**Fig 1.2.** Cut-away view of a pipe (workpiece) situated inside a coil carrying AC current.

<sup>1</sup>The induction heating relies on two phenomena for generating heat in the (workpiece) – Joule losses and hysteresis losses. Of these two the former is the dominant one while the latter contributes, to some extent, in the materials with magnetic properties. However, because of its small contribution and its disappearance after the Curie temperature, it is neglected in most of the applications [10].

$$P_{joule} = I^2 R_{wp}, \text{ [W]} \quad (1.1)$$

where:

$$R_{wp} = \rho_{wp} \frac{l}{A}, \text{ [\Omega]} \quad (1.2)$$

with

$$l = \frac{2D - \delta}{2} \text{ [m]} \quad (1.3)$$

$$A = a \times \delta, \text{ [m}^2\text{]} \quad (1.4)$$

$$\delta = \sqrt{\frac{\rho}{\pi \mu_r \mu_0 f}}, \text{ [m]} \quad (1.5)$$

and

$$I = \frac{E}{R_{wp}}, \text{ [A]} \quad (1.6)$$

with

$$E = -n \frac{d\Phi}{dt}, \text{ [V]} \quad (1.7)$$

where:

$P_{joule}$  – Joule losses [W];

$R_{wp}$  – workpiece's resistance [ $\Omega$ ];

$l$  – mean length of the workpiece surface through which the current circulates [m];

$D$  – outer diameter of the workpiece [m];

$A$  – workpiece's area in which currents circulate [ $\text{m}^2$ ];

$a$  – width of the workpiece perpendicular to  $l$  through which the currents flows [m];

$\delta$  – skin depth [m];

$\mu_r$  – relative permeability of the metal;

$\mu_0$  – permeability of the vacuum  $4\pi \times 10^{-7}$  [Wb/(A · m)];

$f$  – frequency [Hz];

$\rho$  – specific resistance of the metal [ $\Omega \cdot \text{m}$ ];

$E$  – induced voltage in workpiece [V];

$n$  – number of turns in the coil;

$d\Phi/dt$  – rate of change of the magnetic flux [Wb/s].

From (1.2) it can be seen that the resistance of the workpiece depends on physical dimensions ( $l$  and  $A$ ) the specific resistance of the material ( $\rho$ ) and its relative permeability ( $\mu_r$ ). For cooking vessels of fixed size but made of different metals, the physical dimensions are identical and the only difference is in  $\rho$  and  $\mu_r$  of the material. In that way the surface resistance of the vessels are dependable on the latter two parameters.

The electrical parameters of the alloys used for cooking vessels are tabulated on Table 1.2 [4] [5] [11] [6] [7] [8] [9]. From the table it can be seen that AL3004 exhibits unity permittivity

and the lowest specific resistance. This leads to surface resistance of 0.47m $\Omega$  at 100kHz. In comparison, the surface resistance of Cast Iron (ASTM40) is 9.30m $\Omega$  and is 19.7 times higher than the one of AL3004. The surface resistances are calculated for 1  $\times$  1 meters sample by:

$$R_{surface} = \rho \frac{l}{A}, [\Omega] \quad (1.8)$$

**Table 1.2.** Electrical properties of alloys employed in cookware appliance.

Alloy	Properties				
	Specific Res. @ 20°C $\rho$ [n $\Omega \cdot$ m]	Relative Permeability $\mu_r$ [H/m]	Skin depth @ 100kHz $\delta$ [mm]	Surface Res. @ 100kHz $R$ [m $\Omega$ ] <sup>(1)</sup>	Surface Res. related to AL3004
AL3004	41.6	1	0.32	0.13	1
SS 304	72	1.02	0.43	0.17	1.32
Grey Cast Iron	110	145.82 <sup>(2)</sup>	0.044	2.51	19.7

<sup>(1)</sup> for 1m  $\times$  1m sample

<sup>(2)</sup> @ B = 1T (ASTM40)

According to (1.1), for maintaining the amount of injected power unchanged, the lower surface resistance of AL3004 must be compensated by increase of the current  $\sqrt{19.7}$  times. Depending on the application this can entail several challenges as addresses in more detail further in the thesis.

The influence of the temperature on the specific and surface resistances at elevated temperature is tabulated in Table. 1.3 [12], [9] and [13]. From the table it can be seen that all alloys have positive temperature coefficient ( $\rho(T)$ ) – that is with the increase of the temperature resistance also increases. It can also be seen that the influence of temperature on  $\rho(T)$  of ASTM40 is lower that of AL3004. This leads to slight reduction of the difference in the surface resistances between the two alloys and can be considered as benefit. In both cases  $\mu_r$  is relatively unchanged [14][15].

**Table 1.3.** Electrical properties of alloys employed in cookware appliance at elevated temperature.

Alloy	Properties				
	Temperature Coefficient $\rho(T)$ [n $\Omega \cdot$ m/K]	Specific Res. @ 100°C $\rho(T)$ [n $\Omega \cdot$ m]	Increase Related to 20°C	Surface Res. @ 100kHz $R$ [m $\Omega$ ]	Surface Res. related to AL3004
AL3004	0.1	49.6	19.2%	0.15	1
SS 304	0.07	77.6	0.78%	0.18	1.2
ASTM40	0.05	114	0.36%	2.6	17.3

## 1.2.2 Induction Heating System

The AC current required for creation of electromagnetic field is supplied by an DC-AC inverter (Fig. 1.3). The inverter converts the low frequency current of the mains into a high frequency current, demanded by the induction heating process. Other components involved in induction heating systems are: rectifier, impedance matching transformer, compensating capacitor ( $C_r$ ) and control system (Fig. 1.3).

The rectifiers, inverters the main's AC voltage in to a constant DC voltage required for supplying the inverter. The role of transformer is to match the relatively low-voltage high-current (low impedance) requirements of the workpiece with the relatively high-voltage low-current output (high impedance) of the inverter<sup>2</sup>.

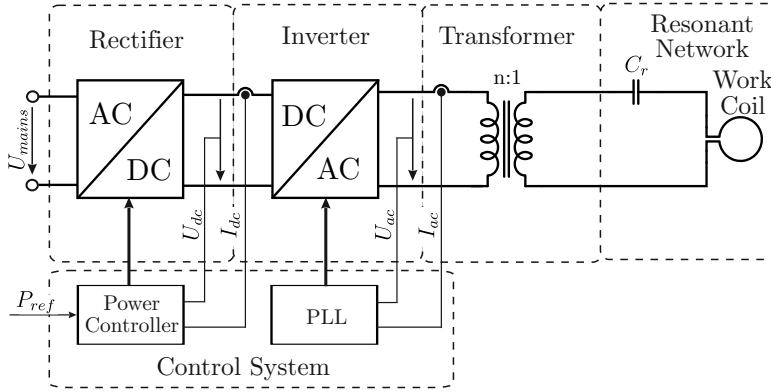


**Fig 1.3.** Induction heating system.

The resonant capacitor ( $C_r$ ) is used to compensate the reactive impedance of the coil. The compensation is necessary because at high frequencies the reactive impedance of the coil ( $X_L = 2\pi fL$ ) increase significantly in comparison to the workpiece resistance and reduces the power delivered to the load. Depending on the type of connection of the resonant capacitor across the coil two main types of compensation are distinguishable – serial and parallel (Fig. 1.4). The main difference between two network is that, in case of series resonant network, the voltage across reactive components ( $u_L$  and  $u_C$ ) is  $Q$  times higher that the input voltage  $u$  while, in case of parallel network, the current through reactive components ( $i_1$  and  $i_2$ ) is  $Q$  times higher that the current in the input terminals  $i$ . The quantity  $Q$  is the quality factor of the network and it is defined as [16]:

$$Q_s = \frac{U_L}{U} = \frac{U_C}{U} = \frac{IX_L}{IR_{wp}} = \frac{I}{IX_C R_{wp}} = \frac{X_L}{R_{wp}} = \frac{1}{X_C R_{wp}} \quad (1.9)$$

for series resonant network, and:

$$Q_p = \frac{I_1}{I} = \frac{I_2}{I} = \frac{UR_{wp}}{UX_L} = \frac{UR_{wp}}{UX_C} = \frac{X_L}{R_{wp}} = \frac{1}{X_C R_{wp}} \quad (1.10)$$

for parallel resonant network

where:

<sup>2</sup>The need and the type of the matching transformer, step-down or stet-up, depends on several factors. Discussion of this factors are beyond the scope of the master thesis.

- $Q_s$  – quality factor for series resonant network;  
 $U_L$  – voltage across the inductor (Fig. 1.4(a)) [V];  
 $U$  – voltage at input of the network [V];  
 $U_C$  – voltage across the capacitor [V];  
 $X_C = (\omega C)^{-1}$  [ $\Omega$ ];  
 $Q_p$  – quality factor for parallel resonant network;  
 $I_1, I_2$  – current in the inductors branch and current in the capacitors branch (Fig. 1.4(b)) [A];  
 $I$  – input current of the network [A].

The selection of the appropriate network depends on several factors such as resistance of workpiece, resonant frequency. the need of matching transformer etc.. However, roughly, the series resonant network is more suitable for load with high resistance (due to  $Q$  times higher voltage) while parallel network for loads with small resistance due to higher current in the network [17] [18].

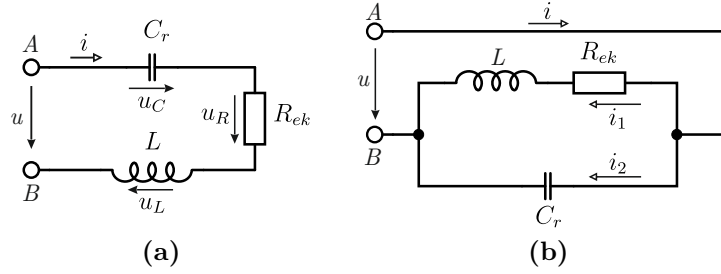


**Fig 1.4.** Basic resonant networks. (a) series and (b) parallel resonant networks [19] [16] and[16].

The connection of  $C_r$  and the coil forms a resonant network which at the resonant frequency ( $f_r$ ), eliminates completely the reactive impedance of the network leaving the inverter's output connected to the active resistance of the workpiece ( $R_{wp}$ ) [19] [16] [16]. The elimination of the reactive components can easily be explained with the help of Fig. 1.5. In Fig. 1.5(a) it can be seen that, in case of series resonant network, at resonant frequency the voltage across the capacitor and the voltage across the coil has the same magnitude ( $X_L = X_{C_r}$  and they are connected in series) but opposite signs. In that way the only remaining vector is the active voltage ( $U_a$ ) due to current flowing through  $R_{wp}$ . In Fig. 1.5(b) is presented the case for parallel resonant network where, this time, the currents ( $I_2$  and  $I_r$ ) are canceling each others. In the figure  $I_1$  is divided in reactive ( $I_r$ ) and active ( $I_a$ ) components.

One positive effect of using a resonant networks in induction heating system is their contribution to reduction of the switching losses. The later is achieved by turning-on the switches when the voltage across them is zero (ZVS) in case of series compensated network or turning them off when the current through the switches is zero (ZCS) – parallel compensated network [18]. In order this to happen, the controller keeps the switching frequency ( $f_{sw}$ ) of the inverter slightly above  $f_r$  ( $f_{sw} > f_r$ ) [20] [21]. In case of  $f_{sw} < f_r$  the switches no longer turn-on or turn-off at ZVS or ZCS. This leads to increase of the switching losses and sometimes failure of the switches as described in [17]). Because of this, this mode of operation is avoided in resonant inverters for induction heating applications.

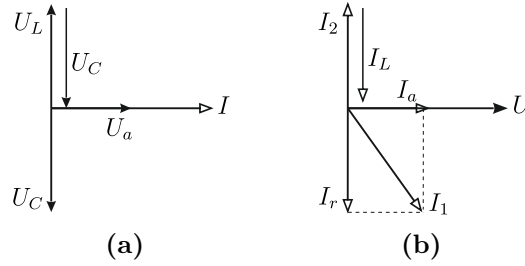


**Fig 1.5.** Vector diagrams of (a) series resonant network and (b) parallel resonant network.

The control system, in generally, consist of two controllers; the first one called Phase Locked Loop (PLL) which tracks  $f_r$  and controls  $f_{sw}$  so that the above condition is met ( $f_{sw} > f_r$ ) (detailed description of several approaches for tracing of  $f_r$  are given in [22] [23] [24]). The second one controls the power delivered to the load (workpiece) in accordance to specified reference value ( $P_{ref}$  Fig. 1.3). The power control can be achieved ether by changing the input voltage of the inverter ( $U_{dc}$  Fig. 1.3) as described in [25] or by changing the switching frequency as described in [26]. Further detail on both approaches are given in §1.3.2.

The inverter, depending on power requirements, can be either Class E (Fig. 1.6(a)) or Half Bridge (Fig. 1.6(b)) or Full Bridge (where the capacitors  $C_1$  and  $C_2$  from Fig. 1.6(b) are substituted by switches) [27]. The employment of only one switch, absence of matching transformer, small filtering capacitors (DC-link) in the input of the inverter, the simple control and the low power ratings ( $P < 1.5\text{kW}$ ) made Class E topology preferred one in the mainstream induction cookers. The Half Bridge topology is employed in cases when higher power ratings are required [27].

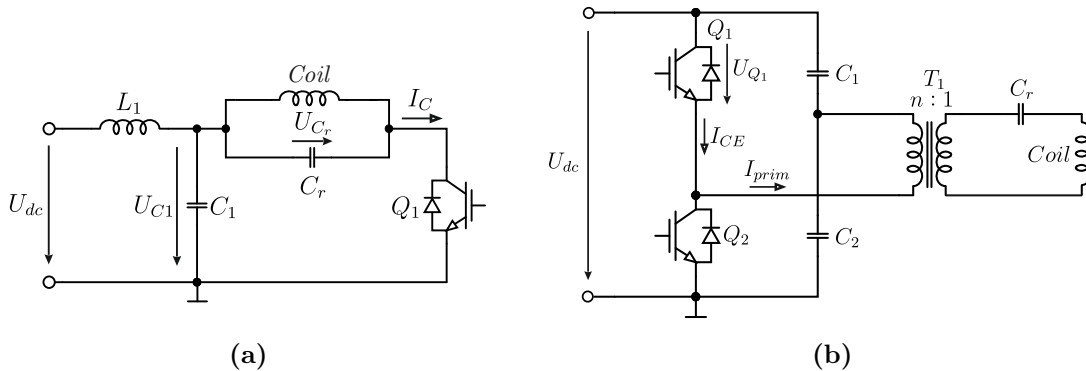


**Fig 1.6.** Inverter topologies used in mainstream induction cookers. (a) Class E, (b) Half Bridge [27].

### 1.3 Problem Description

As mentioned above, the main challenge in designing of an induction cooker for heating all types of metal is the low surface resistance of some of the alloys employed in production of

cookware. This leads to several issues as detailed below.

### 1.3.1 Electrical Point of View

The induction heating, as phenomenon relying on Joule losses, the low surface resistance means that for achieving the same amount of power losses in a vessel with low  $\rho$ , the current ratings must be increased in accordance to (1.1). As example, considering Table 1.2 and Table 1.3, in case of cooking vessel made of AL3004 and temperature of 100°C, the current must be increased  $\sqrt{17.3}$  times than in case of a vessel made of Cast Iron. This imposes a challenge in the design of efficient air cooled coil capable of carrying high frequency high currents.

Further, according to above, to keep the amount of power unchanged ( $P = UI$ ), the AC voltage supplied to the resonant network, in case of Cast Iron vessel, must be  $\sqrt{17.3}$  times higher than in case of AL3004. This leads to poor impedance matching in case a transformer without taps is employed. The poor impedance matching, on the other hand, leads to higher currents level in the primary side of the transformer and hence high switching and conduction losses in the switches.

One way of coping with the problem, unquestionably, would be by equalizing the resistances – that is by attaching a cast iron plate at the bottom of the aluminum and stainless steel vessels. However, this will require additional processing and will make the vessel a special one. Further, the thermal conductivity of the vessel will be influenced by the thermal conductivity of the attaches plate. This might decrease the efficiency of the vessel when employed with conventional cooking appliance ( $k$  in Table 1.1). Because of this, the approach is not considered here.

### 1.3.2 Control Point of View

The relation between the current/voltage in the resonant network and  $f_{sw}$  of the inverter for different values of  $R_{wp}$  ( $Q$ ) is shown in Fig. 1.7. From the figure it can be seen that with decrease of the resistance (increase of  $Q$  (1.9) and (1.10)) the change of the magnitude of the current/voltage ( $\Delta I/\Delta U$ ) which a given change of  $f_{sw}$  ( $\Delta f_{sw}$ ) will lead, increases. This means that in case of very low  $R_{wp}$ , a small change in  $f_{sw}$  will lead to high changes in the current or voltage (the power delivered to load) and imposes a challenge in the design of the power controller. The control of high  $Q$  network is further complicated by the fact that for achieving ZVS and ZCS (for reducing the switching losses)  $f_{sw} > f_r$ . In that case,  $L$  and  $C$  do not compensate each other completely and the open loop is from second order. The later easily can be shown by considering Fig. 1.8. In the figure is shown a typical series connection of capacitor, inductor and resistor in their Laplace forms. The circuit represent typical series resonant network used in induction heating and LLC DC-DC converters (Fig. 1.15(a)). Because in both cases the output quantity of interest is the power delivered to the load ( $R_{ek}$ ) for the transfer function can be written:

$$G(s) = \frac{P_{out}}{P_{in}} = \frac{I^2 R_{ek}}{I^2 \frac{1}{sC_r} + I^2 sL_{coil} + I^2 R_{ek}} = \frac{sC_r R_{ek}}{s^2 L_{coil} C_r + sC_r R_{ek} + 1} \quad (1.11)$$

From (1.11) it can be seen that the open loop transfer function contains terms from second order ( $s^2 L_{coil} C_r$ ). The differences in the step responses of first order (in case  $C_r$  is not present in Fig. 1.8) and (1.11) is presented in Fig. 1.9. From the figure it can be seen that second order system's output is oscillating which makes it more difficult to control.

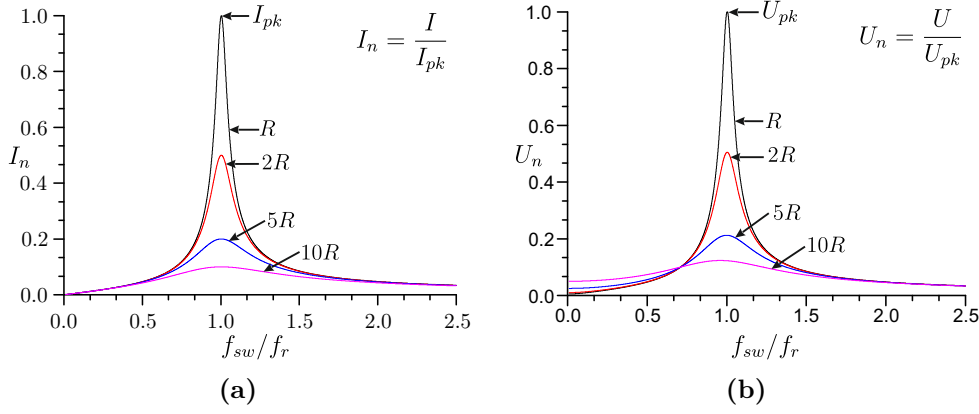


**Fig 1.7.** Relation of the normalized resonant network's current and voltage in function of normalized frequency for (a) series and (b) parallel resonant network.

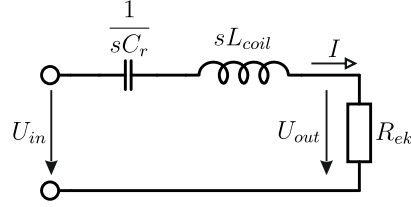


**Fig 1.8.** Series connection of RLC.

The oscillations, in case of second order system, are damped to zero because  $C_r$  blocks the DC component. As the latter is absent in the first order system the waveforms are set at value bigger than zero.

Additional complication in the control of induction heating resonant inverter emerge from the power sensing and controlling approaches. In resonant inverters, the power control is implemented either by sensing the DC power ( $P_{dc}$ ) at the input of the inverter (Fig. 1.3) or by sensing the AC power ( $P_{ac}$ ) at the output of the inverter. However, in both cases the reaction of the control system to power changes will be limited due to measurement of average DC current ( $I_{dc}$ ) in case of  $P_{dc}$  and time required for solving  $P_{ac} = U_1 I \cos \alpha$  in case of  $P_{ac}$ . The accumulation of all above factors contributes to instability of the control system and impose challenges in control of resonant inverter with high  $Q$  load such as aluminum cooking vessels [28] [29] [30] [31].

One way of increasing the stability of the systems is by reducing the close loop transfer function to first order. This can be achieved by implementing a control approach based on sensing some of the quantities of  $C_r$  or  $L_{coil}$ . In that way the component which is included in the control loop will be eliminated from the  $G(s)$  making the closed loop transfer function from first order.

The idea is employed in Class E inverters where for controlling the turn-off times of the switch the Coil's current is sensed (Fig. 1.10(a)) [32] [33]. There the zero voltage across the switch (time interval between  $0 - t_3$  and  $t_3 - 2\pi$  Fig. 1.10(b)) is sensed for turning-on of the switch ( $t_0$  and  $2\pi$ ). The switch is turned-off when the current in the coil reaches

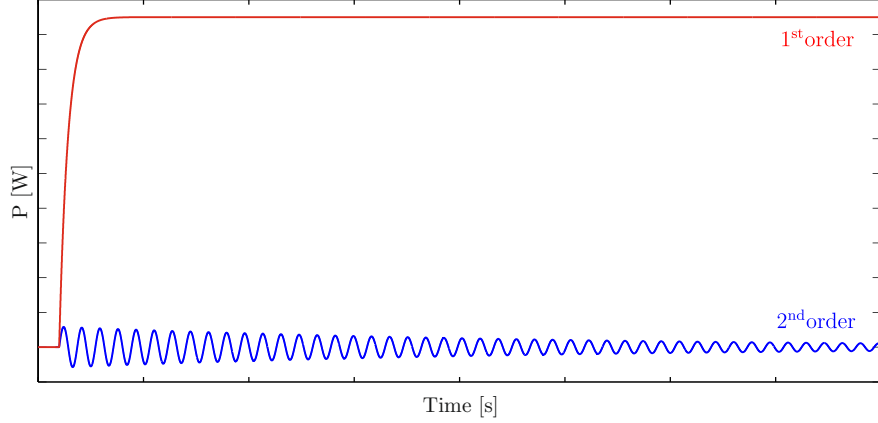


**Fig 1.9.** Step response of first and second order systems in case  $L_{coil} = 22\mu\text{H}$ ,  $C_r = 85\text{nF}$  and  $R_{ek} = 0.19\Omega$ .

the reference peak level ( $I_{C,pk}$ ) ( $t_2$  in Fig. 1.10(b)). The inclusion of the coil current in the control loop, eliminates the inductor from the close loop transfer function and makes the systems of first order.

The power regulation, in this case, is achieved either by varying the duty cycle of the switch ( $D = t_{on}/T$  Fig. 1.11(a)) – that is by varying  $I_{ref}$  (Fig. 1.10(a)) or by Pulse Density Modulation (PDM) (Fig. 1.11(b)) [34]. In the former approach, however, at lower levels of  $I_{C,pk}$ , the energy stored in coil at the moment of turn-off might not be sufficient to precharge  $C_{CE}$  and  $C_r$  and will lead to none zero voltage turn-on (Fig. 1.11(a)). That is why, power regulation based on PDM is mainly employed. The regulation is achieved by enabling the gate pulses of the switch ( $Q_1$  Fig. 1.10(a)) for certain period of time ( $t_{on,PDM}$  Fig. 1.11(b)), and disabling them for another period of time ( $t_{off,PDM}$ ). In that way the average power delivered to load is related to relation between  $t_{on,PMD}/(t_{on,PMD} + t_{off,PMD})$ .

### 1.3.3 Topological Point of View

In Fig. 1.10, a Class E inverters based on parallel resonant network is shown. The reason for this is that it is the preferred topology in induction cookers [35] [33]. The current in the parallel resonant network has a  $Q$  times bigger value than the input current supplied by the source. Because of this,  $R_{wp}$  has  $Q$  times larger value when referred to inverter's output terminals which allows elimination of the matching transformer. Additionally, at turn-on, contrary to series resonant network, the switch turns-on at ZVS and in that way preventing the discharge of the output capacitance of the switch ( $C_{CE}$  or  $C_{DS}$ ) through the switch.

However, the topology is impractical for high current ratings as in the case of low  $R_{wp}$ . The reason for this is the high voltages across the switch, which are reached at high currents. The voltage across the switch can be approximated from the power balance:

$$W_L = W_C \Rightarrow \frac{1}{2}Li_1^2 = \frac{1}{2}Cu^2, [\text{J}] \quad (1.12)$$

$$u_{CE} = i_1\sqrt{\frac{L}{C}} + U_{C_1}, [\text{V}] \quad (1.13)$$

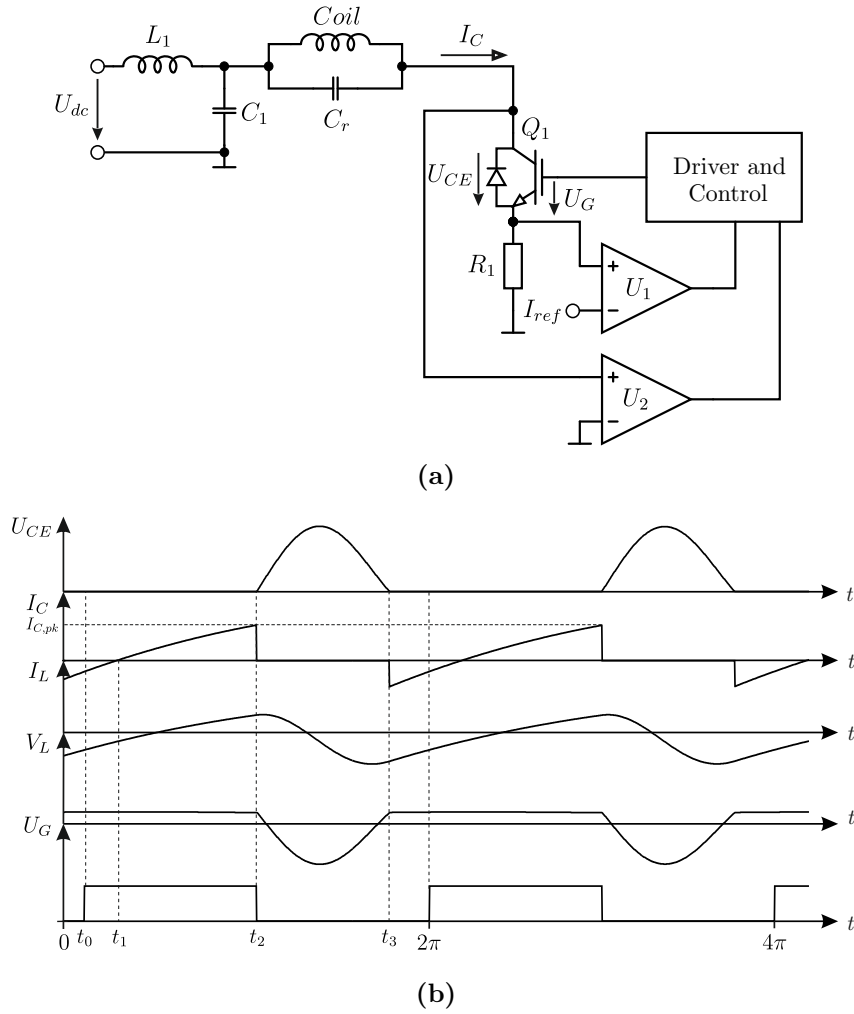


**Fig 1.10.** Class E inverter. (a) schematic and (b) typical waveforms.

Depending on the network and power requirements,  $u_{CE}$  can reach values above  $1kV^3$ .

Further the  $I_C$  has a triangular shape (Fig. 1.10(b)) which in case of high power ratings can reach very high peak values. Even though special type of IGBTs have been developed [36] [37] and are offered by most of power semiconductor manufacturers [38] [39] the switches are not designed to meet the demands for aluminum heating.

The problem is solved very elegantly in [40] by interleaving two Class E inverters, every-one with separate parallel resonant network switching at 20kHz (total 40kHz). The idea have been tested practically, by the authors, with copper, aluminum and stainless steel. However, in case of stainless steel, due to the higher specific resistance, the amount of injects power is reported to be reduced in comparison with the copper and aluminum.

Another attractive solution with interleaved Class E inverters is presented in [35]. The

<sup>3</sup> $U_{CE}$  is proportional to the current in the coil and the characteristic impedance of the network ( $\rho = \sqrt{LC^{-1}}$ )

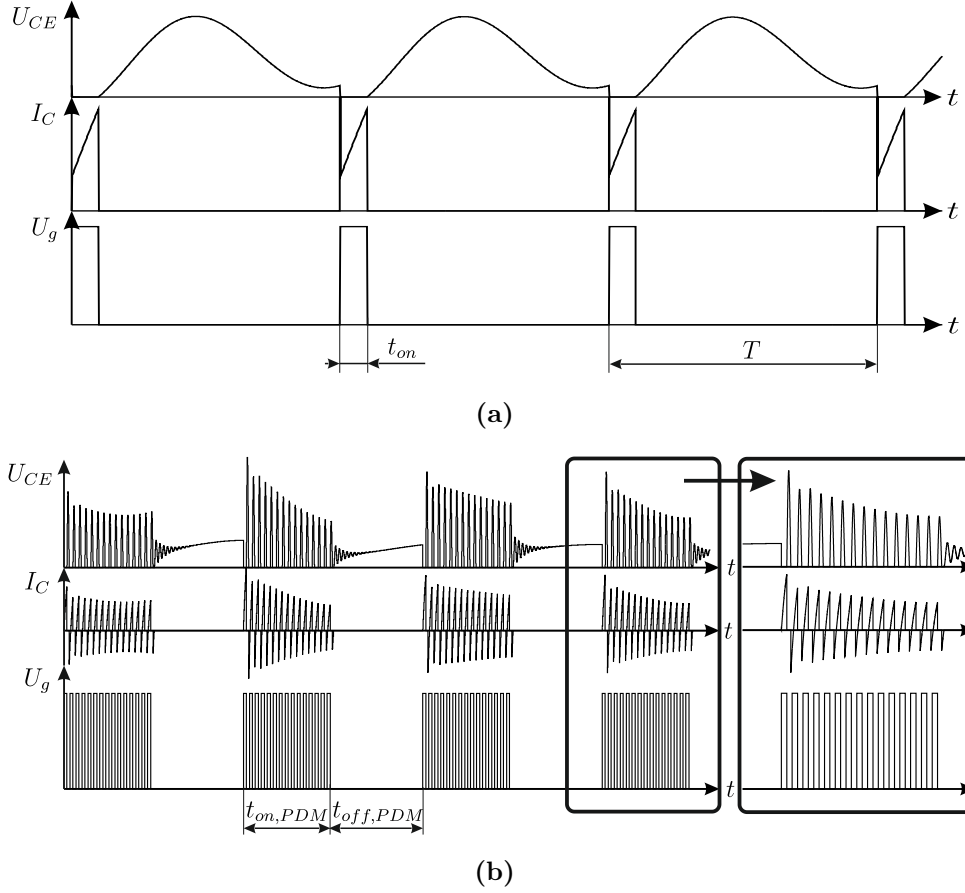


**Fig 1.11.** Power control in Class E inverters. (a) duty cycle control and (b) pulse density modulation.

authors based their approach on series resonant network which allows them to use only one coil and to change the value of  $C_r$  in order to increase/decrease the resonant frequency. In the case of iron cookware the  $f_{sw}$  is set to 50kHz and to 100kHz in case of aluminum and copper. In that way  $R_{wp}$  is also affected in accordance to (1.5), (1.8) and (1.4). The approach, however, requires a mechanical or bidirectional solid-state switches, capable of withstanding the high frequency current and additional logic for selection of appropriate  $f_r$  depending on the load.

With the Half Bridge topology (Fig. 1.6 (b)), due to employment of two switches, a better switch utilization is achieved and is preferred at higher power ratings. The topology, on the contrary of Class E, employs series resonant network [41] [42].

The control of the Half Bridge, as described above, is based on two controllers. The main challenges involved in design of PLL controller are linked to locating and maintaining the resonant frequency (Fig. 1.12). Possible PLL designs scenarios are described in [22] [23] [24].

The power control, in Half Bridge can be achieved either by varying the inverter's supply voltage ( $U_{dc}$ ) or by using frequency control.

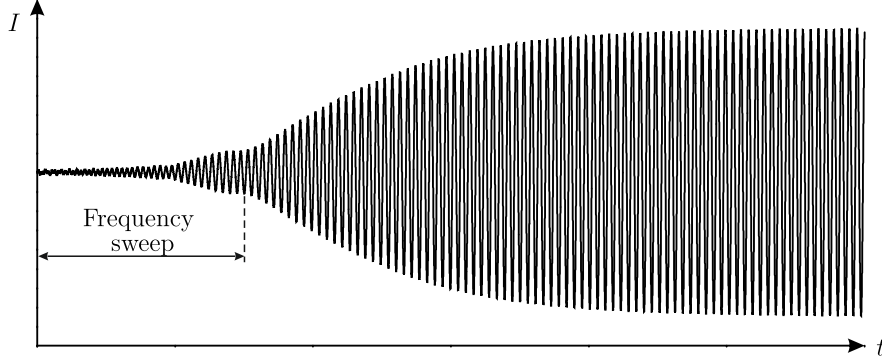


**Fig 1.12.** Starting up of series loaded resonant inverter with frequency sweep.

In case of power control based on varying  $U_{dc}$ , the fact that at  $f_{sw} \approx f_r$  the impedance of the resonant network is reduced to only the active resistance of the load is used. In that case for the power delivered to the load can be written:

$$P = \frac{U_1^2}{nR_{ek}} = nI_{prim}^2 R_{ek}, \text{ [W]} \quad (1.14)$$

with

$$U_1 = \frac{4}{\pi} \frac{U_{dc}}{\sqrt{2}}, \text{ [V]} \quad (1.15)$$

where:

- $n$  – turns ratio of the matching transformer;
- $R_{ek}$  – equals to  $n_{coil}R_{wp}$  with  $n_{coil}$  being number of turns of the coil [ $\Omega$ ];
- $U_1$  – fundamental harmonic of the inverters output voltage [V].

From (1.14) it can be seen that power can directly be influenced by  $U_{dc}$ . The variation of  $U_{dc}$  can be achieved either by step-down converter or controlled rectifier. In the former case, additional circuitry is required which further increases the size and the cost of the unit. In the controlled rectifiers, the rectifying diodes are substituted by Silicon Controlled Rectifiers (SCR). The topology, in general, is employed in high power applications. The employment in low power application is limited due to necessity of bulky EMI filters for filtering the high harmonics content which the rectifier injects in the grid and the large DC-link filter required for smoothing the voltage ripples at the  $U_{dc}$ .

For low power applications the frequency control is more suitable. The power regulation in this case is achieved by increasing  $f_{sw}$  above  $f_r$ . According to Fig. 1.7, increasing  $f_{sw}$  will decrease the magnitude of the current – hence the power.

Typical waveforms of frequency control are presented in Fig. 1.13. From the figure it can be seen that with the increase of  $f_{sw}$  the peak current ( $I_{C,pk}$ ) at which the switch is turn off also increases. This leads to higher switching losses. The problem, to some extent, is alleviated by connecting capacitors (lossless snubbers) in parallel to switches. In that case, however, if the energy stored in the inductive components is less than the energy

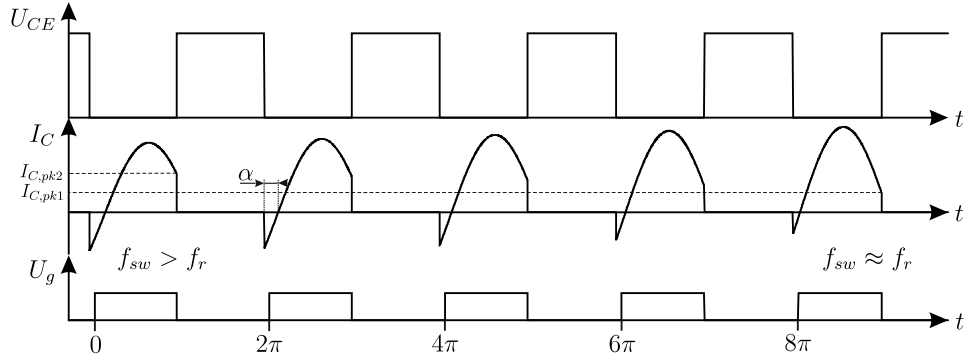


**Fig 1.13.** Typical waveform in case of frequency control.

required for precharge snubbers capacitors at the moment of turn-off, a none ZVS turn-on will occur which will lead to increased switching losses. In order the losses to be reduced, a valley detection must be introduced in the controller which control the turn-on time of the switches so that they are turned-on at the lowest possible  $U_{CE}$  (Fig. 1.14(b)).

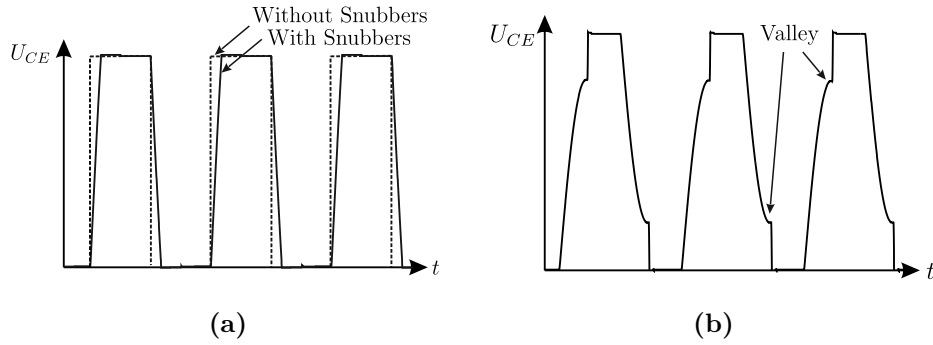


**Fig 1.14.**  $U_{CE}$  waveforms in case (a) with and without loss-less snubber and (b) none ZVS turn-on with valley detection.

In both control approaches, however, the close and open loop transfer function remains of second order. Further the power regulation is achieved by measuring  $P_{dc}$ . Because of this the control approaches are unsuitable for heating metals with low  $\rho$  such as aluminum.

## 1.4 New Control Approach

A newly developed and patented control approach for Half Bridge LLC DC-DC resonant converters by NXP allows for elimination of majority of drawbacks mentioned above and linked to Half Bridge. The idea reduces the closed loop transfer function to first order by sensing the voltage across the resonant capacitor. Further, the idea «predicts» the power delivered to the load every half cycle of  $f_r$  and turns-off the switches once the desired power is delivered to the load. In that way the idea does not require a feedback for power control. These features make the approach suitable for control of loads with high  $Q$ . Further, the idea performs a PLL and detects the resonant frequency immediately, eliminating the need

for frequency sweep and the problem associated with it (Fig. 1.12). Additionally, in the designed Integrated Circuit (IC) several features such as Valley detection, Pulse Density Modulation and sensing the primary current, aiming for increasing the efficiency, stability and reducing switching losses, are also implemented.

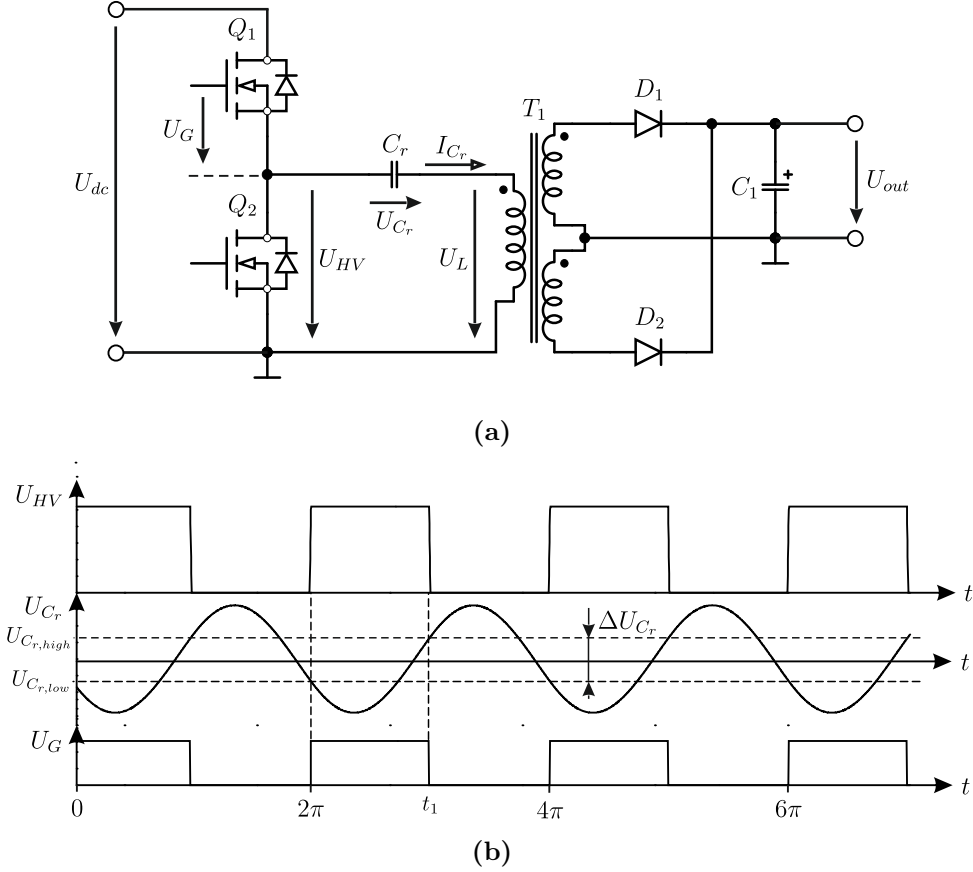


**Fig 1.15.** LLC DC-DC resonant converter. (a) schematic and (b) typical waveforms.

#### 1.4.1 Description of the Patent

The schematic of LLC DC-DC resonant converter and typical waveforms are shown on Fig. 1.15. According to Fig. 1.15 for the active power delivered to the output, in case of Half Bridge, can be written:

$$P = U_{dc}I_{dc} = U_{dc}fdq = U_{dc}fC_r\Delta U_{c_r}, \text{ [W]} \quad (1.16)$$

where:

$dq$  – amount of changed charge [C];

$\Delta U_{c_r}$  – shown on Fig. 1.15 [V].

From (1.16) the turn-off time ( $t_1$  in Fig. 1.15(b)) for the upper switch ( $Q_1$ ) is when  $U_{C_r} > 1/2\Delta U_{C_r}$  and for the lower switch ( $Q_2$ ) when  $U_{C_r} < 1/2\Delta U_{C_r}$ . In that way by tracking  $U_{C_r}$  the switches will be turned-off precisely when the required power has been delivered to the load. The inclusion of  $U_{C_r}$ , as a feedback signal in power regulation, removes  $C_r$  from the close loop transfer function and makes the system of first order. This makes the controller stable when connected to high  $Q$  resonant networks.

## 1.5 Master Thesis Objective and Overview

The objective of the master thesis is the possible employment of the developed control approach for control of induction cooking plates for all types of metals to be investigated. The applicability of the idea, initially, is tested by computer simulations. After achieving successful results, a practical verification is carried out by design of a 1.5kW prototype based on the developed control approach and integrated into an Integrated Circuit (IC).

The steps followed during the design are organized in the master thesis in the following way:

- In **Chapter 2** is given further theoretical background required for understanding some of the steps made during the theoretical design;
- **Chapter 3** contains the theoretical design starting with investigation of the required current in the workpiece for generation of 1.5kW Joule losses, followed by coil design and concluded with theoretical calculations of the resonant inverter based on estimated currents;
- In **Chapter 4** are presented a summary of the simulation results, achieved practical results and observed phenomenons;
- The conclusion of the master thesis is presented in **Chapter 5**;
- In **Appendix A** are given all source codes used in calculations, plotting and simulations.



## Chapter 2

# Theoretical Background

### 2.1 Influence of Frequency and Efficiency of Heating

According to (1.5) frequency influences the depth at which current flow and in that way  $R_{wp}$ . An increase of the frequency leads to decrease of the depth of penetration and hence increases  $R_{wp}$ . The benefit of increasing the frequency, however, is justified to certain value after which the benefit is no more pronounced. The reason for this is that with increase of the frequency the proximity effects in the coil start to play significant role. For certain process or application, the appropriated frequency is selected depending on the requirements. In cases when the efficiency of the systems is the most important, such as in melting applications, the deciding factor is the efficiency of heating. In case when the frequency is the most important factor, such as hardening applications, the efficiency of heating is ignored. As the aim of the master thesis being achieving the highest possible efficiency, the efficiency of heating is used as decisive factor.

The efficiency of heating is defined as the ratio of the delivered power to the workpiece to the power supplied to the coil or:

$$\eta_{heating} = \frac{I_{coil}R_{ek}}{I_{coil}R_{coil} + I_{coil}R_{ek}} = \frac{R_{ek}}{R_{coil} + R_{ek}} \quad (2.1)$$

where:

- $I_{coil}$  – current in the coil [A];
- $R_{ek} - R_{wp}$  referred to the coil side (see §2.2) [ $\Omega$ ];
- $R_{coil}$  – is the AC resistance of the coil [ $\Omega$ ].

### 2.2 Coil Workpiece Interaction

The system of coil and workpiece in induction heating can be represented as a linear transformer (Fig. 2.1(a)). The coil represents the primary side of the transformer with number of turns equal to the number of turns of the coil ( $n$ ) and the secondary side is represented by workpiece as one turn loaded by  $R_{wp}$ . In that way  $R_{wp}$  can be represented with an equivalent resistance ( $R_{ek}$ ) in series with the coil (Fig. 1.4) given by:

$$R_{ek} = n^2 k R_{wp} \quad (2.2)$$

where:

- $n$  – is the number of turns in the coil;
- $k$  – is the coupling between the coil and workpiece.

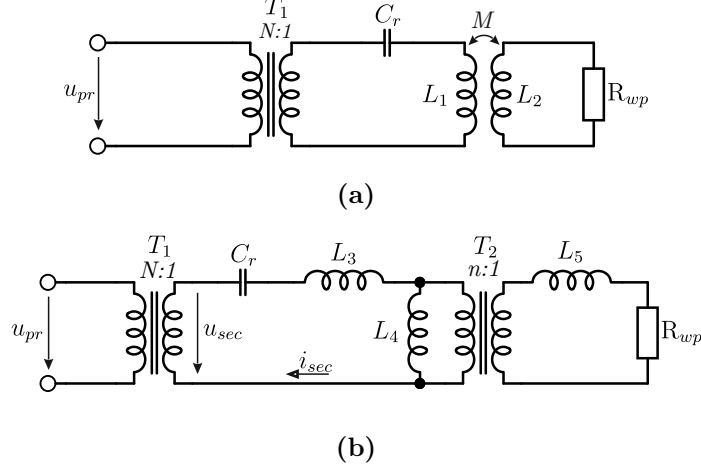


**Fig 2.1.** Equivalent schematics. (a) basic representation, (b) detailed representation.

A more detailed representation of the interaction is shown on Fig. 2.1(b). From the figure, in case of no load, for the Kirchoff's law can be written [43]:

$$\frac{du_{sec}}{dt} = (L_3 + L_4) \frac{d^2 i_{sec}}{dt^2} + R_{paras} \frac{di_{sec}}{dt} + \frac{1}{C_r} \quad (2.3)$$

with characteristic equation:

$$p^2 (L_3 + L_4) + pR_{paras} + \frac{1}{C_r} = 0 \quad (2.4)$$

and roots:

$$p_{1,2} = -\frac{R_{paras}}{2(L_3 + L_4)} \pm \sqrt{\left(\frac{R_{paras}}{2(L_3 + L_4)}\right)^2 - \frac{1}{(L_3 + L_4)C_r}} \quad (2.5)$$

where:

$R_{paras}$  – parasitic resistance of the coil and the secondary winding of  $T_1$  (not shown on Fig. 2.1(b)) [ $\Omega$ ].

From (2.5) it can be seen that when  $(R_{paras}/2(L_3 + L_4))^2 < 1/(L_3 + L_4)C_r$ ,  $C_r$  will resonate with  $L_3$  and  $L_4$  ( $L_1 = L_3 + L_4$ ).

In case a load is present (2.3), (2.4) and (2.5) become:

$$\frac{du_{sec}}{dt} = (L_3 + L_5) \frac{d^2 i_{sec}}{dt^2} + (R_{paras} + R_{ek}) \frac{di_{sec}}{dt} + \frac{1}{C_r} \quad (2.6)$$

$$p^2 (L_3 + L'_5) + p(R_{paras} + R_{ek}) + \frac{1}{C_r} = 0 \quad (2.7)$$

$$p_{1,2} = -\frac{(R_{paras} + R_{ek})}{2(L_3 + L'_5)} \pm \sqrt{\left(\frac{(R_{paras} + R_{ek})}{2(L_3 + L'_5)}\right)^2 - \frac{1}{(L_3 + L'_5)C_r}} \quad (2.8)$$

where:

$L'_5 = n^2 L_5$  – leakage inductance of the load referred to primary side of  $T_2$  [H].

From (2.8) it can be seen that when roots are complex,  $C_r$  will resonate with  $L_3$  and  $L'_5$ . In (2.6)  $L_4$  is eliminated because at resonant frequency  $R_{ek} \ll \omega L_4$  and shunts  $L_4$ .

The values of inductances can be found with following equations [44]:

$$L_3 = L_1 - M \text{ [H]} \quad (2.9)$$

$$L_4 = M \text{ [H]} \quad (2.10)$$

$$L_5 = L_2 - M \text{ [H]} \quad (2.11)$$

$$M = k\sqrt{L_1 L_2} \text{ [H]} \quad (2.12)$$

where:

$k$  – coupling between  $L_1$  and  $L_2$ .

The coupling  $k$  depends on the difference in the sizes of the coil and the workpiece and the distance between them [45]. An approximate value of  $k$  can be obtained by [46]:

$$k = \sqrt{\frac{L - L_{sh}}{L}} \quad (2.13)$$

where:

$L$  – value of the primary inductance ( $L_1$  Fig. 2.1(a)) when the secondary is open (the coil's inductance when no load is present) [H];

$L_{sh}$  – value of the primary inductance when the secondary is short circuited (the coil's inductance when load is present) [H].



# Chapter 3

## Design and Calculations

### 3.1 Preliminary Information

In the following chapter the theoretical design of the induction cooker is presented. The design starts with an estimation of current requirements in the workpiece for achieving the desired power. After that the coil design is considered and one possible solution is presented. The chapter is concluded with dimensioning of the resonant inverter and calculation of the efficiency of the system.

The starting parameters for the design are:

- $P_{out,min} = 200\text{W}$ ;
- $P_{out,max} = 1.5\text{kW}$ ;
- $V_{line} = 230\text{V} \pm 10\%$ ;
- Cookware materials in accordance with Table 1.1 and Table 1.2;
- Coil of planar type in accordance with the currently produced iron cookers with outer diameter of 220mm in accordance with the most commonly used cookwares and inner diameter of 40mm.
- Frequency range between 10kHz and 500kHz limited by IC.

### 3.2 Dimensioning of the Resonant Network

#### 3.2.1 Estimation of Required Workpiece Current

The required current in the workpiece for generation of 1.5kW Joule losses can be approximated in two ways – by FEM simulation or analytical calculations. As the aim of the master thesis not being precise calculation and investigation of coil workpiece interaction, a simple analytical approach is adopted. The approach gives sufficiently accurate results for initial selection of power components, resonant frequency and evaluation of the control system.

### 3.2.1.1 Estimation of Workpiece Resistance

An arrangement of a coil and exemplary cooking vessel is shown on Fig. 3.1. In the presented case the workpiece resistance ( $R_{wp}$ ) can be calculated by:

$$MCP = \pi \frac{d_1 + d_2}{2}, \text{ [m]} \quad (3.1)$$

from here the resistance is:

$$R_{wp} = \rho \frac{MCP}{w\delta}, \text{ [\Omega]} \quad (3.2)$$

with:

$$w = \frac{d_1 - d_2}{2}, \text{ [m]} \quad (3.3)$$

where:

- $MCP$  – Mean Current Path [m];
- $d_1$ – the outer diameter of the coil (Fig. 3.1) [m];
- $d_2$ – the inner diameter of the coil (Fig. 3.1) [m];
- $\rho$  – the specific resistance of cooking vessel's material [ $\Omega \cdot \text{m}$ ];
- $w$  – the width of one side of the coil (Fig. 3.1) [m];
- $\delta$  – the skin depth (1.5) [m].

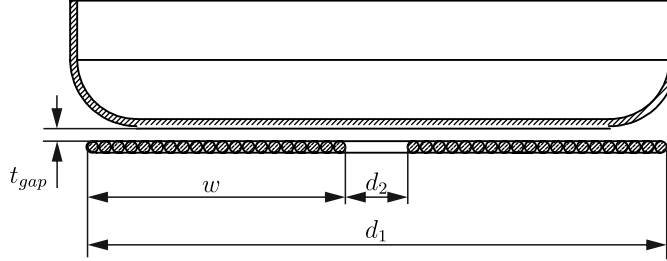


**Fig 3.1.** Designation of the coil and cooking vessel.

In (3.1) it is assumed that the current is flowing only in the area covered by the coil. In reality some fringing will be present in the walls of the pan which will additionally influence  $R_{wp}$ . However, the contribution of this flux is small and for simplicity sake it is neglected here. Further, according to (3.2)  $R_{wp}$  will decrease with smaller vessels which will lead to requirement of higher current. In the current design it is assumed that the cooktop will have several coils with different size which to meet the requirement of the small vessels. Here only one type of coil is designed in accordance to the dimensions described in §3.1.

From (3.2) and (1.1) the required current in the workpiece can be found from:

$$I_{wp} = \sqrt{\frac{P_{joule}}{R_{wp}}}, \text{ [A]} \quad (3.4)$$

The influence of the frequency on  $R_{wp}$  and  $I_{wp}$  in case of  $P_{joule} = 1.5\text{kW}$ ,  $d_1 = 220\text{mm}$ ,  $d_2 = 40\text{mm}$ ,  $t_{wp} = 20^\circ\text{C}$  and  $t_{wp} = 100^\circ\text{C}$  are tabulated in Table 3.1. For visualization

sake, the data for AL3004 and ASTM40 in case of  $t_{wp} = 20^\circ\text{C}$  is also plotted in Fig. 3.2. In Table 3.1 the temperature of  $100^\circ\text{C}$  is selected considering that at sea level the boiling temperature of the water is close to  $100^\circ\text{C}$  and this, to some extent, is the maximum temperature to which the cooking vessel will be heated. Further, the frequency is limited to 400kHz so that frequency control to be implemented. In the calculation of ASTM40 the reduction of  $\mu_r$  with increase of  $B$  is not taken into account.

From the table it can be seen that the highest  $R_{wp,AL}$  is achieved at 400kHz and  $100^\circ\text{C}$ , which might lead to conclusion that 400kHz is the most appropriate  $f_{sw}$ . However, closer look at Fig. 3.2 reveals that above 200kHz a saturation point is reached and the decrease of  $I_{wp}$  is not very well pronounced anymore. A better estimation of  $f_{sw}$  can be made after calculation of coil losses and efficiency of heating (§2.1).

In all further calculation involving  $R_{wp}$  the temperature is set to  $20^\circ\text{C}$ . This will allow the induction cooker to deliver power higher than 1.5kW to vessels covering the entire coil and close to 1.5kW to smaller vessels.

**Table 3.1.** Calculated workpiece resistances and currents for different frequencies and temperatures.

Parameter	Frequency							
	10kHz		100kHz		200kHz		400kHz	
$t$ [ $^\circ\text{C}$ ]	20	100	20	100	20	100	20	100
$R_{wp,AL}$ [ $\text{m}\Omega$ ]	0.19	0.23	0.6	0.71	0.84	1.01	1.19	1.42
$R_{wp,steel}$ [ $\text{m}\Omega$ ]	0.25	0.27	0.78	0.85	1.11	1.20	1.57	1.69
$R_{wp,iron}$ [ $\text{m}\Omega$ ]	3.69	3.83	11.7	12.1	16.5	17.1	23.4	24.2
$I_{wp,AL}$ [A]	2810	2554	1581	1453	1336	1218	1223	1027
$I_{wp,steel}$ [A]	2449	2357	1387	1328	1162	1118	977	942
$I_{wp,iron}$ [A]	638	626	358	352	301	269	253	250

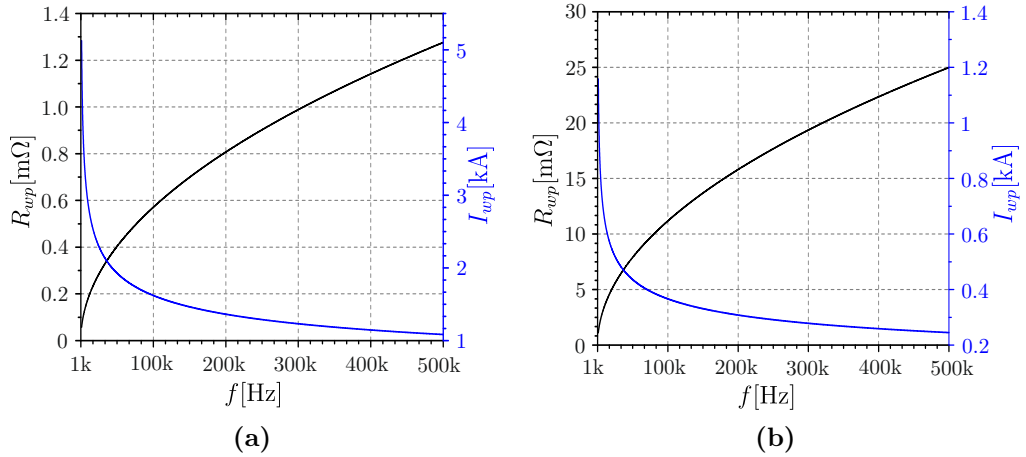


**Fig 3.2.** Workpiece resistance and current in function of frequency in case of  $P_{joule} = 1.5\text{kW}$  (a) AL3004 and (b) ASTM40. For both material  $\rho(T)$  @  $20^\circ\text{C}$ .

### 3.2.1.2 Coil Design and Estimation of Switching Frequency

As state above, the design of the coil is based on a simple planar coil (Fig. 3.1)<sup>1</sup>. Due to the high current levels, the high frequencies and the pronounced skin effect, a litz wire is selected for the design of the coil.

The required current in the coil can be approximated from  $R_{wp}$ , in the following way:

$$R_{ek} = n^2 k R_{wp}, [\Omega] \quad (3.5)$$

$$I_{coil} = \sqrt{\frac{P_{joule}}{R_{ek}}}, [A] \quad (3.6)$$

where:

- $R_{ek}$  – equivalent resistance of  $R_{wp}$  referred to the coil side of the circuit  $[\Omega]$  (§2.2);
- $n$  – number of turns of the coil;
- $k$  – coupling between the cooking vessel and the coil (§2.2);

The coupling can be calculated by (2.13). Because the equation is derived for coupling of linear transformers with interleaved windings, its validity for induction heating and planar coils was practically verified before its employment. For the purpose two planar coils were designed and mounted one above other on a distance of 3mm. The one coil imitated the work coil in the induction heating ( $L_1$  Fig. 2.1(a)) and the second one the workpiece inductance ( $L_2$  Fig. 2.1(a)). Initially the inductances ( $L$  and  $L_{sh}$  (2.13)) were measured by an LCR meter. After that a second measurement, aiming for accounting the influence, if any, of the current to the inductances, was made by forming a resonant network and tuning it to the resonant frequency. In that way the value of the inductance was calculated by [43]:

$$L = \frac{1}{4\pi^2 C_r f_r}, [H]$$

With the measured inductances the coupling was calculated with the help of (2.13) and the results are tabulated in Table 3.2.

In order calculated  $k$  to be verified another approximation of  $k$  was derived:

$$n = \sqrt{\frac{L_1}{L_2}} \quad (3.7)$$

$$I_{sec} = nkI_{prim} \Rightarrow k = \frac{I_{sec}}{nI_{prim}} \quad (3.8)$$

where:

- $L_1$  – inductance of the coil supplied by the inverter [H];
- $L_2$  – inductance of short circuited coil with short circuit removed [H].

In (3.7) it was used the fact, that both coils have the same shape and the only difference is the number of turns squared.

---

<sup>1</sup>Several papers have proposed different approaches for design of planar coils aiming to equalize the temperature distribution in iron cooking vessels [47], [48] and [49]. In this master thesis, due to good thermal conductivity of aluminum, sandwiching of aluminum between two layers of stainless steel and moderate thermal conductivity of cast iron's, the thermal distribution will be considered homogenous.

For calculating the coupling by (3.8) the currents in the  $L_1$  and  $L_2$  were measured by connecting the formed linear transformer ( $L_1$  and  $L_2$ ) to a resonant network, tuning it to  $f_r$  and short circuiting the terminals of  $L_2$ . The measured results are given in Table 3.2. From the table it can be seen that all three measurements give close result. The difference between different approaches can be contributed to inaccuracies in the measurement.

The accuracy of (3.8) was further verified by computer simulation using the measured values of  $L_1$ ,  $L_2$  and  $k$  and measuring the currents in the terminals of both inductances. It was observed that as  $k$  approaches 1 the accuracy increase and for  $k = 0.88$  the error was estimated to be approximately  $9.33 \times 10^{-4} \%$ .

**Table 3.2.** Comparison between theoretically calculated value of  $k$  and practically measured.

Type of Measurement	$L$ [ $\mu\text{H}$ ]	$L_2$ [ $\mu\text{H}$ ]	$L_{sh}$ [ $\mu\text{H}$ ]	$k$	Error [%]
LCR meter	56.5	50.7	16	0.85	0
Resonant	57.15	—	13.8	0.87	2.3
$f$ [kHz] <sup>(1)</sup>	67.4	—	137	—	—
Current primary [A]	—	—	7.65	0.88 <sup>(2)</sup>	5.7
Current secondary [A]	—	—	6.9		

<sup>(1)</sup>  $C_r = 97.66\text{nF}$

<sup>(2)</sup>  $k = \frac{I_{sec}}{\sqrt{n}I_{prim}}$

With the help of (2.13) for  $t_{gap} = 5\text{mm}$ , and with specified coil dimensions, the coupling was estimated to be  $k = 0.78$ . The selected  $t_{gap}$  is sufficient for accommodating a supporting material between the cooking vessel and the coil and some additional air gap for further thermal insulation and cooling.

For achieving the highest possible efficiency the optimum coil current must be estimated. From (3.5) and (3.6) it can be seen that  $I_{coil}$  depends on the number of turns in the coil ( $n$ ) and the frequency ( $f$ ). The most appropriate frequency can be estimated from the efficiency of heating. The number of turns, however, are limited by several factors:

(a) the allowed winding area ( $w$  in Fig. 3.1) and OD of the litz wire – that is if  $n \uparrow OD \downarrow$  which will lead to increase in the losses in the litz wire ( $A_{litz} = \frac{\pi \times OD^2}{4}$ ); the maximum value of OD is also limited by manufacturing capabilities of the litz wire manufacturers;

(b) the inductance of the coil ( $L_{coil}$ ), for planar type of coil, is related to  $n$  by [50]:

$$L_{coil} = 15.22 \frac{\mu_0}{8\pi} n^2 w, \text{ [H]} \quad (3.9)$$

hence  $n \uparrow L_{coil}^2 \uparrow$ ;

(c) the value of resonant capacitor is related to  $L_{coil}$  by:

$$f = \frac{1}{2\pi\sqrt{L_{coil}C_r}}, \text{ [Hz]} \quad (3.10)$$

so  $L_{coil} \uparrow C_r \downarrow$ ;

(d) and the voltage across  $C_r$  is related to  $I_{coil}$  by:

$$U_{C_r} = \frac{I_{coil}}{2\pi f_{sw} C_r}, \text{ [V]} \quad (3.11)$$

$C_r \downarrow U_{C_r} \uparrow$ .

**Table 3.3.** Recommended strand size for given frequency range [51].

Frequency	Recommended Wire Gauge	Nominal Diameter over Copper	D.C. Resistance Ohms/M' (Max)	Single Strand $R_{AC} / R_{DC}$ "S"
60 HZ - 1 KHZ	28 AWG	0.0126	66.37	1.0000
1 KHZ - 10 KHZ	30 AWG	0.0100	105.82	1.0000
10 KHZ - 20 KHZ	33 AWG	0.0071	211.70	1.0000
20 KHZ - 50 KHZ	36 AWG	0.0050	431.90	1.0000
50 KHZ - 100 KHZ	38 AWG	0.0040	681.90	1.0000
100 KHZ - 200 KHZ	40 AWG	0.0031	1152.3	1.0000
200 KHZ - 350 KHZ	42 AWG	0.0025	1801.0	1.0000
350 KHZ - 850 KHZ	44 AWG	0.0020	2873.0	1.0003
850 KHZ - 1.4 MHZ	46 AWG	0.0016	4544.0	1.0003
1.4 MHZ - 2.8 MHZ	48 AWG	0.0012	7285.0	1.0003

Obviously, the parameters:  $L_{coil}$ ,  $f_r$ ,  $C_r$  and  $U_{C_r}$  conflict with each others and an optimal decision, considering the manufacturing capabilities of litz wire, high frequency high power capacitors and the losses in the litz wire, must be made. For the purpose, the influence of the strand diameter, diameter of the litz wires, the number of turns in the coil and the frequency on the efficiency of heating have been investigated. During the investigation the available power capacitors and litz wires were considered and used as limiting factor. The steps taken during the investigation and the achieved results are outlined bellow.

On Table 3.3 is tabulated the recommended, by the manufacturers, strand types for given frequency range [51]. On Fig. 3.3 is shown the influence of the strand type on the efficiency of heating in case of  $n = 15$  (Fig. 3.3(a)) and  $n = 20$  (Fig. 3.3(b)), the current in the coil (Fig. 3.3(c)) and the losses in the coil (Fig. 3.3(d)). The number of turns are selected in accordance with the iron induction cookers [52].

For plotting the graphs the following equations and data were used (the used Matlab script is given in **Appendix A**):

- single layer coil with dimensions according to §3.1;
- the OD is calculated for every strand type by:

$$OD = FF \frac{w}{n}, \text{ [m]} \quad (3.12)$$

where:

$FF$  – filling factor  $FF = 0.95$  [53] [54];

- the number of strands bunched in the cable [55]:

$$n_s = \left( \frac{OD}{1.155 d_{s,overal}} \right)^2, \text{ [m]} \quad (3.13)$$

where:

$d_{s,overal}$  – maximum overall diameter of the strand [56];

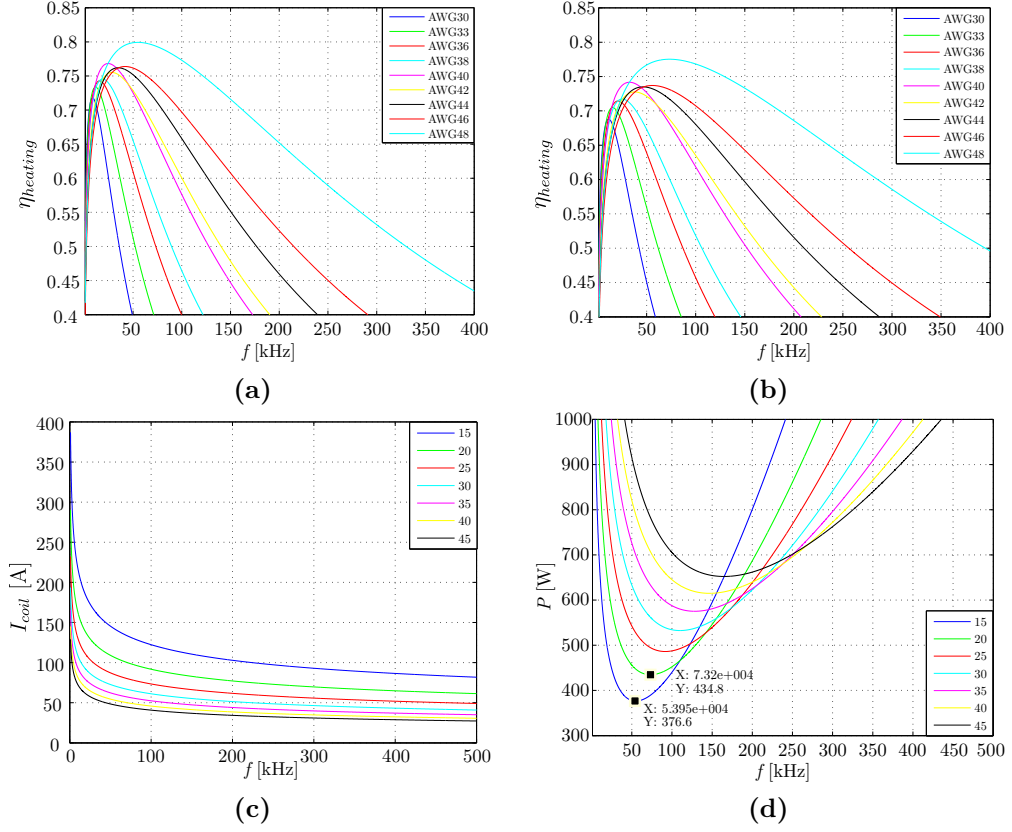


**Fig 3.3.** Efficiency of heating in function of frequency for coil with (a) 15 and (b) 20 turns for different strand types. (c)  $I_{\text{coil}}$  and (d) coil losses in function of frequency for different strand types.

- the coil's DC resistance of litz wire [57]:

$$MLT = \pi \frac{d_1 + d_2}{2}, \text{ [m]} \quad (3.14)$$

$$R_{dc,coil} = \frac{1.015^{n_b} 1.025^{n_c} R_{dc,s} n MLT}{n_s}, \text{ [\Omega]} \quad (3.15)$$

where:

- $MLT$  – Mean Length per Turn [m];
- $n_b$  – bunching operations  $n_b = 1$ ;
- $n_c$  – cabling operations  $n_c = 1$ ;

- the proximity effect contribution [58]:

$$R_{ac,coef} = 1 + \frac{\pi^2 \omega^2 \mu_0^2 n^2 n_s^2 d_s^2 k}{768 \rho_c^2 w^2} \quad (3.16)$$

where:

$$\omega = 2\pi f \text{ [rad/s];}$$

$d_s$  – single strand bare diameter [m];

$k$  – factor accounting for field distribution ( $k = 1$ );

$\rho_c$  – the specific resistance of the copper  $\rho_c = 1.72 \times 10^{-8} [\Omega \cdot \text{m}]$ ;

- the total resistance is  $R_{ac,coil} = R_{dc,coil} R_{ac,coef}$ , [ $\Omega$ ];
- the efficiency of heating is calculated by (2.1) with  $R_{ek}$  given by (3.5) and  $I_{coil}$  by (3.6).

The used equations approximates the real number of  $n_s$  and  $R_{dc}$  and the achieved results are approximate. because of this, they are used only as guidelines for selecting the strand type and  $n$ .

From Fig. 3.3(a) and Fig. 3.3(b) it can be seen that the highest  $\eta_{heating}$  is achieved when strand type of AWG48 and small number of turns are used ( $n = 15$ ). From Fig. 3.3(c) it can be seen that in case of  $n = 15$  and  $f = 50\text{kHz}$   $I_{coil} \approx 150\text{A}$ . The current is suitable for parallel resonant network where  $I_{coil}$  flows only in the coil and resonant capacitor (Fig. 1.4(b)). In the case of series resonant network  $I_{coil}$  flows also in the windings of the matching transformer which will lead to increase of the copper losses in the transformer. From Fig. 3.3(d) it can be seen that the difference between losses in case of  $n = 15$  and  $n = 20$  is approximately 60W. Considering that the current reduction between coil with  $n = 15$  and  $n = 20$  is approximately 50% (Fig. 3.3(c)) the difference in the coil losses could be compensated by the copper losses in the transformer and the losses in  $C_r$ . Because of this in the further investigation  $n = 20$  and litz types AWG40, AWG42, AWG44 and AWG46 will be used. AWG48 is not included in the investigation due to limited OD (OD = 4.03mm) currently produced. The OD is below the maximum achievable OD with the selected  $w$  and  $n$  which is:

$$\text{OD} = FF \frac{w}{n} = 0.95 \frac{0.09}{20} = 4.27\text{mm} \quad (3.17)$$

In Table 3.4 are tabulated the parameters of litz cables produced by New England with suitable OD for achieving  $n \approx 20$  [59].

Because the produced cables differ in OD, which will influence the comparison, the parameters for strand types AWG42 and AWG44 are calculated by averaging the parameters of cables with the next lower and higher OD.

**Table 3.4.** Maximum OD of litz cable produced by New England Wire Technologies [59].

Strand type	OD [mm]	$n_s$	$R_{dc}$ [m $\Omega$ /m]	$n$	Construction
AWG40	4	1100	3.7	22	5x5x44/40 <sup>(2)</sup>
AWG42	4 <sup>(1)</sup>	1380 <sup>(1)</sup>	4.9 <sup>(1)</sup>	22	–
AWG44	3.78	2625	3.97	23	5x5x3/35/44)
AWG46	3.9 <sup>(1)</sup>	3525 <sup>(1)</sup>	4.9 <sup>(1)</sup>	22	–

<sup>(1)</sup> averaged value

<sup>(2)</sup> x indicates cabling operations ( $n_c$ ) and / bunching operations ( $n_b$ )

Based on the data from Table 3.4 new calculations have been made and the results are presented in Fig. 3.4. From the figure it can be seen that the highest efficiency is achieved with strand types AWG44 and AWG46.

AWG44 is selected for the coil design, due to limited maximum OD of cables produced with AWG46 (OD = 4.85mm [59]). Further, AWG44 achieves its maximum  $\eta_{heating}$  at lower frequencies than AWG46, which will lead to lower switching losses in the inverter and lower core losses in the transformer.

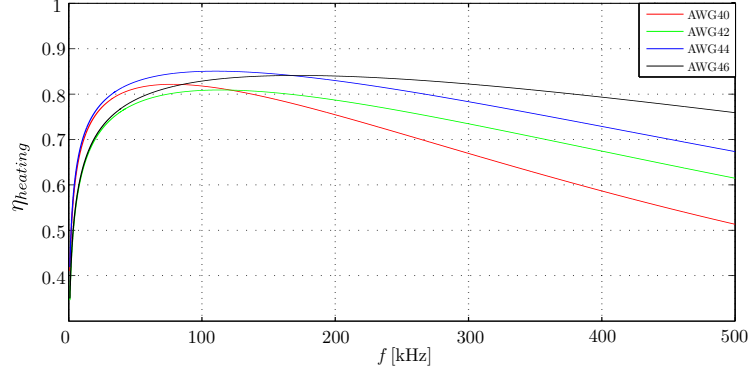


**Fig 3.4.** Efficiency of heating for strand types AWG40, AWG42, AWG44, AWG46 and AWG48.

The calculated OD by (3.17) leads to high current density and high losses in the coil (Fig. 3.3(d)):

$$J_{litz} = \frac{4I_{coil}}{\pi OD^2} = \frac{4 \times 90}{3.14 \times (3.78\text{mm})^2} = 8.02\text{A/mm} \quad (3.18)$$

where:

OD is given by (3.17);

$I_{coil}$  is taken from Fig. 3.3(c) in case  $f = 100\text{kHz}$  and  $n = 20$ ;

Increase of OD can be achieved either by connecting two coils with OD calculated by (3.17) in parallel (Fig. 3.5(a)) or by connecting two coils with bigger OD in series as shown on Fig. 3.5(b). In the former case the current density is reduced by factor of two (losses by 4). It also reduces the coupling between the coil and the cooking vessel, as it influences the flux linking with the pan, and increases  $R_{ac}$  due to increase of the proximity effect. In the case of Fig. 3.5(b), due to partial coverage of the second layer, the coupling and  $R_{ac,coil}$  are less effected, while  $R_{wp}$  is slightly increased due to higher current circulating in the periphery of the coking vessel Fig. 3.5(b). Because of its benefits the latter approach is adopted here.

**Table 3.5.** Parameters of litz cable based on AWG44.

Strand type	OD [mm]	$n_s$	$R_{dc}$ [mΩ/m]	Construction
AWG44	5.74	4200	2.45	6(5x5/28/44)

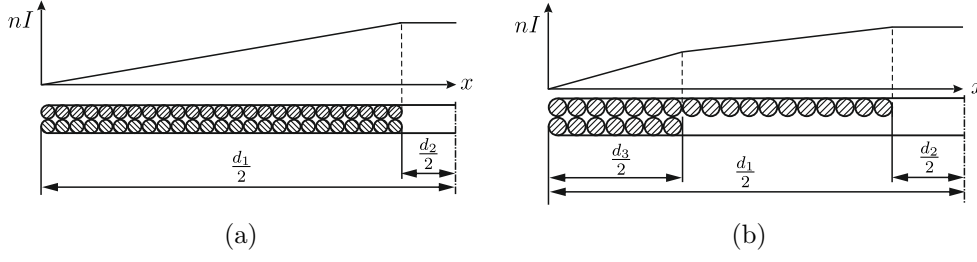


**Fig 3.5.** Possible coil designs.

The selected standard litz cable bunched with AWG44 is shown on Table 3.5 [59]. The number of turns which can be accommodated in the first layer in this case are:

$$n_{first} = FF \frac{w}{OD} = 0.95 \frac{0.09}{5.74\text{mm}} \approx 15\text{turn} \quad (3.19)$$

On Fig. 3.6 are shown the achieved result with selected litz cable,  $n = 20$ , data from Table 3.5 and designed in accordance to Fig. 3.5(b). In plotting of the graphs, the reduction of the coupling, the increase of coil's  $R_{ac}$  and increase of  $R_{wp}$  are not taken into account. From the figure it can be seen that the increase of  $n_s$  led to reduction of the frequency to  $f \approx 110\text{kHz}$ .

For calculation of  $C_r$  the inductance of the coil can be calculated analytically by [50]:

$$L = \sum_{k=1}^n L_k + \sum_{k=1}^n \sum_{i=1}^n M_{ki} \quad k \neq i \quad (3.20)$$

where:

- $k$  – the number of layers;
- $L_k$  – the self inductance of each layer;
- $M_{ki}$  – the mutual inductance between each layers.

However, (3.20) requires a knowledge of the coupling between the two coils which is difficult for analytical derivation. Because of this, a real coil was designed and its inductance was measured. The coil was based on a litz wire with  $OD \approx 5.5\text{mm}$ , 16 turn in the first layer and 7 turns in the second layer. The measured no load inductance was  $L_{noload} = 66\mu\text{H}$  and inductance with load  $L_{load} = 22\mu\text{H}$ . The number of turns were made 23 instead of 20 which leads to increase of  $L_{noload}$ . However,  $L_{load}$  is slightly affected because in the physical design was based on  $t_{gap} = 3\text{mm}$  instead of 5mm, which increased the coupling and reduced  $L_{load}$ .

For the measured  $L_{load}$  and desired  $f = 110\text{kHz}$  the value of  $C_r$  is:

$$C_r = \frac{1}{4\pi^2 f^2 L_{load}} = \frac{1}{4 \times 3.14^2 \times (110\text{kHz})^2 \times 22\mu\text{H}} = 95\text{nF} \quad (3.21)$$

with  $U_{C_r}$ :

$$U_{C_r} = \frac{I_{coil}}{2\pi f C_r} = \frac{80}{2 \times 3.14 \times 110\text{kHz} \times 95\text{nF}} = 1.22\text{kV} \quad (3.22)$$

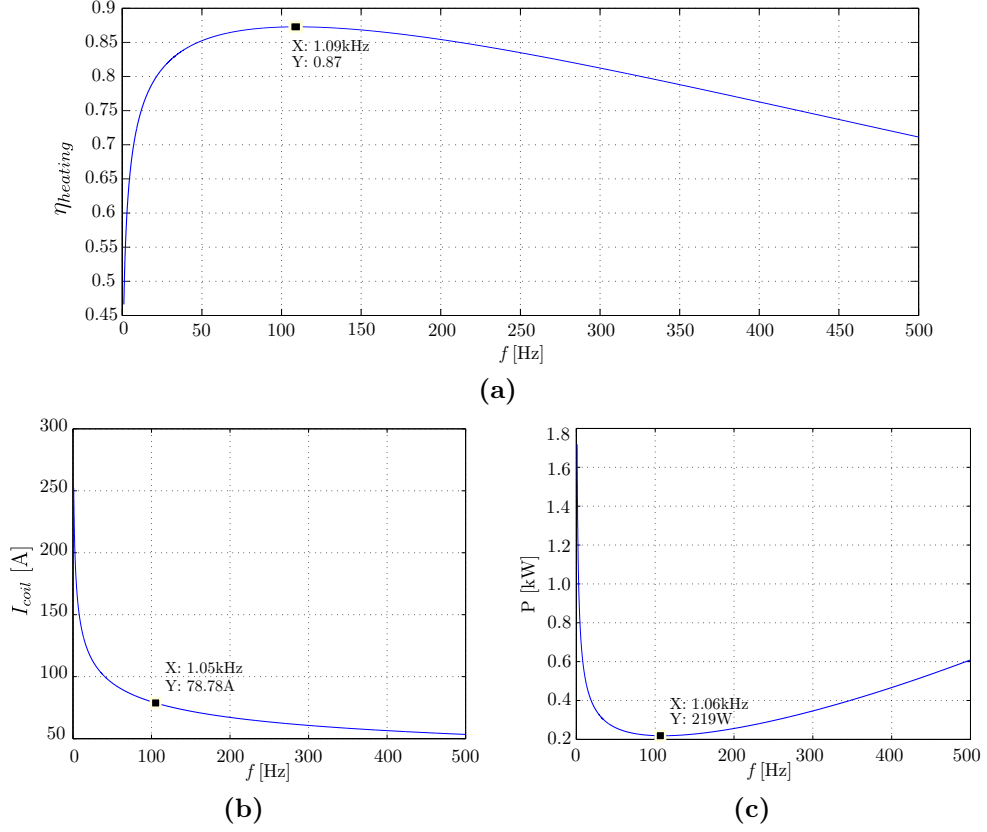


**Fig 3.6.** Achieved results for litz cable with OD = 5.74mm, bunched with AWG44. (a)  $\eta_{heating}$ , (b)  $I_{coil}$  and (c) losses coil.

where:

$I_{coil}$  is selected from Fig. 3.6(b) and rounded to 80A.

On Table 3.6 and Fig. 3.7 are shown the parameters and dimensions of CSP 120/200 type power capacitors produced by Celest Power Capacitors Ltd. [60]. From the table it can be seen that the closest capacitor to calculated one is 2x170nF connected in series. The capacitance in that way is 85nF,  $f_r = 116$ kHz, voltage across per capacitor is  $U_{C_r} = 646$ V and

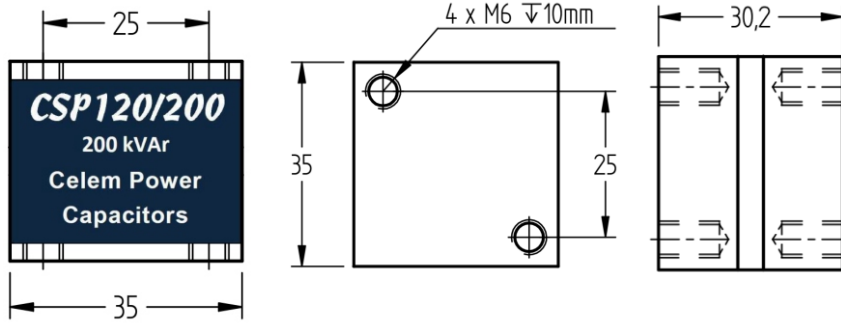
$$Q_{C_r} = I \times U_{C_r} = 80 \times 646 = 51.67\text{kVAR} \quad (3.23)$$

The three parameters,  $I_{C_r} = I_{coil}$ ,  $U_{C_r}$  and  $Q_{C_r}$  are met by the capacitor with proper derating (Fig. 3.8) [60].

From Fig. 3.6(c) it can be seen that the losses in the coil are approximately  $P_{losses,coil} = 219$ W. The value is high for natural convection and a forced air cooling might be required. A better estimation of the required cooling can be achieved either by FEM simulation or practical design. In the thesis, as main aim of the coil design being the electrical parameters and not the thermal, the thermal design is not carried out. It will be assumed that the cooling system is capable of maintaining the litz strands the temperature in the specified limits.

**Table 3.6.** Parameters of CSP120/200 series capacitors produced by Celem Power Capacitors [60].

TYPE	CSP 120 / 200									
Dimensions (L x W x H)	mm	35 x 35 x 30.2								
Weight	kg	0.15								
Capacitance ( $\pm 10\%$ )	$\mu F$	0.025	0.05	0.085	0.17	0.25	0.33	0.66	1.2	
Sinusoidal Voltage	$V_{rms}$	1100	1000	900	800	700	600	500		
Peak Voltage	$\hat{V}$	1560	1410	1270	1130	990	850	710		
Max. Current	$A_{rms}$	200			250	270	300	350	400	
Max. Power	$kVA_r$	180			200					
Freq Range @ Full Power	kHz	947-1415	573-707	374-374	231-293	199-232	197-217	134-148	106-106	
Stray Inductance	nH	<3								

**Fig 3.7.** CSP120/200 series capacitors dimensions [60].

With calculated values the quality factors of an iron and aluminum cooking vessels can be calculated:

$$Q_{AL} = \frac{2\pi f_{sw} L_{load}}{R_{ek}} = \frac{2 \times 3.14 \times 116\text{kHz} \times 22\mu\text{H}}{0.197} \approx 82.6 \quad (3.24)$$

for aluminum cooking vessel, and:

$$Q_{iron} = \frac{2\pi f_{sw} L_{load}}{R_{ek}} = \frac{2 \times 3.14 \times 116\text{kHz} \times 22\mu\text{H}}{3.77} \approx 4.2 \quad (3.25)$$

for iron vessel.

For sake of visualization the steepness of the quality factor and appreciation the challenges involved in control of such load, on Fig. 3.9 the normalized currents for aluminum and iron cooking vessels in function of frequency are plotted.

### 3.2.2 Output of the Coil Design

The output of coil design is:

- coil dimensions –  $d_1 = 200\text{mm}$ ,  $d_2 = 40\text{mm}$  and  $t_{gap} = 5\text{mm}$ ;

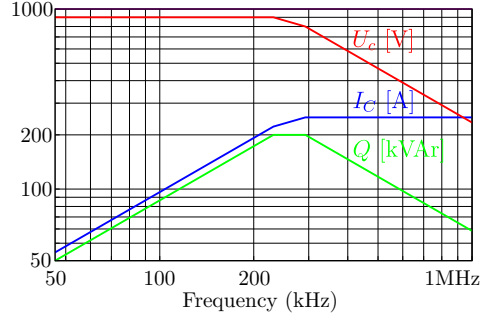


**Fig 3.8.** Parameters of CSP120/200 0.17 $\mu$ F capacitor [60].

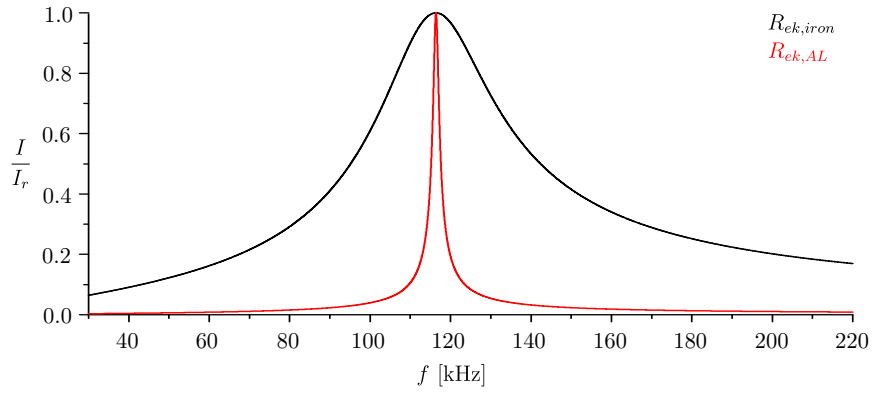


**Fig 3.9.** Quality factor for aluminum and iron cooking vessels.

- coil design according to Fig. 3.5(b) with  $n_{first} = 15$  and  $n_{second} = 5$ ;
- $L_{noload} = 66\mu\text{H}$ ,  $L_{load} = 22\mu\text{H}$  and  $R_{ac,coil} = 30\text{m}\Omega @ 116\text{kHz}$ ;
- $I_{coil,AL} = 78.78\text{A} \approx 79\text{A}$ ,  $I_{coil,iron} = 19.95\text{A} \approx 20\text{A}$ ,  $J_{coil,AL} = 3\text{A}/\text{mm}^2$ ,  $P_{losses,coil} = 219\text{W}$  and  $k = 0.78$ ;
- litz wire according to Table 3.5;
- $f_{r,noload} \approx 67.2\text{kHz}$  and  $f_{r,load} \approx 116\text{kHz}$ ;
- $C_r = 2 \times 170\text{nF}$  and  $U_{C_r} = 2 \times 646\text{V}$ ;
- $R_{ek,AL} = 0.194\Omega @ 120\text{kHz}$  and  $R_{ek,iron} = 3.77\Omega @ 116\text{kHz}$ <sup>2</sup>.

### 3.3 Dimensioning of the Inverter

In general, the IC is designed to control a Half Bridge inverter (Fig. 3.10). However, before dimensioning of the inverter, an investigation of the suitability of the topology as a solution

<sup>2</sup>Due to frequency control and low turn ration the controller will increase  $f_{sw}$  for aluminum so that the power can be 1.5kW. In case of iron the controller will keep  $f_{sw}$  close to the resonant frequency.

for the problem is made. The investigation is based on estimation the losses in the inverter and the possibility of dissipating the generated power in the switches used for decision making.

For proper functioning, the IC's requires a constant input voltage ( $U_{dc}$ ) which is selected to be  $U_{dc} = 390V$ . In that way typical  $470\mu F/400V$  capacitors can be used ( $C_1$  Fig. 3.10) while the DC current is kept as low as possible. The constant voltage is achieved by the rectifier ( $D_1, D_2, D_3$  and  $D_4$ ) and PFC ( $L_1, Q_1, D_5$  and  $C_1$ ) in the input stage of the inverter. Dimensioning of both stages is not part of the master thesis.

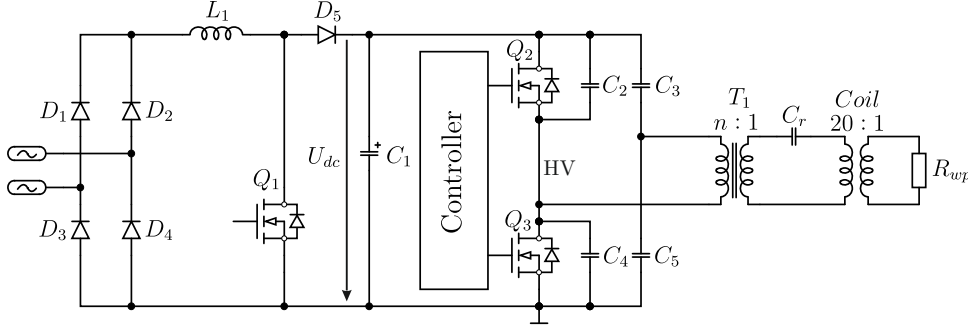


Fig 3.10. Half Bridge inverter schematic.

### 3.3.1 Calculation of Losses in Half Bridge Topology

For determination of the losses in the switches, the primary current of the transformer  $T_1$  is required. The current is related to the transformation ration ( $n$ ) of the transformer which is set by  $R_{ek,iron}$  as the resistance having the highest value and requiring the highest voltage:

$$U_{iron} = \sqrt{P_{out} R_{ek,iron}} = \sqrt{1500 \times 3.77} = 75.2V \quad (3.26)$$

$$U_{sec} = \frac{\pi}{4} \sqrt{2} U_{iron} = \frac{3.14}{4} \sqrt{2} \times 75.2 = 83.48V \quad (3.27)$$

$$U_{pr,HB} = \frac{U_{dc}}{2} = \frac{390}{2} = 195V \quad (3.28)$$

$$n = \frac{U_{pr,HB}}{U_{sec}} = \frac{195}{83.48} = 2.3 \quad (3.29)$$

where:

$U_{iron}$  – voltage across  $R_{ek,iron}$  [V];

$U_{sec}$  – square wave voltage at the secondary side of  $T_1$  [V];

$U_{pr}$  – voltage at primary terminals of  $T_1$  [V].

In (3.26)  $R_{ac,coil}$  is ignored due to its small contribution.

From (3.29) the currents in the primary winding of  $T_1$  in case of aluminum and iron vessels are:

$$I_{pr,AL} = \frac{I_{coil,AL}}{n} = \frac{79}{2.3} = 34.34A \quad (3.30)$$

$$I_{pr,iron} = \frac{I_{coil,iron}}{n} = \frac{20}{2.3} = 8.7A \quad (3.31)$$

With the help of (3.30) the conduction and the switching losses can be calculated which are higher in case of aluminum cooking vessel due to the higher current.

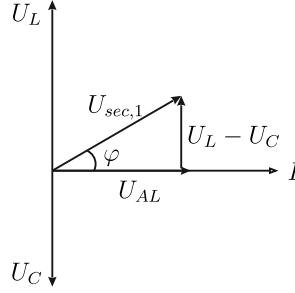


**Fig 3.11.** Vector diagram of series resonant network in case  $\omega_s > \omega_r$ .

For calculation of switching losses the turn-off current ( $I_{C,pk2}$  Fig. 1.13) and  $f_{sw}$  must be known.

The turn-off current can be calculated in the following way:

$$U_{sec,1} = \frac{4}{\pi} \frac{U_{sec}}{\sqrt{2}} = U_{iron} = 75.2V \quad (3.32)$$

$$\alpha_{AL} = \arccos \frac{P_{out}}{U_{sec,1} I_{coil,AL}} = \arccos \frac{1500}{75.2 \times 79} = 75.37^\circ \quad (3.33)$$

$$I_{pk,turn-off,AL} = \sqrt{2} I_{pr,AL} \sin \alpha_{AL} = \sqrt{2} \times 34.34 \times \sin 75.37 = 46.99A \quad (3.34)$$

where:

$U_{sec,1}$  – fundamental voltage at the secondary side of the transformer;

$\alpha_{AL}$  – angle between voltage and current (Fig. 1.13) in case of aluminum vessel [deg].

The  $f_{sw}$  in case of aluminum cooking vessel can be found from Fig. 3.11 in the following way:

$$U_{AL} = \sqrt{P_{out} R_{ek,AL}} = \sqrt{1500 \times 0.194} = 17.06V \quad (3.35)$$

$$U_L - U_{C_r} = U_{AL} \tan \alpha_{AL} = 17.06 \times \tan 75.37 = 65.35V \quad (3.36)$$

where:

**Table 3.7.** Parameters of low  $R_{DS,on}$  MOSFET and fast IGBT [61][62].

Parameters								
Mosfet	$U_{DS}$ [V]	$I_D^{(1)}$ [A]	$R_{DS,on}$ [m $\Omega$ ]	–	$t_f$ [ns]	$P^{(2)}$ [W]	$R_{jc}$ [ $^{\circ}$ C/W]	Package
IPW65R037C6	650	52.6	70 <sup>(1)</sup>	–	7	500	0.25	TO247
FGH60N60SMD	600	60	24.2 <sup>(3)</sup>	1.1V <sup>(3)</sup>	1.1mJ <sup>(4)</sup>	600	0.25	TO247
IGBT	$U_{CE}$	$I_C$	$R_{CE,on}$	$U_{CE,on}$	$E_{off}$	$P^{(2)}$	$R_{jc}$	Package

<sup>(1)</sup> @120 $^{\circ}$ C

<sup>(2)</sup> @25 $^{\circ}$ C

<sup>(3)</sup> @175 $^{\circ}$ C

<sup>(4)</sup> @175 $^{\circ}$ C,  $I_{C,test} = 60$ A,  $U_{CE,test} = 400$ V,  $R_G = 10\Omega$

$$U_L = X_L I_{coil,AL} = \omega L_{coil} I_{coil,AL} \quad (3.37)$$

$$U_{C_r} = X_C I_{coil,AL} = \frac{I_{coil,AL}}{\omega C_r} \quad (3.38)$$

from here:

$$I_{coil,AL} \omega L_{coil} - \frac{I_{coil,AL}}{\omega C} = U_{AL} \tan \alpha_{AL} \Rightarrow I_{coil} \omega^2 - \frac{U_{AL}}{I_{coil,AL}} \tan \alpha_{AL} \omega - \frac{1}{C_r} = 0 \quad (3.39)$$

with:

$$\omega = 2\pi f_{sw} \quad (3.40)$$

The solution of (3.39) is:

$$\omega_{1,2} = \frac{\frac{U_{AL}}{I_{coil,AL}} \tan \alpha_{AL} \pm \sqrt{D}}{2L_{coil}} \quad (3.41)$$

with

$$D = \left( \frac{U_{AL}}{I_{coil,AL}} \tan \alpha_{AL} \right)^2 + 4 \frac{L_{coil,AL}}{C_r} \quad (3.42)$$

The positive root of (3.41) gives  $\omega_{AL} = 750.33 \times 10^3$ rad/s  $\Rightarrow f_{sw,AL} = 119.48$ kHz.

In Table 3.7 are tabulated the parameters of the lowest  $R_{DS,on}$  MOSFET<sup>3</sup> produced by Infineon Technologies<sup>4</sup> and the fastest (for the given  $I_C$  and  $U_{CE}$ ) IGBT<sup>5</sup> produced by Fairchild Semiconductor [63], [61], [64] and [62].

<sup>3</sup>Metal-Oxide-Semiconductor Field Effect Transistor.

<sup>4</sup>The company announced recently a new MOSFETs with  $R_{DS,on} = 19$ m $\Omega$  @25 $^{\circ}$ C which were not present during the development stage of the master thesis.

<sup>5</sup>Isolated Gate Bipolar Transistor.

With the data from the table the losses in the switches and the required heatsink are calculated. The results are tabulated in Table 3.8.

For calculations the following equations were used:

$$I_{rms,AL} = \sqrt{\frac{1}{2\pi} 2I_{pr,AL}^2 \int_0^\pi \sin^2 \omega t d\omega t} = \frac{\sqrt{2}}{2} I_{pr,AL} \quad (3.43)$$

$$I_{avg,AL} = \frac{\sqrt{2}}{2\pi} I_{pr,AL} \int_0^\pi \sin \omega t d\omega t = \frac{\sqrt{2}}{\pi} I_{pr,AL} = 15.47A$$

$$P_{cond,mosfet,AL} = I_{rms,AL}^2 R_{DS,on} \quad (3.44)$$

$$P_{cond,IGBT,AL} = I_{rms,AL}^2 R_{CE,on} + I_{avg,AL} U_{CE,on} \quad (3.45)$$

$$P_{sw,mosfet,AL} = \frac{U_{dc} I_{pk,turn-off,AL}}{2} 2t_f f_{sw,AL} \quad (3.46)$$

$$P_{sw,IGBT,AL} = \frac{I_{pk,turn-off,AL}}{I_{C,test}} \frac{U_{dc}}{U_{CE,test}} E_{off} f_{sw,AL} \quad (3.47)$$

$$P_{tot} = P_{cond} + P_{sw} \quad (3.48)$$

$$T_c = T_j - P_{tot} R_{jc} \quad (3.49)$$

$$R_{hs} = \frac{T_c - T_a}{P_{tot}} \quad (3.50)$$

where:

$I_{rms,AL}$  – rms currents contributing to conduction losses in case of AL3004 ( $I_{losses} \neq I_{pr}$  because every of the switches conducts only for half period) [A];

$I_{avg,AL}$  – average current in the primary in case of AL3004 [A] ;

$P_{cond,AL}$  – conduction losses in case of AL3004 [W];

$P_{sw,AL}$  – switching losses in case of AL3004 [W];

$t_f$  – fall time of  $I_D$  [s];

$I_{C,test}$  – magnitude of the current during the test in the datasheet [A];

$U_{CE,test}$  – magnitude of the voltage during the test in the datasheet [V];

$T_c$  – case temperature of the switch [°C];

$R_{hs}$  – thermal resistance of the heatsink for single switch [°C/W].

In calculation of  $P_{cond,mosfet}$ , it is considered that at the instance  $U_{DS}$  becomes zero, the controller will turn on the MOSFET connecting it in parallel to the freewheeling diode and in, that way, carrying the whole current<sup>6</sup>. Because of this losses are represented as losses in the MOSFETs only.

<sup>6</sup>In reality the whole current will flow through the MOSFET when  $U_{DS}$  is below the forward voltage of the diode ( $U_F$ ); otherwise the current will be shared between the diode and MOSFET.

**Table 3.8.** Calculated losses and cooling requirements per switch with the data from Table 3.7.

Parameters								
Mosfet	$I_{rms}$ [A]	$P_{cond}$ [W]	$P_{sw}$ [W]	$P_{tot}$ [W]	$T_j$ [°C]	$T_a$ [°C]	$T_c$ [°C]	$R_{hs}$ [°C/W]
IPW65R037C6	24.68	41.27	15.39	56.66	120 <sup>(1)</sup>	50	105.83	0.98
FGH60N60SMD		40.97	100.79	141.76	140 <sup>(1)</sup>		104.56	0.38

<sup>(1)</sup>  $0.8T_{j,max}$

In calculation of  $P_{cond,IGBT}$ , it is assumed that the parameters ( $U_F$ ,  $R_F$  and  $R_{j,c,D}$ ) of the freewheeling diode are identical to the one of the IGBT (in reality this is not the case, but for simplicity sake, they are ignored here).

In (3.46) it is assumed that the rise time of  $U_{DS}$  is equal to fall time of  $I_D$  during turn-off. In (3.50) the thermal resistance of the thermal pad (the electrical insulation pad) is ignored due to insufficient data in the manufacturer's datasheet. The thermal conductivity of the selected pad, EYGA091203RV, is specified as  $k = 1600\text{W}/(\text{m} \cdot \text{K})$  which for TO247 package gives  $R_{thpad} = 0.173 \times 10^{-3}\text{°C}/\text{W}$  [65]. However, the value does not include the electrical isolating material in the thermal pad which will further increase the thermal resistance of the pad.

In calculation of switching losses it is not taken into account the reduction of losses which the lossless snubbers ( $C_2$  and  $C_4$  on Fig. 3.10) will lead. However, the influence of the snubbers will be limited due to small value of the capacitors which can be used. The value of the snubber is related to the magnitude of the current at turn-off – hence angle  $\alpha$  (Fig. 1.13). In order the values of the snubbers to be large,  $\alpha$  must be increased and, in order the output power to be kept unchanged,  $n$  must be decreased (increasing  $\alpha$  will move the switching frequency away from  $f_r$  hence reducing the current; decreasing  $n$  will compensate this). This, however, will lead to increase of  $P_{cond}$  and  $P_{sw}$  in the switches. The selection of appropriate snubber capacitors will be carried out further in the master thesis. In this part of the master thesis the contribution of the snubber capacitors in case of MOSFETs will be ignored. Further, in case of IGBTs, snubbers will not be used as the small value of snubber will lead to increase in the losses rather than reducing them [66].

From Table 3.8, where the calculations are per switch, it can be seen that both type of switches have almost identical  $P_{cond}$ . However, the employment of IGBT is limited due to high switching losses and its employment in the design will not be considered. The MOSFETs performs better and the cooling demands can be met by forced air cooled heatsink. However, concentration of the heat in only two spots will lead to formation of hot spots in the heatsink and, in that way, lowering reliability of the unit. Further, because in the calculations the case-to-heatsink thermal resistance was not included, the practical thermal resistance of the heatsink must be lower than the calculated one. This demands for either a large heatsink with low air flow fan or small heatsink with large air flow fan. Both options will lead to higher price with either noisy fan or large heatsink.

Unquestionably, for reducing the losses in the switches, several devices can be connected in parallel. In that way the power dissipation area will increase alleviating the heatsink's thermal requirement. However, addition of two extra MOSFETs will make the circuit comparable with Full Bridge topology. Further, because the losses are related to  $P = RI^2$ , the

losses in Full Bridge will be lower than the Half Bridge (paralleling the devices will reduce  $R_{DS,on}$  two times while using Full Bridge topology will reduce the current two times). Additionally, the capacitors forming the middle point ( $C_3$  and  $C_5$  on Fig. 3.10) must carry high frequency current with magnitude of  $I_{pr,AL}/2 = 17.17A$  per capacitor with capacitance of:

$$i = \frac{dq}{dt} = \frac{C\Delta U_{cap}}{dt} \Rightarrow I_{avg} = CU_{cap,pk-pk}f_{sw} \quad (3.51)$$

$$C = \frac{I_{avg,AL}}{2U_{cap,pk-pk}f_{sw}} = \frac{15.47}{2 \times 10 \times 120kHz} = 6.44\mu F \quad (3.52)$$

where:

$U_{cap,pk}$  – desired peak to peak voltage drop across single capacitor  $U_{cap,pk} = 10V$  [V];  
the coefficient of 2 accounts for parallel connection of the capacitors for AC current.

This will require several FKP<sup>7</sup> or MKP<sup>8</sup> capacitors connected in parallel increasing further the cost and dimensions of the system.

Due to these reasons, the Half Bridge is considered impractical for the design and the Full Bridge topology is selected as suitable topology (Fig. 3.12).

### 3.3.2 Full Bridge Topology

The schematic of the Full Bridge is shown on Fig. 3.12. From the schematic it can be seen that:

$$U_{pr,FB} = 2U_{pr,HB} = 390V \quad (3.53)$$

$$n_{FB} = 2n_{HB} = 4.6turns \quad (3.54)$$

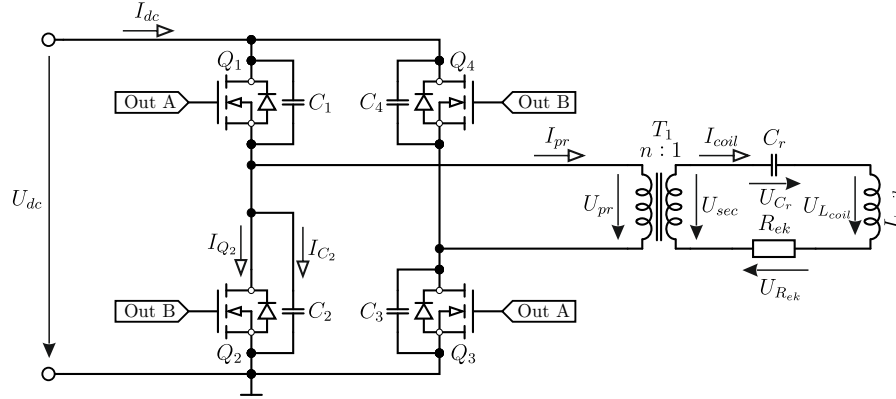


**Fig 3.12.** Full Bridge.

In the calculation of losses in Half Bridge topology it was assumed that, in case of iron cooking vessel, the IC works exactly on the resonant frequency. In reality this is

<sup>7</sup>Film polypropylene.

<sup>8</sup>Metalized polypropylene.

impossible due to propagation delays in the control signals and switching characteristics of the MOSFETs. That is why  $f_{sw} > f_r$  which will decrease the turn ratio and increase in the losses in the switches.

The minimum turn-off angle can be estimated in the following way. In Fig. 3.13 is shown an exemplary turn-off of a MOSFET part of a resonant inverter with lossless snubbers. From Fig. 3.13 it can be seen that for avoiding none ZV turn-on, in case of iron vessel as then the angle is the smallest, the switch must be turned-off at some angle ( $\varphi = 180^\circ - \alpha$  Fig. 1.13) bigger than zero. The minimal angle can be calculated from the figure in the following way:

$$\varphi_{iron} = 360^\circ \frac{t_1 + t_2 + t_3 + t_4 + t_5}{T} \quad (3.55)$$

where:

- $t_0 - t_1$  – propagation delay of output of the IC, gate drivers and turn-off delay of switch ( $t_{pd,off} = 83\text{ns}$  [67]) [s];
- $t_1 - t_2$  – fall time of  $I_D$  or  $I_C$  ( $t_f = 5\text{ns}$  [67]) [s];
- $t_1 - t_3$  – rise time of voltage across the switch [s];
- $t_3 - t_4$  – delay time for sensing and asserting the output Flip-Flop by the IC, after zero voltage across the switch [s];
- $t_4 - t_5$  – propagation delay of gate drivers and turn-on delay of switch ( $t_{pd,on} = 16\text{ns}$  [67]) [s].

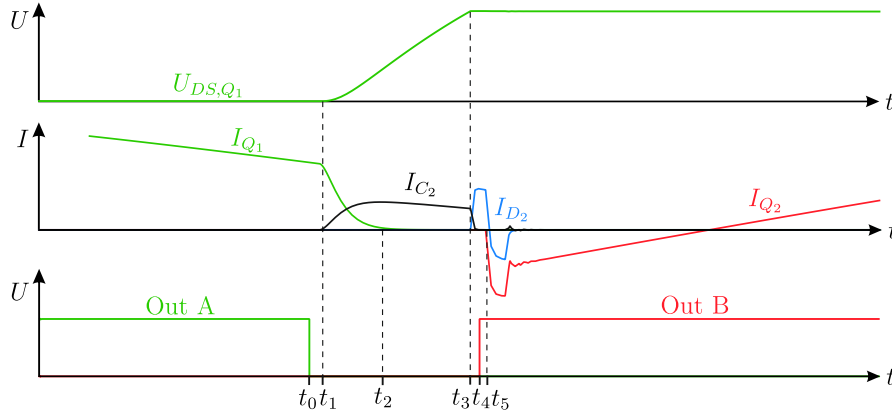


**Fig 3.13.** Typical turn-off and turn-on waveforms of a SRL resonant inverter (Fig. 3.12) (times not scaled).

Because the IC is still a prototype, its propagation delays are not measured yet. The times are included in the design as set value of  $2 \times 50\text{ns}$ .

The turn-on and turn-off propagation delay of the gate drivers depends on the type of the gate driver (optical or electromagnetic isolation), with electromagnetically isolated gate drivers exhibit the lowest propagation time. An example for fast electromagnetically isolated gate driver is ADuM3223 [68]. The gate driver has propagation  $t_{DLH} = 50\text{ns}$  and  $t_{DHL} = 50\text{ns}$  which will be used in the calculations.

The times  $t_{pd,off}$ ,  $t_{pd,on}$  and  $t_f$  are given for IPW60R070C6 MOSFET which has the parameters shown Table 3.9 [67]. The times are for the case of  $R_g = 1.7\Omega$ . Due to absence

of data in the datasheet accounting for influence of  $R_g$  on the switching times, the given values are used in the design.

**Table 3.9.** IPW60R070C6 MOSFET parameters [67].

Parameters							
Mosfet	$U_{DS}$ [V]	$I_D^{(1)}$ [A]	$R_{DS,on}$ [m $\Omega$ ]	$t_f^{(2)}$ [ns]	$P^{(3)}$ [W]	$R_{jc}$ [ $^{\circ}\text{C}/\text{W}$ ]	Package
IPW60R070C6	600	34	130 <sup>(1)</sup>	5	391	0.32	TO247

<sup>(1)</sup> @ 120 $^{\circ}\text{C}$

<sup>(2)</sup> @  $I_{D,test} = 25.8\text{A}$ ,  $U_{CE,test} = 400\text{V}$ ,  $R_G = 1.7\Omega$ ,  $V_{GS} = 13\text{V}$

<sup>(3)</sup> @ 25 $^{\circ}\text{C}$ ,

In that way  $\varphi$  can be calculated as:

$$\varphi_{iron} = 360^{\circ} \frac{t_1 + t_2 + t_3 + t_4 + t_5}{T} =$$

$$= 360 \times ((50\text{ns} + 83\text{ns}) + 5\text{ns} + 5\text{ns} + 50\text{ns} + (16\text{ns} + 50\text{ns})) \times 120\text{kHz} =$$

$$= 11.18^{\circ}$$

The calculated value is the minimum angle. For accounting for some of the above assumptions (gate drivers and MOSFET's propagation times) an angle of 15 $^{\circ}$  is selected.

The required  $U_{sec}$  for producing 1.5kW in iron vessel with the new angle ( $\varphi = 15^{\circ}$ ) is:

$$U_{sec} = \frac{\pi}{4} \sqrt{2} \frac{P}{I_{iron} \cos \alpha_{iron}} = \frac{3.14}{4} \sqrt{2} \frac{1500}{20 \times \cos 15^{\circ}} = 86.2 \quad (3.56)$$

Comparing the values calculated with  $\varphi_{iron} = 0$  (3.27) and the  $U_{sec}$  calculated by (3.56) reveals that the difference is approximately 2V. The difference leads to turn ratio of:

$$n = \frac{U_{pr,FB}}{U_{sec}} = \frac{390}{86.2} = 4.5 \quad (3.57)$$

and currents:

$$I_{pr,AL,FB} = \frac{I_{coil,AL}}{n} = 17.55\text{A} \quad (3.58)$$

$$I_{pr,iron,FB} = \frac{I_{coil,iron}}{2} = 4.44\text{A} \quad (3.59)$$

The new transformer ratio will change  $f_{sw,AL}$ . However, the change will be small and will be measured further in the master thesis by means of simulations.

### 3.3.2.1 Calculation of Snubber Capacitors

For calculation of the required snubber capacitors the stored charge in the inductive components (coil, leakage inductance of the matching transformer and parasitic inductances) can be used. In the case of iron cooking vessel, full power (1,5kW) and  $\varphi = 15^\circ$  the stored charge is:

$$\begin{aligned}
 Q_L = idt &= \int_{180-\alpha_{iron}}^{\pi} I_{pk,pr,iron,FB} \sin(\omega_{iron}t) dt \\
 &= \frac{I_{pk,pr,iron,FB}}{2\pi f_r} (\cos(180 - \varphi_{iron}) - \cos \pi) = \\
 &= \frac{6.3}{2 \times 3.14 \times 116\text{kHz}} (\cos 165^\circ - \cos 180^\circ) = 294\text{nC} \quad (3.60)
 \end{aligned}$$

where:

$$I_{pk,pr,iron} = \sqrt{2}I_{pr,iron} = \sqrt{2} \times 4.44 = 6.3\text{A} \quad (3.61)$$

and the maximum snubber capacitors which will not lead to none ZV turn-on:

$$4C_{snub} = \frac{Q_L}{U_C} = \frac{294\text{nC}}{2 \times 390} = 188\text{pF} \quad (3.62)$$

where:

$f_r$  is used assuming that  $\alpha_{iron}$  will not contribute significantly to frequency change;

$C_{snub}$  is multiplied by 4 because the calculated charge is divided between the 4 capacitors.

According to the datasheet, the output capacitance ( $C_{oss}$ ) of IPW60R070C6 is 20nF at  $U_{DS} = 0\text{V}$  and becomes 100pF at  $U_{DS} = 200\text{V}$ . Because of non-linearity of output capacitance, it is difficult for the required additional capacitance in parallel of the MOSFET to be predicted. The value can best be selected practically. Because of this no snubber capacitors will be selected at this stage. Further investigations will be carried out during the practical design.

The calculated value is in case of full power. At lower power ratings the energy will not be sufficient to percharge the capacitors. However, this will not lead to hard switching as the voltage across the switch will be lower than  $U_{dc}$ . The additional losses in this case can be calculated by:

$$P_{turn-on} = \frac{1}{2}U_{cap}^2 C_{snub} \quad (3.63)$$

where;

$U_{cap}$  – voltage across the capacitor at the moment when the switch is turned on.

In that way, the turn-on losses will be compensate by reduced conduction and turn-off losses and will not lead to destruction of the MOSFETs.

### 3.3.2.2 Estimation of the Losses in the MOSFET

The  $P_{sw}$  and  $P_{cond}$ , this time, will be calculated with the help of SW package for circuit simulation – PLECS [69]. The package includes models of MOSFET and Diode with customisable parameters. In such a way the contribution of drain-source ( $C_{DS}$ ) capacitance can be accounted for.

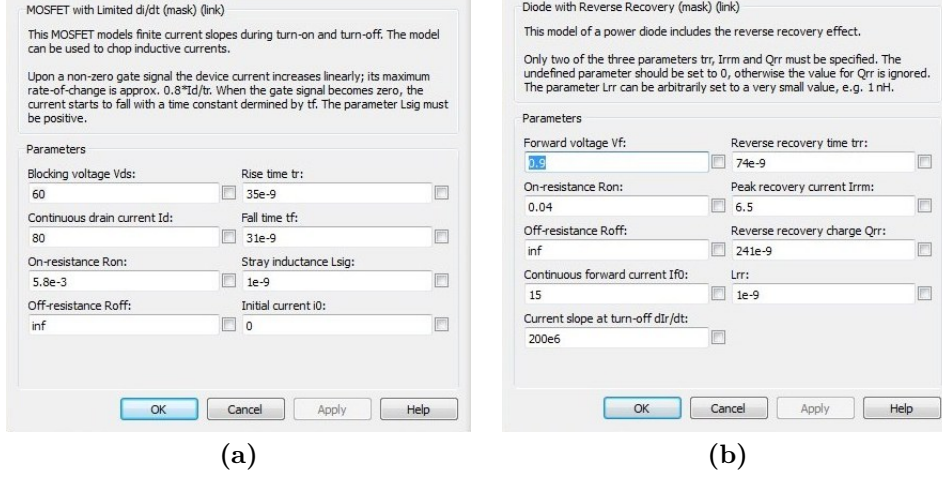


**Fig 3.14.** PLECS customisable components menus. (a) MOSFET and (b) Diode.

The obtained waveforms and some of the values are shown on Fig. 3.15. In the simulation the following parameters were used:

- Parameters of the MOSFETs according to Table 3.9;
- $L_{coil} = 22\mu\text{H}$ ,  $C_r = 85\text{nF}$ ,  $R_{ek} = 0.194\Omega$ ,  $U_{dc} = 390\text{V}$ ,  $C_{snub} = 188\text{pF}$  (the MOSFET model in PLECS does not include capacitive behaviour; because of this the calculated value for the snubber capacitors was used in the simulations) and  $f_{sw} = 119.6\text{kHz}$ ;
- The average power delivered to load was  $P \approx 1.5\text{kW}$

From Fig. 3.15 it can be seen that the main losses are due to conduction and are:

$$P_{cond,AL} = E_{cond}f_{sw} = (140.7\mu\text{J} + 17.8\mu\text{J}) \times 119.6\text{kHz} = 18.96\text{W} \quad (3.64)$$

$$P_{sw,AL} = E_{sw}f_{sw} = 27.2\mu\text{J} \times 119.6\text{kHz} = 3.25\text{W} \quad (3.65)$$

The contribution of the freewheeling diode to losses is approximately 2W. The parameters of the diode according to datasheet are:  $U_F = 0.4\text{V}$  and  $R_F = 20\text{m}\Omega$ .

In that way the total losses per MOSFET are:

$$P_{tot} = P_{cond} + P_{sw} + P_{diode} = 18.96 + 3.25 + 2 = 24.21\text{W} \quad (3.66)$$

The error which theoretical calculation of  $P_{cond}$  give is:

$$P_{cond,calc} = \frac{\sqrt{2}}{2} I_{pr,AL} R_{DS,on} = \frac{\sqrt{2}}{2} \times 17.55 \times 0.13 = 20.02\text{W} \quad (3.67)$$

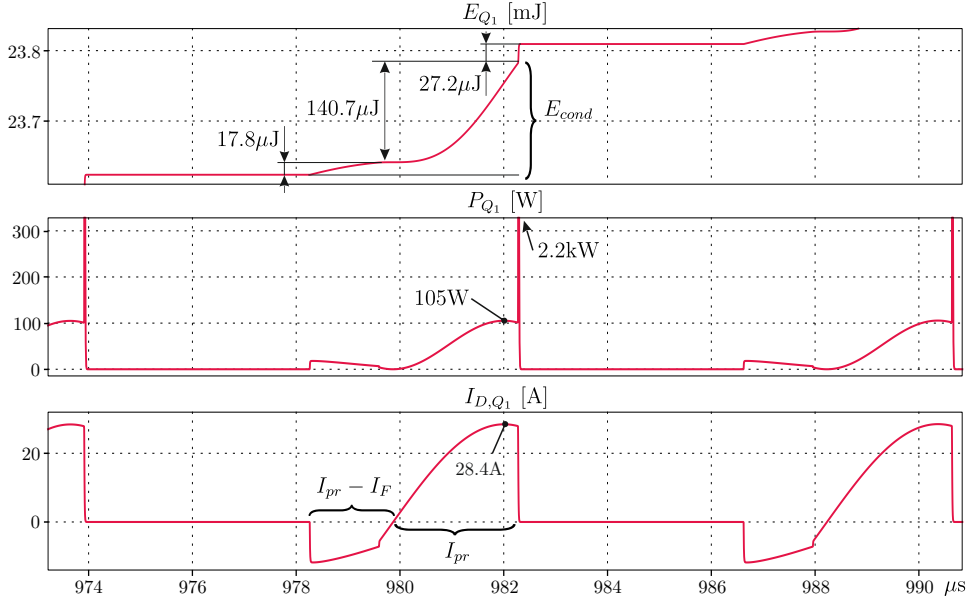


**Fig 3.15.** Simulation results of energies, losses and  $I_D$ .

$$P_{error} = |P_{cond} - P_{cond,calc}| = |20.96 - 20.02| \approx 1W \Rightarrow 4.49\% \quad (3.68)$$

which is small enough to justify the assumption made in calculating (3.44).  
The case temperature per MOSFET is:

$$T_c = 0.8T_{j,max} - P_{tot}R_{jc} = 0.8 \times 150 - 24.21 \times 0.32 = 112.25^\circ\text{C} \quad (3.69)$$

and the maximum heatsink resistance for 4 MOSFET in case  $T_a = 50^\circ\text{C}$  is:

$$R_{hs} = \frac{T_c - T_a}{4P_{tot}} = \frac{112.25 - 50}{4 \times 24.21} = 0.64^\circ\text{C/W} \quad (3.70)$$

The calculated  $R_{hs}$  does not differ very much from the one calculated for Half Bridge topology ( $R_{hs,HB} = 0.98/2 = 0.49^\circ\text{C/W}$ ), however the dissipated power (and the thermal stress) in the switches in case of Full Bridge is lower. Further the power is divided between four switches and covers large area than in case of Half Bridge. Both factors will increase the reliability of the unit and will increase the life of the switches. Additionally, the selected switches for Full Bridge cost 2.8 times less than the selected switches for Half Bridge.

A suggestion for suitable heatsink will not be made here considering that the unit might contain several inverters attached to one heatsink.

### 3.3.2.3 Transformer Design

The design of the transformer is based on selection of appropriate core, calculation of the required number of turns and verification whether the number of turns can be accommodated in the window area of the core.

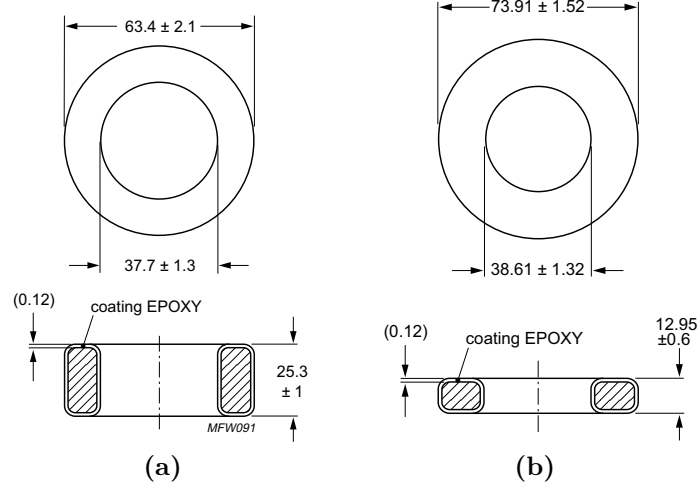


**Fig 3.16.** Toroidal ferrite cores produced by Ferroxcube (a) TX63/38/25 and (b) TX74/39/13 [70].

The shape of the transformer is selected to be toroidal (toroidal core gives the maximum efficiency) made of F3F material produced by Ferroxcube [70]. The manufacturer produces two type of cores suitable for the design – TX63/38/25 and TX74/39/13 (Fig. 3.16) [70]. From the figure it can be seen that both cores have similar dimension with only difference in the height. In the master thesis TX74/39/13 cores is selected as it has lower profile than TX63/38/25 which could be beneficial during the enclosure design. In order copper losses to be kept low 3 staked cores are selected for the design.

For calculation of the number of turns the approach described in [53] is adopted<sup>9</sup>. With the selected core the number of turns are:

$$n_p = \frac{U_{pr}}{3A_e B_{pk} k f_{r,noload}} = \frac{390}{3 \times 208\text{mm}^2 \times 0.1 \times 4 \times 67.2\text{kHz}} = 23.25\text{turns} \quad (3.71)$$

where:

$A_e$  – effective area of the core [ $\text{m}^2$ ] ( $A_e = 208\text{mm}^2$ ) [70];

$B_{pk}$  – peak magnetic induction [T];

$k$  – voltage waveform coefficient ( $k = 4$  for squarewave [53]);

$f_{r,noload}$  – no load resonant frequency of the resonant network [Hz].

In (3.71)  $f_{r,noload}$  is used as it leads to the lowest induced voltage in the winding and hence the highest number of turn. The value of the peak magnetic induction is selected 0.1T in order core losses to be kept low.

Because the required turn ration is  $n = 4.5$  the primary number of turns is selected to be  $n_{pr} = 22$ . In that way the secondary number of turns are:

<sup>9</sup>In [54] is described approach which aims to equalize the core losses and the copper losses. The approach is suitable for cores which have direct contact to air. In the current design, as the ring core is selected, the windings will limit the core's contact with the air. In that way the temperature of the core will have a higher value than the windings due to heating by windings and limited cooling.

$$n_{sec} = \frac{n_{pr}}{4.5} = \frac{22}{4.5} = 4.89 \Rightarrow 5 \text{ turns} \quad (3.72)$$

and the turn ratio is:

$$n = \frac{n_{pr}}{n_{sec}} = \frac{22}{5} = 4.4 \quad (3.73)$$

The maximum peak magnetic induction with the selected  $n_p$  in case of inverter switching at the full load resonant frequency is:

$$B_{max, pk} = \frac{U_{pr}}{3A_e n_p k f_{r, load}} = \frac{390}{3 \times 208 \text{mm}^2 \times 22 \times 4 \times 116 \text{kHz}} = 61 \text{mT} \quad (3.74)$$

On Fig. 3.17 is shown the losses in the core in function of  $B_{pk}$  for different frequencies. From the figure it can be seen that losses will be higher at no load ( $f_{r, no load}$ ). However, working of the induction cooker with no load will lead only to use of energy for heating the inverter and the resonant network which is meaningless. Because of this, it is assumed that the induction cooker will be able to detect the load and work only when a load is present. In that way the worst case is for  $f_{sw} = 116 \text{kHz}$ . From the figure it can be seen that at this frequency and  $B_{pk} = 61 \text{mT}$  the losses in the material are  $28 \text{kW/m}^3$ . From here the total losses in the stacked cores are:

$$P_{losses, core} = 3V_e P_{mat} = 3 \times 34300 \text{mm}^3 28 \text{kW/m}^3 = 2.88 \text{W} \quad (3.75)$$

where:

$V_e$  – effective volume of the core [ $\text{m}^3$ ] [70];

$P_{mat}$  – losses in the material at specified values of  $B_{pk}$  and  $f_{sw}$  [ $\text{kW/m}^3$ ] (Fig. 3.17).

The losses are low and easily can be dissipated by the area of the core.

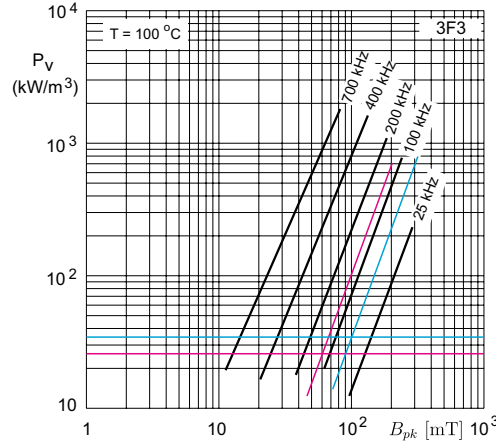


**Fig 3.17.** Losses in F3F material in function of magnetic induction for different frequencies [70].

For the design of the transformer's windings a litz wire is selected. For the secondary side is selected the litz wire used in the coil design (Table 3.5). For the primary side's the

litz wire shown on Table. 3.10 is selected. AWG46 is selected because the AWG46 strand gives lower losses than the AWG44<sup>10</sup> (Fig. 3.4). The litz wire's OD is selected so that the current density in the wire to be sufficiently low:

$$J_{pr} = \frac{4I_{pr,AL,FB}}{\pi OD_{pr}^2} = \frac{4 \times 17.55}{3.14 \times (3\text{mm})^2} = 2.48\text{A/mm}^2 \quad (3.76)$$

**Table 3.10.** Parameters of litz cable for the primary windings .

Strand type	OD <sub>pr</sub> [mm]	n <sub>s</sub>	R <sub>dc</sub> [mΩ/m]	Construction
AWG46	3	2700	6.1	5x5x3/36/46)

The winding area of the core is:

$$W_c = \frac{\pi d_{in}^2}{4} = \frac{3.14 \times 38.61^2}{4} = 1170.22\text{mm}^2 \quad (3.77)$$

where:

$d_{in}$  – the inner diameter of the core (Fig. 3.16(b)) [mm].

and the area occupied by the winding is:

$$W_w = (W_{pr} + W_{sec}) FF_w = (155.43 + 129.32) \times 1 = 284.75\text{mm}^2 \quad (3.78)$$

with

$$W_{pr} = n_{pr} \frac{\pi OD_{pr}^2}{4 FF_{pr}} = 22 \frac{3.14 \times 3^2}{4 \times 1} = 155.43\text{mm}^2 \quad (3.79)$$

and

$$W_{sec} = n_{sec} \frac{\pi OD_{sec}^2}{4 FF_{sec}} = 5 \frac{3.14 \times 5.74^2}{4 \times 1} = 129.32\text{mm}^2 \quad (3.80)$$

where:

$W_{pr}$  – area occupied by primary winding [mm<sup>2</sup>];

$W_{sec}$  – are occupied by the secondary winding [mm<sup>2</sup>];

$FF_w$  – fill factor taking into account the none perfect arrangement between primary and secondary; for simplicity  $FF_w = 1$ <sup>11</sup>;

OD<sub>pr</sub> – overall diameter of the litz wire used for the primary winding [mm];

$FF_{pr}$  – fill factor for the primary winding; for simplicity  $FF_{pr} = 1$ <sup>12</sup>;

OD<sub>sec</sub> – overall diameter of the litz wire used for the secondary winding [mm];

<sup>10</sup>The litz cable bunched with AWG48 are produced in OD = 2.36mm and OD = 4mm which will give either too high current density, in the former case, or will require a large window area, in the latter case.

<sup>11</sup>The real value depends on the arrangement of the windings in the layers. In the worst case it cannot decrease below 0.785 [54].

<sup>12</sup>The value is between 0.95 and 1 as each, primary and the secondary winding, occupies only one layer (the inner circumference of the core is  $C_{core} = \pi d_{in} = 3.14 \times 38.6\text{mm} = 121.2\text{mm}$  while  $C_{pr} = n_{pr} OD_{pr} = 22 \times 3 = 66\text{mm}$  and  $C_{sec} = n_{sec} OD_{sec} = 5 \times 5.74\text{mm} = 28.7\text{mm}$ ) [54].

$FF_{sec}$  – fill factor for the secondary winding; for simplicity  $FF_{sec} = 1$ .

From (3.77) and (3.78) it can be seen that  $W_c \gg W_w$  and core's winding area can accommodate the total number of turns (even at  $FF_w = 0.785$ ,  $FF_{pr} = 0.9$ , and  $FF_{sec} = 0.9$ ).

The losses in the windings can be approximated by:

$$W = \frac{d_{out,max} - d_{in,min}}{2} = \frac{75.43 - 37.29}{2} = 19.07\text{mm} \quad (3.81)$$

$$h_{tot} = 3h_{core,max} = 3 \times 13.55 = 40.65\text{mm} \quad (3.82)$$

$$L_{pr} = 2n_{pr}(W + h_{tot} + OD_{pr}) = 2 \times 22 \times (19.07 + 40.65 + 3) \times 10^{-3} = 2.76\text{m} \quad (3.83)$$

$$\begin{aligned} L_{sec} &= 2n_{sec}(W + h_{tot} + 2OD_{pr} + OD_{sec}) = \\ &= 2 \times 5 \times (19.07 + 40.65 + 2 \times 3 + 5.74) \times 10^{-3} = 0.715\text{m} \end{aligned} \quad (3.84)$$

$$R_{dc,pr} = R_{dc,litz,pr}L_{pr} = 6.1\text{m}\Omega \times 2.76 = 16.84\text{m}\Omega \quad (3.85)$$

$$R_{dc,sec} = R_{dc,litz,sec}L_{pr} = 2.45\text{m}\Omega \times 0.715 = 1.75\text{m}\Omega \quad (3.86)$$

$$R_{ac,pr} = R_{ac,coef,pr}R_{dc,pr} = 1.17 \times 16.84\text{m}\Omega = 19.7\text{m}\Omega \quad (3.87)$$

$$R_{ac,sec} = R_{ac,coef,sec}R_{dc,sec} = 1.11 \times 1.75\text{m}\Omega = 1.94\text{m}\Omega \quad (3.88)$$

$$P_{losses,pr} = I_{pr,AL}^2 R_{ac,pr} = 20^2 \times 19.7\text{m}\Omega = 7.88\text{W} \quad (3.89)$$

$$P_{losses,sec} = I_{sec,AL}^2 R_{ac,sec} = 79^2 \times 1.77\text{m}\Omega = 12.12\text{W} \quad (3.90)$$

where:

$W$  – width of the core [m];

$d_{out,max}$  and  $d_{in,max}$  – maximum outer and inner diameters of the core [m];

$h_{tot}$  – total height of the three stacked cores [m];

$h_{core,max}$  – maximum height of single core [m];

$L_{pr}$  and  $L_{sec}$  – length of the primary and secondary litz wires [m];

$OD_{pr}$  and  $OD_{sec}$  – overall diameters of the litz wires used in the primary and secondary windings [m];

$R_{dc,pr}$  and  $R_{dc,sec}$  – DC resistances of the primary and secondary windings [ $\Omega$ ];

$R_{dc,litz,pr}$  and  $R_{dc,litz,sec}$  – DC resistances of the litz wires used in the primary and the secondary windings [ $\Omega/m$ ];

$R_{ac,pr}$  and  $R_{ac,sec}$  – AC resistances of the primary and the secondary windings [ $\Omega$ ];

$R_{ac,coef,pr}$  and  $R_{ac,coef,sec}$  – AC contribution to  $R_{dc}$  for the primary and secondary windings calculated by (3.16);

$P_{losses,pr}$  and  $P_{losses,sec}$  – power losses in the primary and the secondary windings [W].

In (3.83) and (3.84) it is assumed that the litz wires is closely wound to the walls of the core. In reality the windings will have some radius of winding which will increase slightly the calculated values. However, due to its small contribution it is ignored here. The OD in both equation is used in order the contribution of the layer to the mean length per turn to be accounted for.

In that way the losses in the transformer are:

$$\begin{aligned} P_{losses,tr} &= P_{losses,core} + P_{losses,pr} + P_{losses,sec} = \\ &= 2.88 \times 7.88 \times 12.12 = 22.88\text{W} \end{aligned} \quad (3.91)$$

From (3.91) it can be seen that the losses in the core are lower than the losses in the windings. However, considering that the two windings cover the core and, in that way, heat additionally the core and limit its thermal radiation and convection, the value is appropriate for the design.

An approximate thermal design can be carried out by a FEM analysis. However the thermal design is not considered in the master thesis.

### 3.4 Theoretical Efficiency of the Complete System

The total losses in the inverter are:

$$P_{losses,inv} = 4P_{tot} = 4 \times 24.21 = 96.84\text{W} \quad (3.92)$$

From here the losses in the whole system are:

$$P_{losses,sys} = P_{losses,coil} + P_{losses,inv} + P_{losses,tr} = 219 + 96.84 + 22.88 = 338.72\text{W} \quad (3.93)$$

In (3.93) the losses in the resonant capacitor are not included due to absence of the losses ( $\tan \delta$ ) in the datasheet of the manufacturer.

The theoretical efficiency of the system is:

$$\eta_{th} = \frac{P_{joule}}{P_{joule} + P_{losses,sys}} = \frac{1500}{1500 + 338.72} = 0.81 \quad (3.94)$$

which is still higher than the smooth electric cooktops (74.2%).

The required input power is:

$$P_{in} = P_{joule} + P_{losses,sys} = 1500 + 338.72 = 1838.72\text{W} \quad (3.95)$$

The total power in the output of the inverter in case of aluminum cooking vessel is:

$$S_{AL} = \frac{4 U_{dc} I_{coil,AL}}{\pi \sqrt{2} n} = \frac{4 \cdot 390 \cdot 79}{3.14 \sqrt{2} \cdot 4.4} = 6.3\text{kVA} \quad (3.96)$$

### 3.5 Design Outputs

The output of the theoretical design is:

#### Inverter

- Topology – Full Bridge;
- Switches – IPW60R070C6;
- no lossless snubbers;

#### Transformer

- turns ration  $n = 4.4$ ;
- primary number of turns  $n_{pr} = 22$  wound with litz wire with OD = 3mm and AWG46;
- secondary number of turns  $n_{sec} = 5$  wound with litz wire with OD = 5.74mm and AWG44;

#### Resonant Network

- coil dimensions –  $d_1 = 200\text{mm}$ ,  $d_2 = 40\text{mm}$  and  $t_{gap} = 5\text{mm}$ ;
- coil design according to Fig. 3.5(b) with  $n_{first} = 15$  and  $n_{second} = 5$ ;
- litz wire with OD = 5.74mm and AWG44;
- $L_{noload} = 66\mu\text{H}$ ,  $L_{load} = 22\mu\text{H}$ ;
- $C_r = 2 \times 170\text{nF}$ ;

## Chapter 4

# Simulation Results

### 4.1 Simulation Setup

In order the control idea to be used for control of induction heating inverter, several changes have been made to the circuit presented in Fig. 1.15(a) which, for convenience, is presented in this part of the master thesis also (Fig. 4.1).

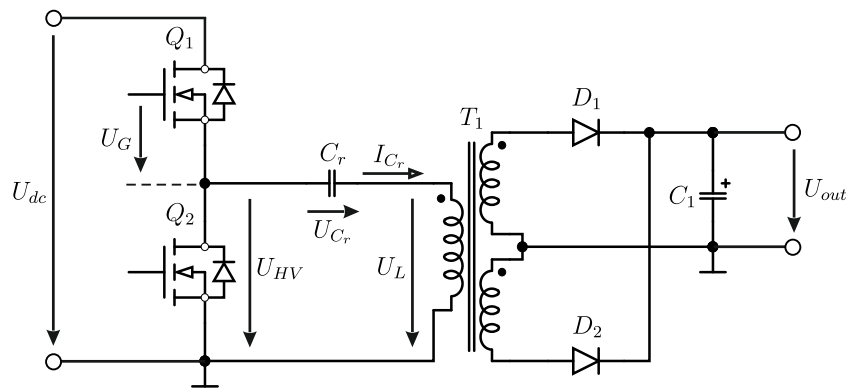


**Fig 4.1.** LLC DC-DC resonant converter. Copy of Fig. 1.15(a).

From Fig. 4.1 it can be seen that in LCC resonant converters the resonant capacitor ( $C_r$ ) is located in the primary side of the transformer. This is done for two reasons. First  $C_r$  is used for blocking the DC voltage and eliminating the need of additional blocking capacitor. Secondly,  $C_r$  resonates with the leakage inductance, or leakage inductance and magnetizing inductance in cases of no load, of the transformer where the current is bidirectional. The current in the secondary, due to the diodes, for series connection of capacitor is unidirectional. Moving  $C_r$  in the secondary side, in this case, will only charge the capacitor to voltage related  $U_{dc}$  and  $n$  eliminating the resonant network <sup>1</sup>.

<sup>1</sup>With single secondary winding and full bridge rectifier the resonant network can be formed. However, this requires 2 additionally diodes and decrease the efficiency of the converter.

In the induction heating the current in the primary and secondary is bidirectional. Because of this,  $C_r$  can be located either in the primary or in the secondary side of the transformer. Keeping the capacitor in the primary side, however, will reduce its value  $n^2$  times compared to the case when it is located in the secondary side. This will lead to high voltage across the capacitor and the transformer. For instance, in the case of full power and aluminum pan the voltage across  $C_r$  is:

$$U_{C_r,pr} = nU_{C_r,sec} = 4.4 \times 2 \times 646 = 5.68\text{kV} \quad (4.1)$$

A capacitor with such ratings has large dimension, requires extra creepage distance, imposes challenge in design of high voltage transformer and increases the copper losses. That is why  $C_r$  is moved to the secondary side of the transformer (Fig. 3.12).

Further, for achieving a better start-up and stability the IC is designed to track the voltage across the primary side of the transformer ( $U_L$  on Fig. 4.1) instead of  $U_{C_r}$ . In induction heating the voltage across the primary side cannot be used because  $C_r$  is situated in the secondary side. The required voltage is represented by the voltage across the coil (sum of  $U_{L_{coil}}$  and  $U_{R_{ek}}$  in Fig. 3.12). Because of this the sampling is moved in the secondary side of the transformer.

The effect of sampling the coil voltage ( $U_{coil}$ ) instead of  $U_{C_r}$  is shown on Fig. 4.2. From the figure it can be seen that  $U_{coil}$  has a voltage jump at the moment when one of the switch pairs is turned ( $t_0$  or  $t_1$ ) while  $U_{C_r}$  is pure sine wave. This, however, does not influence the control approach as long as the magnitude of  $\Delta U_{C_r}$  is calculated correctly. For this reason the turn-off limits in this case are calculated by:

$$U_{C_r,high} \geq \frac{\Delta U_{C_r}}{2} - \frac{U_{dc}}{2n} \quad (4.2)$$

$$U_{C_r,low} \leq \frac{U_{dc}}{2n} - \frac{\Delta U_{C_r}}{2} \quad (4.3)$$

and the power delivered to load in this case is:

$$P = U_{dc}I_{dc} = U_{dc} \frac{2f_{sw}C_r\Delta U_{C_r}}{n} \quad (4.4)$$

The switches are turned-on when the voltage across them becomes zero or a valley is detected (Fig. 1.14).

With this changes, the developed control idea is implemented in the Matlab language and simulated with the help of Matlab Simulink (Fig. 4.3) (the source code is given in **Appendix A**).

In the schematic:

- switches are ideal with RC snubbers with  $R = 1\text{m}\Omega$  and  $C = 188\text{pF}$ ;
- the transformer ratio of T1 is 4.4:1;
- resonant network's components have values of  $C_r = 85\text{nF}$ ,  $L_{coil} = 22\mu\text{F}$  and  $R_{ek} = R_{ek,AL}$  or  $R_{ek} = R_{ek,iron}$ ;
- $U_{dc} = 390\text{V}$ ;
- the value of  $V_{m1}$  ( $U_{pr}$ ) is used for controlling the turn-on of the switches;
- $V_{m2}$  ( $U_{coil}$ ) is the feedback signal used for controlling the turn-off of the switches;

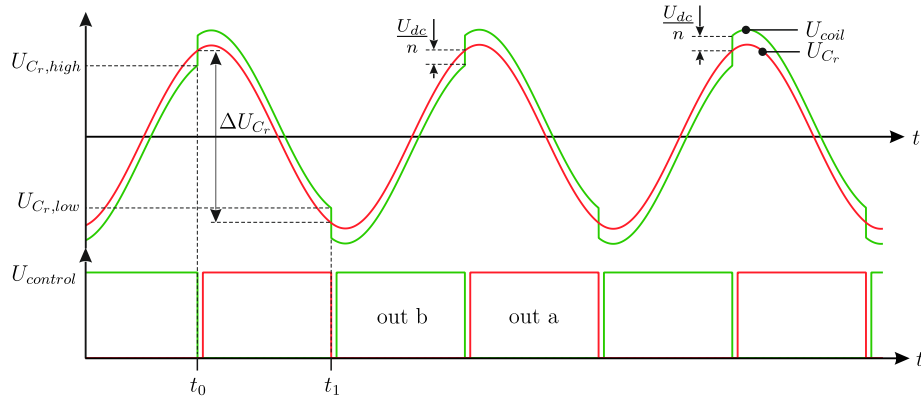


**Fig 4.2.** Difference between  $U_L$  and  $U_{C_r}$ .

- the additional signals supplied to algorithm are: the simulation time required for calculation of the switching frequency and the reference power.
- the output signals of the block are the control signals for the switches (out\_a and out\_b);

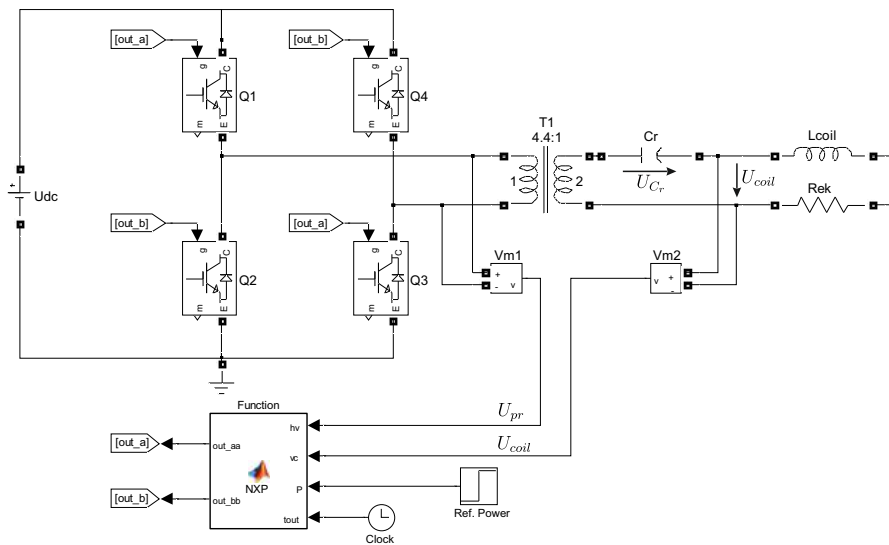


**Fig 4.3.** Used schematic during the simulations.

The algorithm works in the following way: in the beginning of the simulation (0 Fig. 4.4) out\_a is turned on for defined period of time and turned off after end of this time ( $t_0$ ). This injects energy in Lcoil and Cr and force them to start to resonate. After  $t_0$  the voltage across switches Q2 and Q4 is sensed. When it becomes lower than 10V out\_b is turned-on and the next half periods begins ( $t_1$ ). When condition (4.2) is fulfilled, the out\_b is turned-off ( $t_2$ ) and the algorithm begins to sense the voltage across Q1 and Q3. When this voltage

becomes  $<10V$ , out\_a is turned-on ( $t_3$ ) and algorithm waits for condition (4.3) to turn-off out\_a ( $t_4$ ). In that way the algorithm switch with a frequency dependable on the required power. The unknown in (4.2) and (4.3)  $\Delta U_{C_r}$  is calculated from (4.4) at the end of every period.

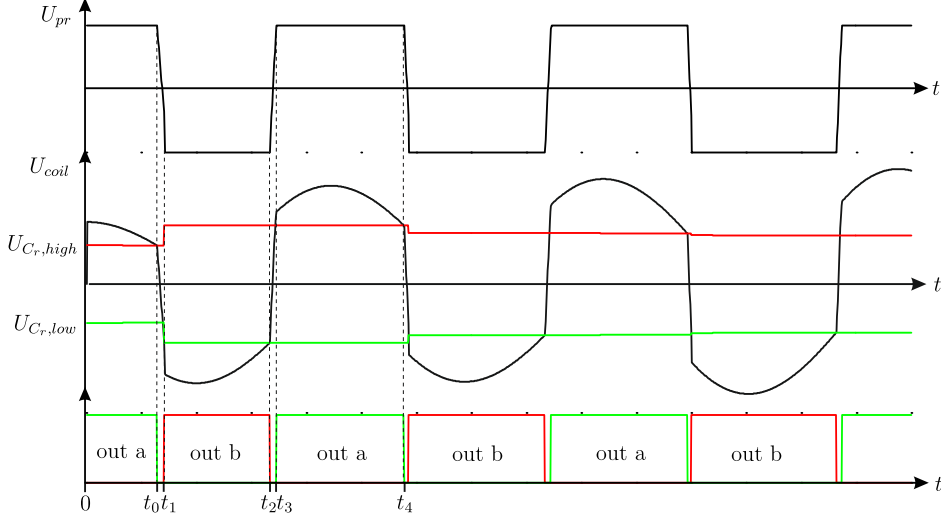


Fig 4.4. Starting up of implemented algorithm.

## 4.2 Simulation Results

The step response of the implemented controller and the change of  $f_{sw}$  in case of  $R_{ek} = R_{ek,AL}$  are shown on Fig. 4.5. The simulated waveforms are without power feedback and the required power is estimated only by calculating (4.4) in every half cycle. The output power is averaged by use of 2 order Butterworth low pass filter with cutting frequency of 15kHz.

From the figure it can be seen that the controller is capable of responding to changes in the reference power very quickly and without any overshoot. The small difference in the reference power ( $P_{ref}$ ) and power delivered to load ( $P_{R_{ek}}$ ) is due to calculation inaccuracies and snubber capacitors which contribute to the continuation of the energy flow after issuing a turn-off signal. The error can be eliminated by addition of power feedback. Further, from Fig. 4.5 it can be seen that there is no overshoot in the output power which shows the high stability of the system and its reduction to first order.

From the figure it can also be seen the small change of frequency required for changing the power with 1.2kW.

On Fig. 4.6 is presented the step response in case of  $R_{ek} = R_{ek,iron}$ . From the figure it can be seen that the step response is similar to case of  $R_{ek} = R_{ek,AL}$  and the only difference is in the switching frequency of the inverter. As expected the iron cooking vessel requires larger change of  $f_{sw}$  for reducing the power to 300W.

On Fig. 4.7 is shown the start up of the inverter in case of  $R_{ek} = R_{ek,iron}$  and the response of the system in case of step change of  $R_{ek} = R_{ek,iron}$  to  $R_{ek} = R_{ek,AL}$ . In the figure the averaged output power is substituted by the peak output power divided by 2 so

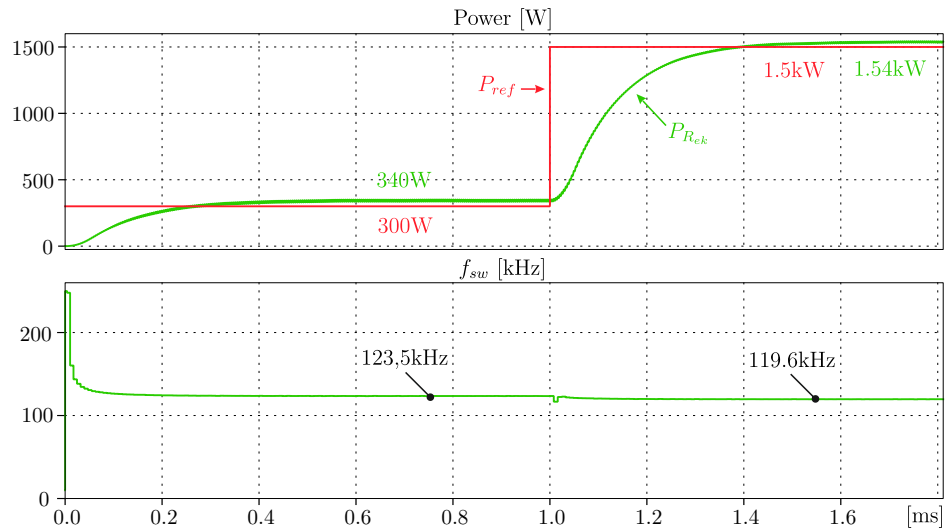


**Fig 4.5.** Step response of the output power and change of  $f_{sw}$  in function of power in case of aluminum cooking vessel.

that the real response of the system to be observable. The finite slop of  $P_{ref}$  is due to the fact that no logic for prevention of capacitive switching is implemented in the algorithm and the finite time required for increasing the energy in the resonant network to appropriate magnitudes. From the figure it can be seen that the system response very quickly and accurately to changes of the load.

For sake of comparison on Fig. 4.8 is shown the response of the system in case of step change of the load from iron to aluminum when the switches are driven with constant frequency of 120kHz. This represents a system of second order as described in §1.3.2. From the figure it can be seen that after the step change was applied the output power needs some time before it settles to the steady state value. By comparing Fig. 4.7 and Fig. 4.8 the influence of the controller can easily be notice.

From the simulation results it is clear that the idea successfully can be used in induction heating applications.

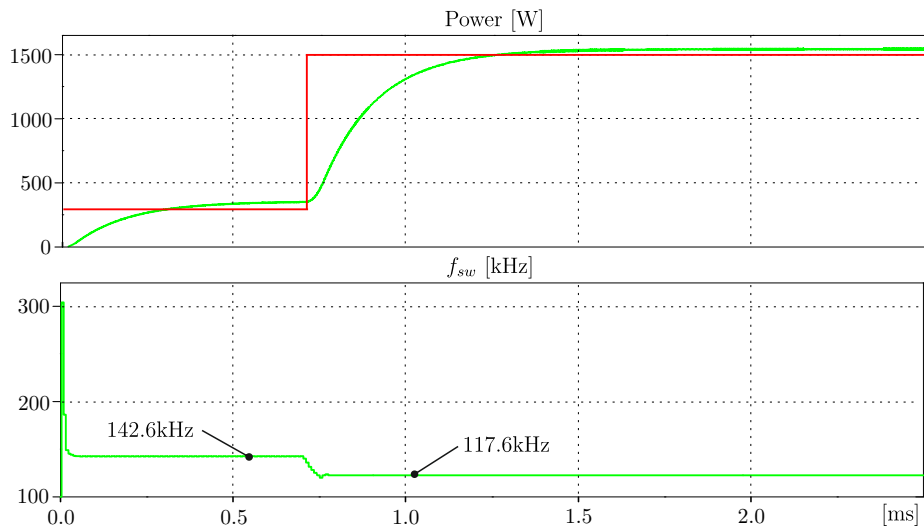


**Fig 4.6.** Step response of the output power and change of  $f_{sw}$  with power in case of iron cooking vessel.

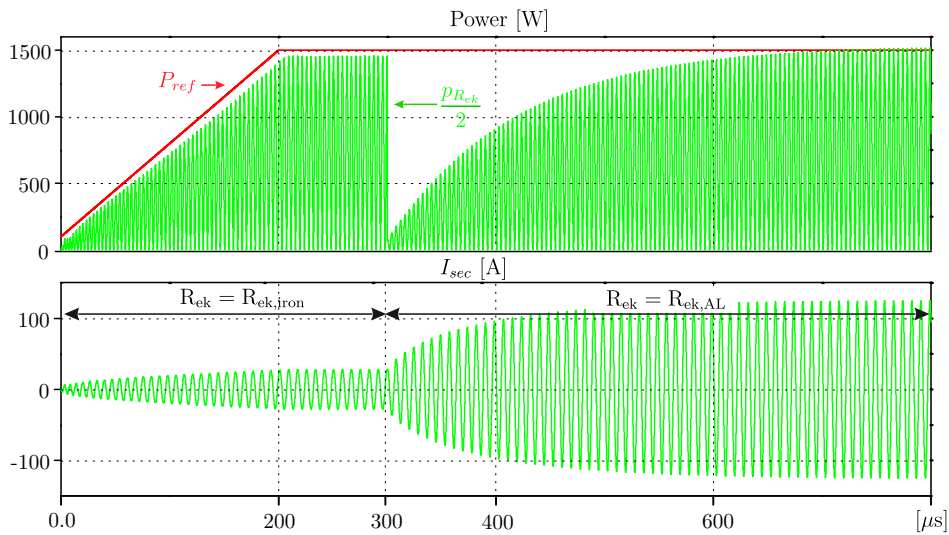


**Fig 4.7.** Response in case of step change of  $R_{ek} = R_{ek,iron}$  to  $R_{ek} = R_{ek,AL}$ .

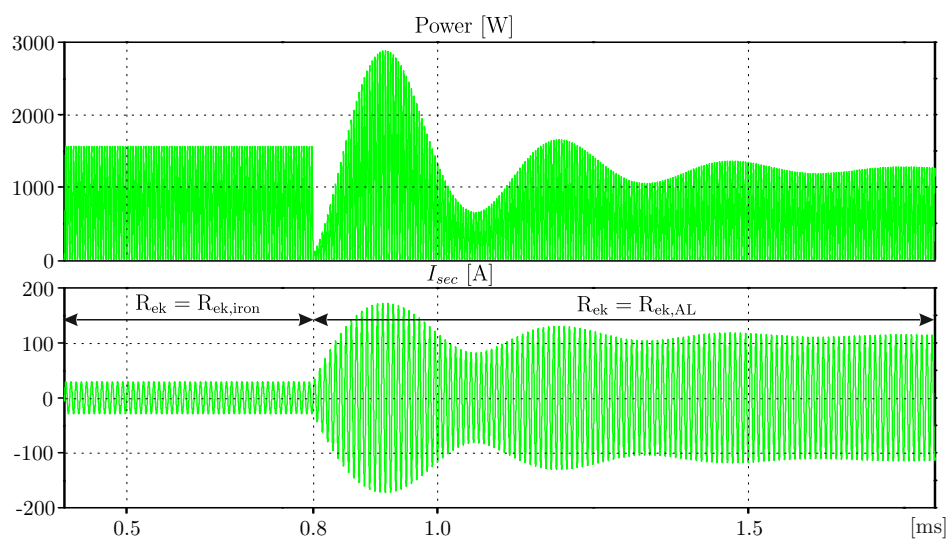


**Fig 4.8.** Response in case of step change of  $R_{ek} = R_{ek,iron}$  to  $R_{ek} = R_{ek,AL}$  with fixed switching frequency.



# Chapter 5

## Practical Design

In the practical design firstly the Half Bridge topology was used. After obtaining successful results, the topology was changed to Full bridge. The precaution was taken due to the fact that the IC is designed for control of Half Bridge topology which makes the initial testing easier.

### 5.1 Used Equipment

Power Supplies:

- Delta Elektronika SM400-AR-8 (0-400V, 4A) – used for supplying the inverter;
- Delta Elektronika E015-2 (0-15V, 2A) – used for supplying the control board;
- Delta Elektronika ES030-5 (0-30V, 5A) – used for supplying the hide side driver in the Half Bridge.

Oscilloscopes:

- LeCroy Waverunner 343 (350MHz, 2Gs/s);
- Yokogawa DLM 2024 (200MHz, 2.5Gs/s).

Voltage Probes:

- LeCroy PP007-WS (x10, 550MHz, 10M $\Omega$ , 10pF );
- Yokogawa 701938 (x10, 200MHz, 10M $\Omega$ ).

Current Probes:

- LeCroy CP030 (30A, 50MHz);
- Yokogawa 701933 (30A, 50MHz);
- Yokogawa 701929 (30A, 50MHz);
- Current transformers 1:40 and 1:60 (Fig. 5.1) with burden resistance of 6 $\Omega$ .

Infrared Thermometer:

- Fluke 574.

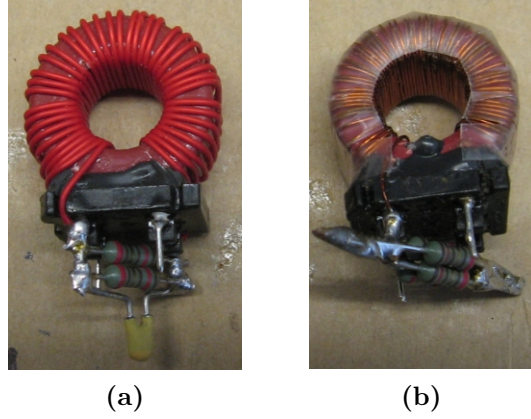


**Fig 5.1.** Current transformers used in the measurements. (a) 1:40 and (b) 1:60.

## 5.2 Half Bridge Inverter

### 5.2.1 Schematics and Practical Implementation

The control board used in the practical verification was designed by NXP. All other components have been designed by the author.

The appearance of the board is shown in Fig. 5.2 and the schematic on Fig. 5.3. On Fig. 5.4 and Fig. 5.5 is shown the Half Bridge inverter's schematic and a picture of the practical realization respectively. In Fig. 5.3 the Slope Gain (R7) and the Fdb (R8) trimmers are used for power regulation.  $U_{fb}$  is the feedback signal of the voltage across the coil (Fig. 5.4). The sensing of the voltage across the coil is implemented with capacitive divider formed by C16 and C19. The capacitance of C19 is fixed to 100nF and is SMD capacitor situated as close as possible to the feedback pin of the IC (**Sns Cap** Fig. 5.3). C16 is implemented as a series connection of 12pcs. 2.2nF 2kVDC ceramic capacitors connected in series (Fig. 5.2). The large number of serially connected capacitors is required due to high AC voltage which the capacitors must sustain. Also, it allows for changing the division ratio.

In the current version of the IC, the ratio between C16 and C19 sets the output power deviled to the load. The required value of C16 for achieving given power level can be calculated by:

$$C16 = C19 \frac{f_r C_r U_{sns,bus}}{P_{in} - f_r C_r U_{sns,bus}} [F] \quad (5.1)$$

where:

$U_{sns,bus}$  – voltage at the **Sns Bus** pin.

The above equation is valid for low power DC-DC converters where the maximum peak voltage  $U_L$  (Fig. 1.15) hardly exceeds the applied  $U_{DC}$  (Fig. 4.4). In the case of high power resonant converters, where the reactive power can be significant, the value of C16 is limited by the maximum voltage which the IC can sustain in the **Sns Cap** pin and the maximum peak voltage across the coil (Fig. 5.4). The voltage at **Sns Cap** is in range of 0-5V and must not be exceeded. Because of this in all practical design the ratio between C19 and C16

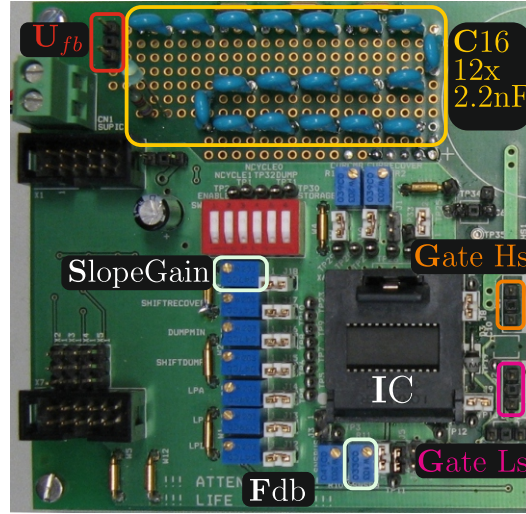


**Fig 5.2.** IC's test board.

is selected so that the divided peak-to-peak voltage does not exceeds 5V. The difference in the calculated value based on max. pk-pk voltage and the one calculated by (5.1) can be compensated by tuning R6.

The output power regulation, in the IC, is made to be regulated by changing the voltage on **Sns Fb** pin. The voltage range is between 1V and 3V as 3V being the maximum output power delivered to load and 1V zero power. The IC also has the capability of implementing Pulse Density Modulation (PDM) (Fig. 1.11(b)) depending on the voltage at **Sns Fb** pin. In the current design this level is set to 1.6V.

In the design, the **Sns Fb** pin, besides power regulation, is also intended to be used for output current limitation in case of no load. The latter is added in order MOSFETs to be protected during the tests<sup>1</sup>.

The current limitation is implemented by the current transformer CT1 (Fig. 5.4) an the circuit enclosed in dashed box in Fig. 5.3. The circuit works in the following manner: CT1 and R16 transform the primary current into voltage; the voltage is applied to voltage divider (R9 and R10) and after that feed to U2; in steady state U2 is turn off, however when the voltage in its input exceeds the threshold voltage of U2, U2 is turn on and in that way reduces the voltage at **Sns Fb**.

The Q1, Q3 and Q4, Q6 in the schematic of the Half Bridge are used as current booster due to limited output current driving capabilities of the IC's drivers. The diode (D3) and capacitors C10, C11 and C12 form a bootstrap network used for providing the required voltage and charge for turning on the upper MOSFET (Q2). The behavior of the circuit is as follow: when the lower switch (Q5) is turn on, the one end of the bootstrap capacitors becomes connected to ground through  $R_{DS,on}$  of Q5; if the voltage in the bootstrap capacitor is bellow  $15V - V_{F,D3}$ , D3 becomes forward biased and connects the bootstrap capacitors to  $V_{dd Hs}$  (+15V); in that way the capacitors are charged; when Q5 is turn off the voltage in the source of Q2, depending on current direction, becomes higher than +15V which reverse

<sup>1</sup>In the absence of load, according to the equivalent circuit Fig. 2.1, in the secondary side of the transformer only the  $R_{ac}$  of the coil will remain. This will force the IC to attempt to deliver 1.5kW, in case of full power, to the small AC resistance of the coil. This will increase significantly the current and destroy the MOSFETs.

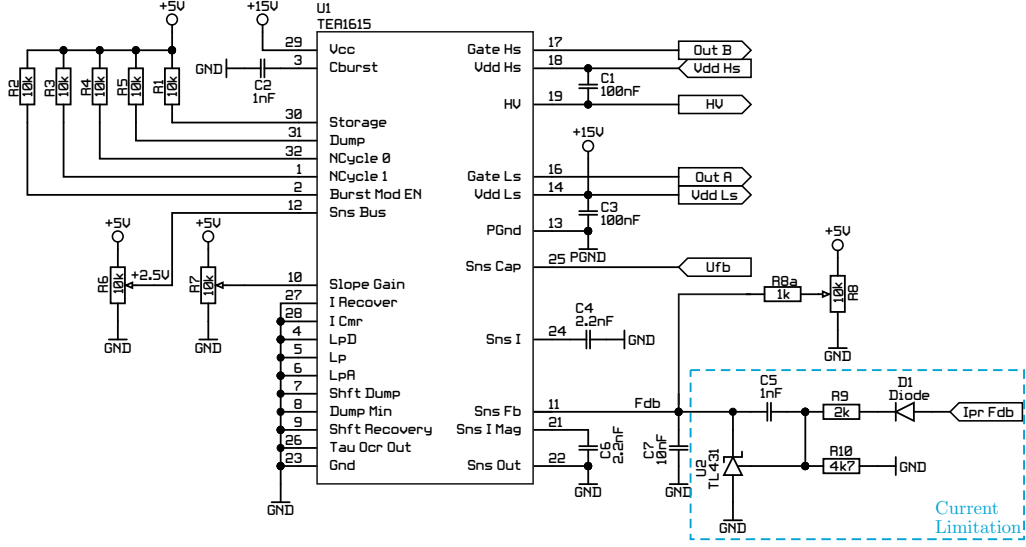


Fig 5.3. Schematic for the control board.

bias D3 and turns it off preserving the charge in the capacitors.

The required bootstrap capacitors can be calculated by [71]:

$$C_{boot} = \frac{Q_{gate, total}}{\Delta U_{boot}} S = \frac{255 \times 10^{-9}}{1} \times 15 = 3.82 \mu F \Rightarrow 4.7 \mu F \quad (5.2)$$

where:

$$Q_{gate, total} = Q_{gate} + (I_{lk, cap} + I_{lk, gs} + I_{qbs} + I_{lk} + I_{lk, diode}) \cdot t_{on} + Q_{ls} \quad (5.3)$$

$Q_{gate}$  – the total gate charge of the MOSFET;  $Q_{gate} = 170 \text{ nC}$  for  $U_{gate} = 0 - 10 \text{ V}$  [C];

$I_{lk, cap}$  – leakage current of the bootstrap capacitor [A];

$I_{lk, gs}$  – leakage current of the switch gate source capacitance [A];

$I_{q, bs}$  – quiescent current of the bootstrap circuit [A];

$I_{lk}$  – leakage current of the bootstrap circuit [A];

$I_{lk, diode}$  – leakage current of the bootstrap diode [A];

$Q_{ls}$  – charge required by the internal level shifter of the driver [C];

$t_{on}$  – on time of the high side switch [s];

$\Delta U_{boot}$  – pk-pk ripple voltage of the bootstrap capacitor [V];

$S$  – over-dimensioning factor.

In (5.3) the contribution of the currents and the level-shifter charge are ignored due to their low contribution and are taken in the account in the  $S$ . The given value of  $Q_{gate}$  is in case of 10V gate voltage. As the used maximum gate voltage in the design being 15V (50% higher)  $Q_{gate}$  is multiplied by 1.5. For testing purposes of IGBTs the bootstrap capacitors are selected with value higher that calculate one (Fig. 5.4).

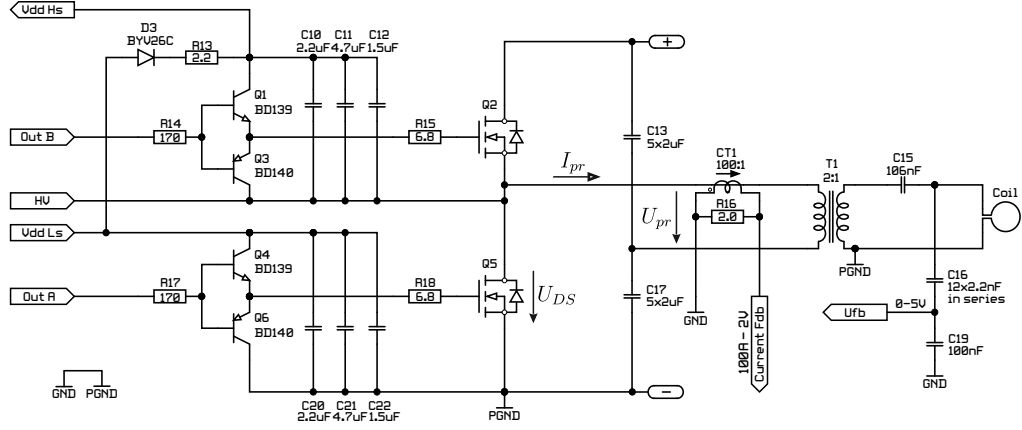


Fig 5.4. Half Bridge – schematic.

The gate resistances are selected so that the maximum peak current of 3A of the BJTs is not exceeded [72]:

$$R_G > \frac{U_{dc,IC}}{I_{C,max}} = \frac{15}{3} = 5\Omega \Rightarrow 6.8\Omega \quad (5.4)$$

where:

$U_{dc,IC}$  – supply voltage of current boost transistors equal to IC's drivers voltage (+15V);  
 $I_{c,max}$  – maximum collector current of the BJTs.

The value of R14 and R17 are:

$$R_B = R_G \beta_{min} = 6.8 \times 25 = 170\Omega \quad (5.5)$$

where:

$\beta_{min}$  – minimum current gain of BJT.

The value of C13 and C17 are calculated by (3.52). The MOSFETs are IPW60R070C6 according to Table 3.9.

The connection between the control board and the Half Bridge board was made by twisted pair wires with length less than 10cm. The cable used for sensing the voltage across the coil was also made by twisting wires with length less than 30cm.

For the design of the resonant capacitors 240pcs. of MKP capacitors with capacitance of 100nF and 1kVDC were used (Fig. 5.6(a)) [73]. The capacitors were connected 15 in series and 16 in parallel and the total capacitance was 106nF. In that way the voltage across the capacitor at 120kHz and  $I_{coil} = 79A$  will be:

$$U_{Cr} = \frac{I_{coil}}{2\pi f C} = \frac{79}{2 \times 3.14 \times 120\text{kHz} \times 106\text{nF}} = 989V \quad (5.6)$$

and across single capacitor:

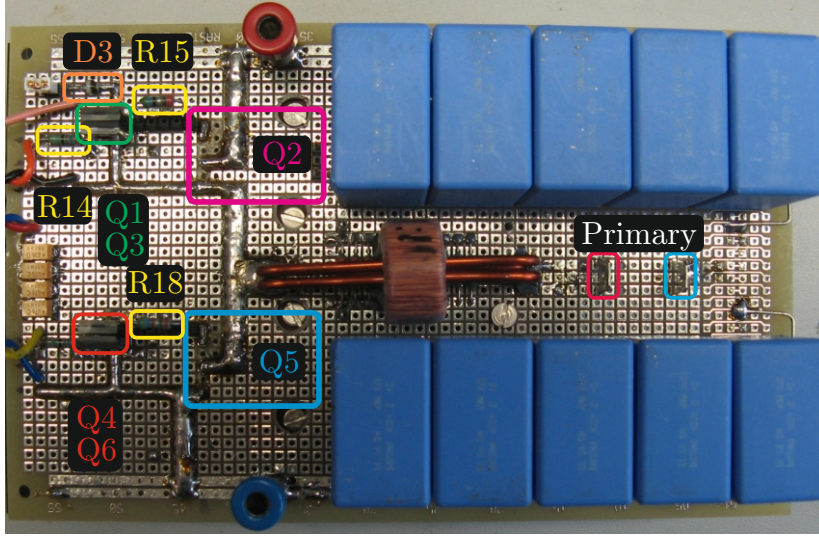


Fig 5.5. Half Bridge – practical realization.

$$U_{C_r, single} = \frac{U_{C_r}}{15} = \frac{989}{15} = 66\text{V} \quad (5.7)$$

On Fig. 5.6(b) is shown the maximum permissible AC voltage across a single capacitor in function of frequency [73]. From the figure it can be seen that at 120kHz and selected  $I_{coil}$  the applied voltage will exceeds with 26V the maximum allowed voltage of 40V. However, because of limited number of capacitors,  $U_{C_r}$  could not be reduced further.

The maximum power losses in single capacitor are [74]:

$$\begin{aligned} P_{C_r, losses} &= 2\pi f C U_{C_r, single}^2 \tan \delta = \\ &= 2 \times 3.14 \times 120\text{kHz} \times 100\text{nF} \times 66^2 \times 15 \times 10^{-4} = 0.59\text{W} \end{aligned} \quad (5.8)$$

which is within the limit of the 22.5mm pitch package [75].

The current through single capacitor is:

$$I_{cap, single} = \frac{I_{coil}}{16} = \frac{79}{16} = 4.9\text{A}$$

The designed coil is shown on Fig. 5.7. For the design a litz wire with strand type of AWG36 ( $d_s = 0.127\text{mm}$ ), OD = 5.94mm and  $n_s = 1050$  were used. The reason for using a litz wire with higher  $d_s$  that the selected on in chapter 3 is due to availability of such cable and the preliminary stage of the investigation.

The number of turns in the first layer were 17 and the number of turns in the second layer 6 (Fig. 3.5(b)). The mechanical supporting material was with thickness of 3mm and the dimensions of the coil were:  $d_1 = 220\text{mm}$ ,  $d_2 = 38\text{mm}$  and  $d_3 = 43\text{mm}$ . The measured inductance was  $L_{no load} = 66\mu\text{H}$ ,  $L_{load} = 22\mu\text{H}$ .

In that way the resonant frequencies are:

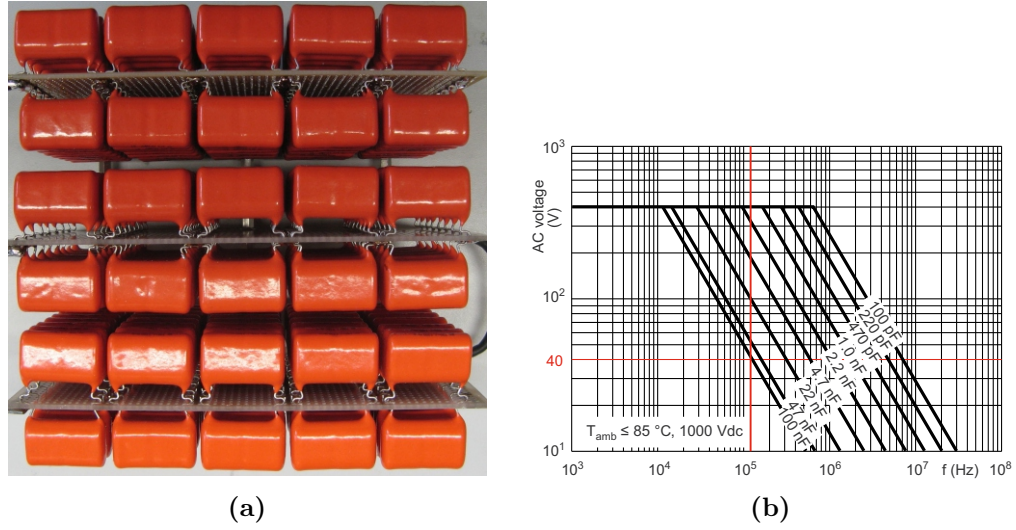


**Fig 5.6.** Resonant capacitor (a) practical realization and (b) AC voltage vs. frequency for single capacitor.

$$f_{r,load} = \frac{1}{2\pi\sqrt{C_r L_{load}}} = \frac{1}{2 \times 3.14 \times \sqrt{106\text{nF} \times 22\mu\text{H}}} = 104.27\text{kHz} \quad (5.9)$$

$$f_{r,noload} = \frac{1}{2\pi\sqrt{C_r L_{noload}}} = \frac{1}{2 \times 3.14 \times \sqrt{106\text{nF} \times 66\mu\text{H}}} = 60.2\text{kHz} \quad (5.10)$$

The matching transformer was designed by packing two toroidal cores with inner diameter of  $d_{inner} = 39\text{mm}$ , outer diameter  $d_{outer} = 73\text{mm}$  and height of single toroid of  $h = 12\text{mm}$ . In that way the area of the two cores was  $A_e = 408\text{mm}^2$ . The peak magnetic induction was set to  $B_{pk} = 0.1\text{T}$  @60kHz and, for half bridge, was calculated 10 turn for the primary winding and 5 turns were made in the secondary winding ( $n = 2 : 1$ ).

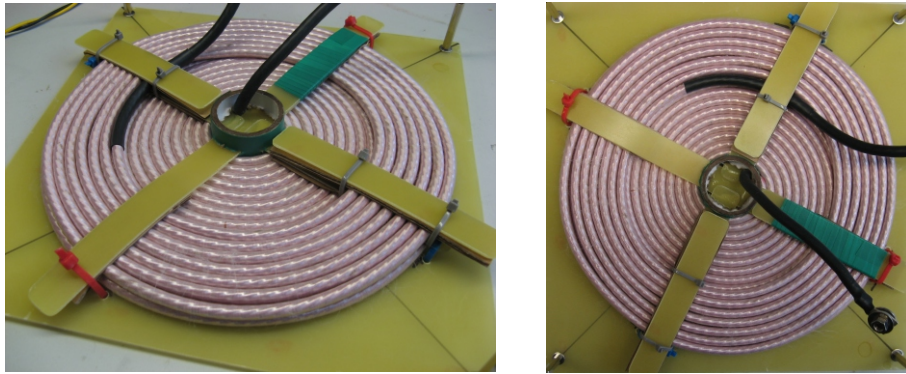


**Fig 5.7.** Practically designed coil.



**Fig 5.8.** The matching transformer.

The primary winding was made by litz wire with OD = 3.6mm, strand type AWG36 and  $n_s = 265$ . The secondary winding was made by the same litz wire as the one used for the design of the coil. A picture on the transformer is shown on Fig. 5.8.

### 5.2.2 Achieved Practical Results

In all practical tests the following settings were used:

- the inverter's supply voltage ( $U_{dc}$ ) was set to a low value, approx. 30V, and was increased once the IC has locked to the resonant frequency;
- the test were conducted without snubber capacitors connected in parallel to the switches;
- as loads aluminum plate, aluminum fry pan, iron plate and iron pan were used.

In the firsts practical tests, the inverter's supply voltage ( $U_{dc}$ ) was applied before the IC voltage ( $U_{cc}$ ). This was done considering that in reality the IC is supplied by step-down converter which requires some initial supply voltage before beginning operation. In that way  $U_{dc}$  reaches a value close to the maximum before IC start working.

The approach, however, lead to destruction of the lower MOSFET. The reason for the failure was investigated and is shown on Fig. 5.9. In the figure:

- $U_{cc}$  – supply voltage for the IC (+15V);
- $I_{pr}$  – current in the primary side of the transformer;
- $U_{pr}$  – primary voltage at transformer's terminals;
- Out A – voltage at the low MOSFETs gate (Q5 Fig. 5.4);
- (1) – charging of the bootstrap capacitors;
- (2) – starting of the inverter.

From the figure it can be observed that in the beginning of initialization, the IC turns on the low side switch for 10ms. Because the  $U_{dc}$  has value bigger than zero, this forces the capacitors forming the middle point (C13 and C17 Fig. 5.4) to be discharged through the

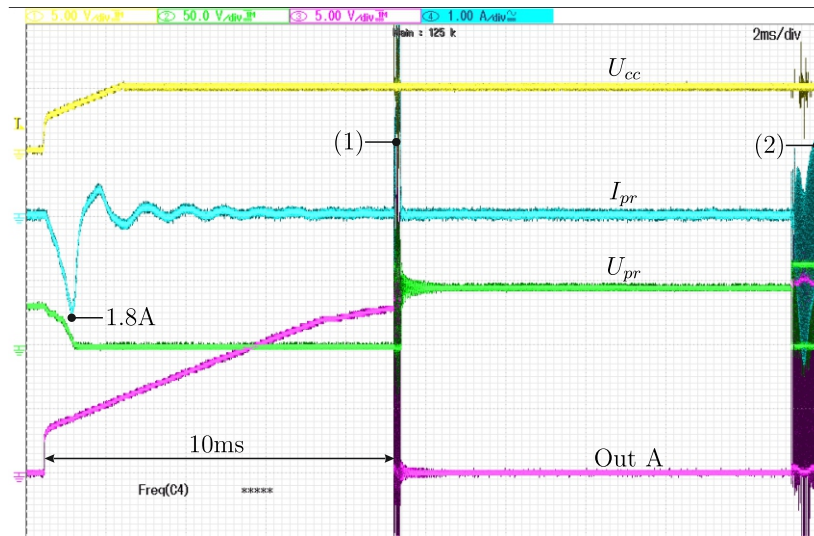


Fig 5.9. Start up in case  $U_{dc}$  is applied before  $U_{cc}$ .

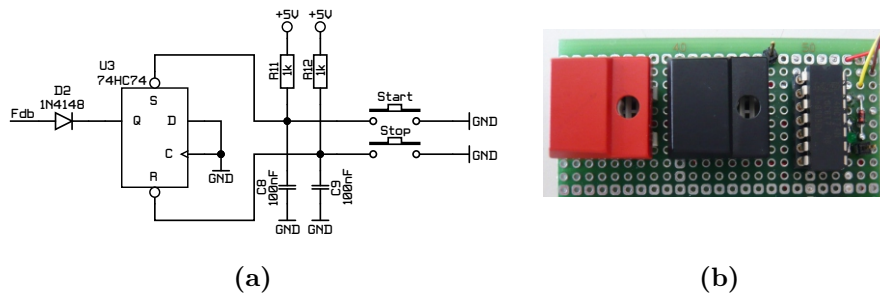


Fig 5.10. Auxiliary starting circuit. (a) schematic and (b) practical realization.

transformer and Q5. In case of high  $U_{dc}$ , this leads to saturation of the transformer and destruction of the lower switch.

The problem was solved by applying  $U_{cc}$  before  $U_{dc}$ , so that the initialization of the IC to be done with no voltage in C13 and C17. However, because the IC is designed in such a way that when no change on **Sns Fb** pin is sensed, the IC continuously turns on and off the **Out A** while a change on **Sns Fb** is sensed. Considering that application of  $U_{dc}$  when the **Out A** is high might cause instability issues and for achieving better flexibility with starting and stopping the inverter additional circuit for aiding the starting and stopping of the inverter was designed (Fig. 5.10). The new circuit was adapted to Fig. 5.3 by connecting the output of the circuit (the anode of D2) to the **Sns Fb** pin of U1. The circuit work in follow way: when  $U_{cc}$  is applied, U2 is reset by pressing the Stop button; then the output of U2 goes low and pulls down **Sns Fb** pin of U1, turning off its outputs; when Start button is preset the output of U2 goes to +5V and reverse bias D2 as the voltage on its cathode being higher than the voltage at its anode; this restores the voltage on **Sns Fb** and its normal

operation.

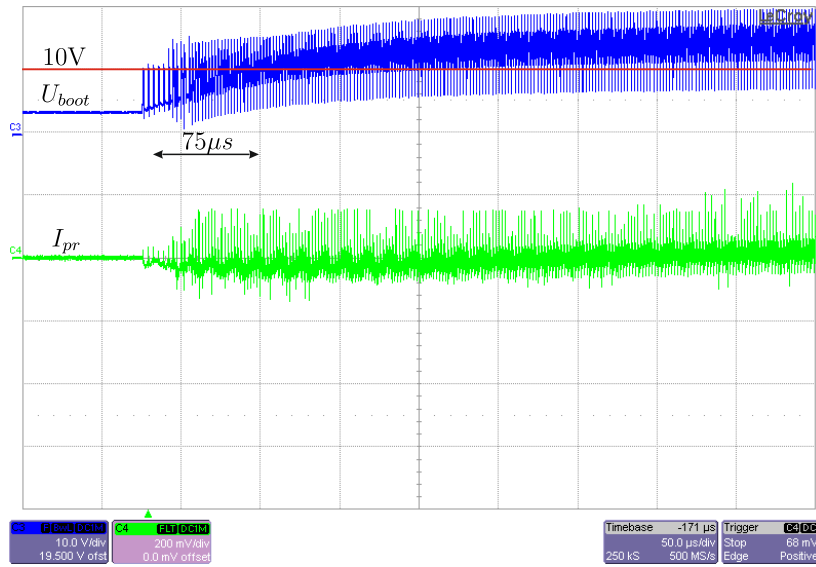


Fig 5.11. Charging of bootstrap capacitors.

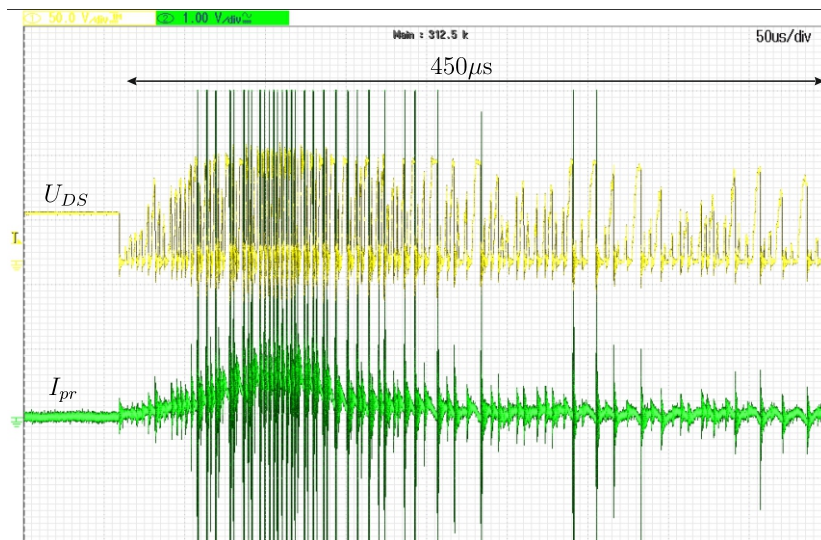


Fig 5.12. Uncontrolled switching.

Application of  $U_{cc}$  before  $U_{dc}$ , however, eliminates the charging of the bootstrap capacitors ((1) in Fig. 5.9). The charging of the capacitors, now, takes place in the beginning of the start-up of the inverter Fig. 5.11. This leads to uncontrolled switching of the inverter due

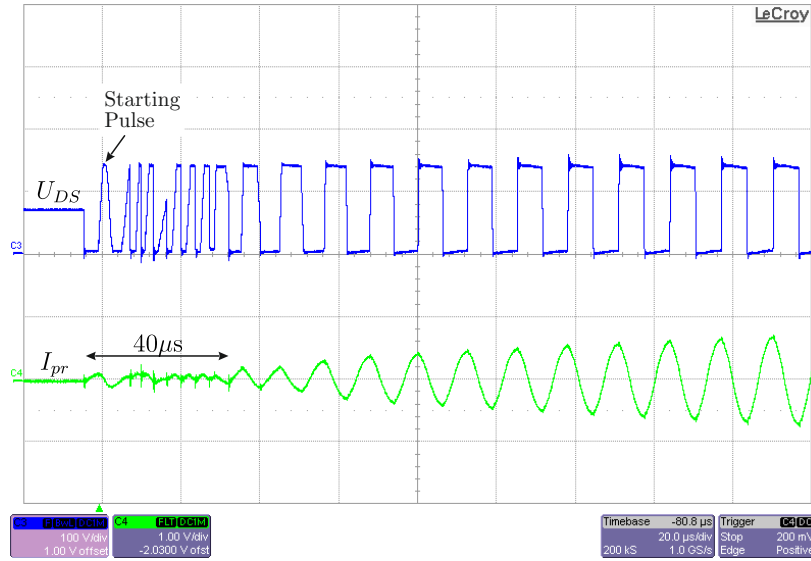


Fig 5.13. Start up with bootstrap supplied by external voltage source.

to insufficient voltage for saturation of the upper MOSFET. This causes high  $dV/dt$  in the middle point of the inverter (HV Fig. 5.4) as shown on Fig. 5.12 which leads to destruction of the gate drive stage of the IC. The uncontrolled switching, in case of connected snubbers, also leads to high power losses in the MOSFETs due to discharging of snubbers through the MOSFETs.

For avoiding the uncontrolled switching the diode D3 (Fig. 5.4) was removed and voltage source with magnitude of +15V was connected in parallel to bootstrap capacitors. The effect of changes is shown on Fig. 5.13. As can be seen from the figure the starting up have been improved significantly. However, it is also observable that in the first  $40\mu s$  the switching is still uncontrollable. The reason for this is the high voltage division required for reducing the voltage across the coil to the limits of the IC (0-5V). The effect of this is as follow. In typical DC-DC LLC resonant converter, where  $C_r$  is located in the primary side of the transformer (Fig. 1.15), and the feedback signal for calculation of the turn-off times is taken from the primary side, the turn-on of the upper switch produce a voltage jump across the primary side of the transformer equal to  $U_{dc}$ . The IC samples the jump and uses it as a reference for calculating the turn-off levels of the switches. Further, in low power application the reactive power, in comparison to active power, is low. Because of this, the voltage at the primary side of the transformer hardly exceeds  $U_{dc}$  (Fig. 4.4). In that way, if  $U_{dc} = 390V$ , the voltage division is:

$$n_{division,LLC} = \frac{U_{dc}}{Sns\ Cap_{pk}} = \frac{390}{2.5} = 156 \quad (5.11)$$

where:

$Sns\ Cap_{pk}$  – peak voltage at the **Sns Cap** pin (0-5V is peak-to-peak value).

In case of induction heating the voltage jump is reduced by turn ratio of the transformer as the feedback signal is taken from the secondary side of the transformer. Further, the high current in the secondary side leads to high voltages across the reactive components which in the current setup is 989V (5.6). This leads to voltage division of approximately:

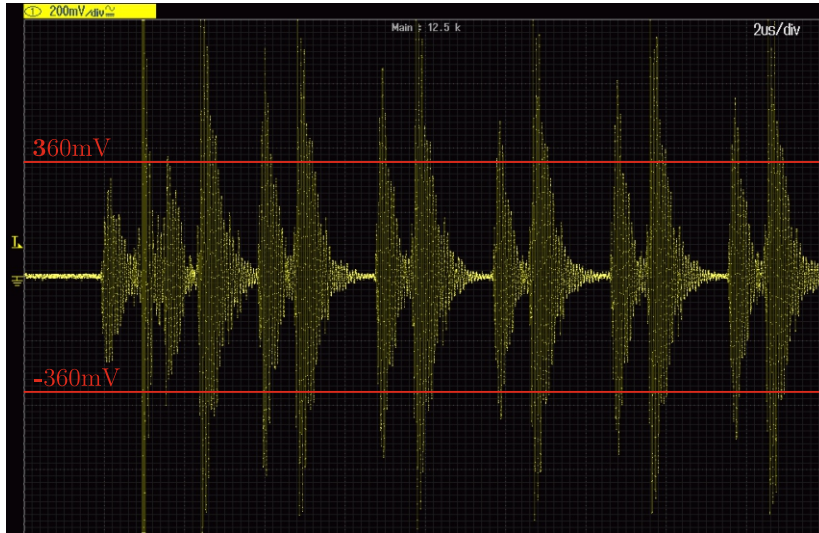


**Fig 5.14.** Noise across C19 with feedback disconnected and board placed in grounded metal box.

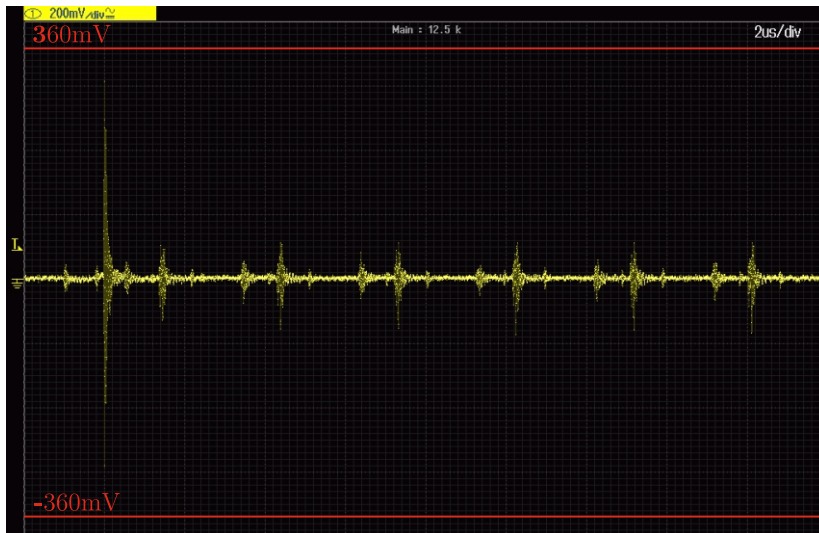


**Fig 5.15.** Voltage induced in the probe placed inside grounded metal box with probe's ground connection attached to active end of the probe.

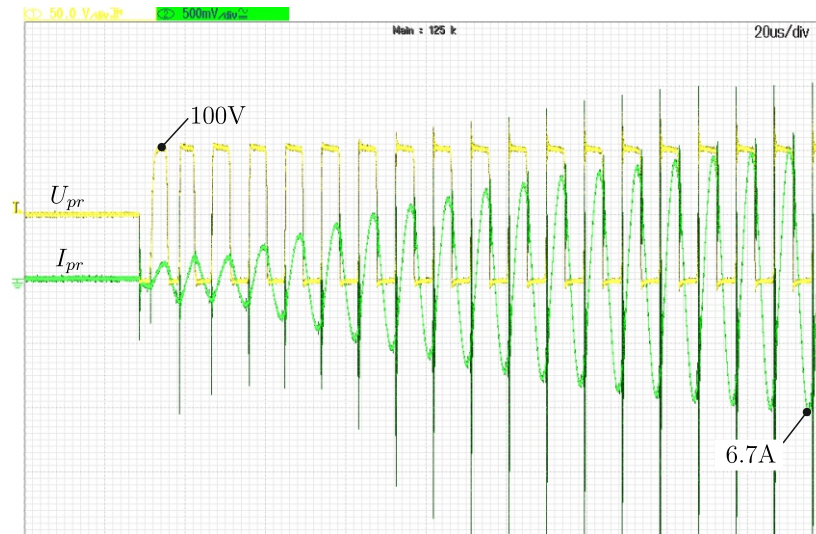


**Fig 5.16.** Start up at  $U_{dc} = 100\text{V}$  with load AL plate.

$$n_{division,IH} = \frac{\sqrt{2}U_{C_r}}{\text{Sns Cap}_{\max}} = \frac{\sqrt{2} \times 989}{2.5} = 559.5 \quad (5.12)$$

In that way, in case of DC-DC LLC resonant converter, the IC will sample and store a value of approximately 2.5V, while in case of induction heating inverter the voltage is:

$$U_{stored} = \frac{U_{jump}}{n_{division,IH}} = \frac{U_{dc}}{n \times n_{division,IH}} = \frac{390}{2 \times 559.5} = 348\text{mV} \quad (5.13)$$

where:

- $U_{jump}$  – voltage jump;
- $n$  – turn ratio in the current setup.

On Fig. 5.14 is shown the induced voltage across C19 (pin **Sns Cap**) in case the feedback cable is disconnected, the inverter is switching uncontrolled, the control board is placed in a grounded metal box and  $U_{dc} = 20\text{V}$ . From the figure it can be seen that the induced voltage in the **Sns Cap** pin exceeds the one calculated in (5.13). This will cause the IC to trigger before the resonant frequency is achieved.

The contribution of the probe to the induced noise is shown on Fig. 5.15. From the figure it can be seen that the probe's influence on the measurements is insignificant and the noise mainly is due to PCB and IC layout.

Attempts have been made for alleviation of the problem by shortening the length of the cable used for feedback signal and tightening the twisting so that the induced noise to be reduced. With this setup several test have been made by gradually increasing  $U_{dc}$ . Even though the start up, to some extent, was improved (Fig. 5.16 where it can be seen that the start up is excellent and IC starts to switch immediately at proximity of  $f_r$  without any uncontrolled switching), there were cases when the IC could not lock immediately to  $f_r$  which led to uncontrolled switching. In the latter cases a failure of either the MOSFET or IC, due to high rate of change of the voltage ( $dV/dt$ ), was observed.

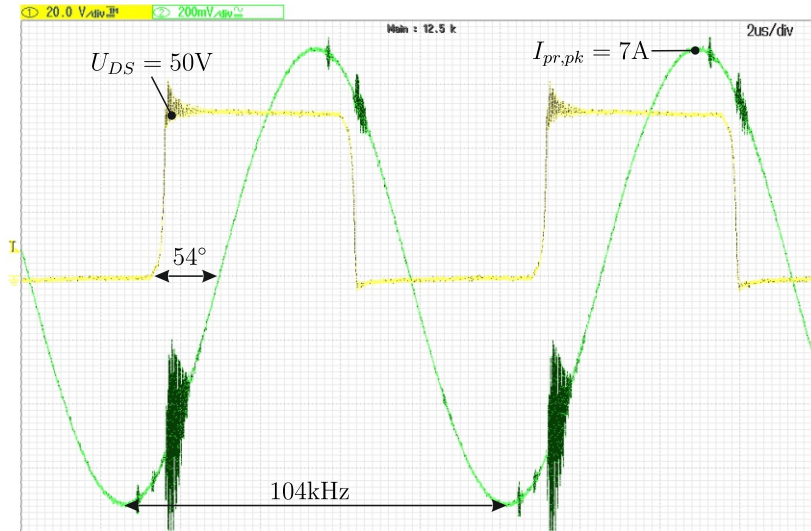


**Fig 5.17.** Continuous work with IC locked to frequency. Load AL plate,  $U_{dc} = 50V$ .

Because in the attempts for improving the start up of the inverter significant number of IC and MOSFETs were destroyed, the efforts for improving the start up were stopped. The behavior of the IC was noted as a drawback in the current prototype and efforts were concentrated on investigating the behavior of the IC at high power levels.

The steady state behavior of the IC when locked to frequency, with AL plate as load,  $U_{dc} = 50V$  is shown on Fig. 5.17. In the figure it can be seen  $f_{sw} = 104kHz$  and the angle  $\alpha = 54^\circ$ . In that way power delivered to load is  $P \approx 72W$ .

Because of high losses in the MOSFETs, due to high  $I_{pr}$ , the power in Half Bridge topology were not increased significantly. The desired power ratings were achieved with the Full Bridge topology as shown in the following section.

## 5.3 Full Bridge Inverter

### 5.3.1 Schematics and Practical Implementations

The schematic of the Full Bridge inverter is shown on Fig. 5.18. In order control board's interface to be adapted to the Full Bridge requirements, four gate drivers with floating power supply are added. The selected gate drivers, HCPL-J312, have optical isolation and peak output current of 2.5A [76] which limits the gate resistance to  $6.8\Omega$ . The floating power supplies for the gate drivers are required due to floating ground potential of upper drivers U4 and U5 (Fig. 5.18). Because the ground potential of U6 and U7 is same for both drivers, only one power supply is used. The floating power supplies, in reality, can be substituted by bootstrap network, however this will lead to uncontrolled switching in the start up of the inverter as described in §5.2.2.

The bootstrap network is moved to the control board to provide a voltage for the upper gate driver of the IC. The capacitors C10, C11 and C12 (Fig. 5.4) are replaced with a single capacitor of  $1\mu F$  due to reduced charge (current) required by the input of the gate drivers.

The capacitor C31 is used for blocking any DC voltage present in the inverters output.

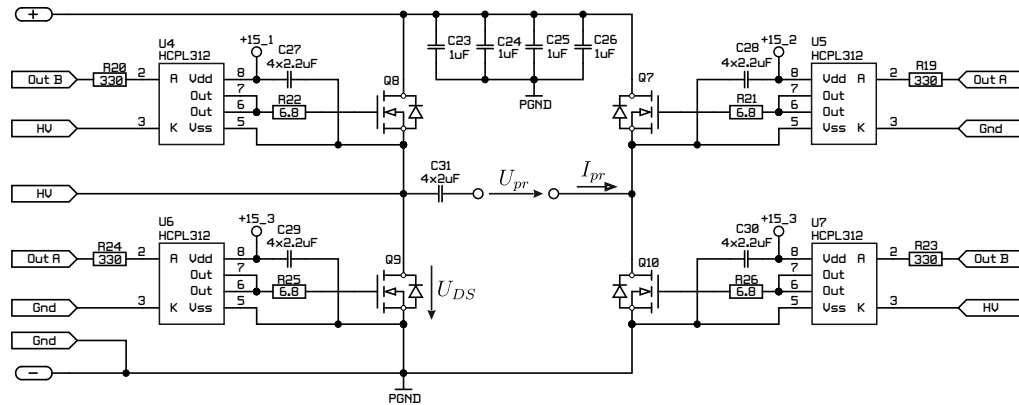


Fig 5.18. Full Bridge – schematic.

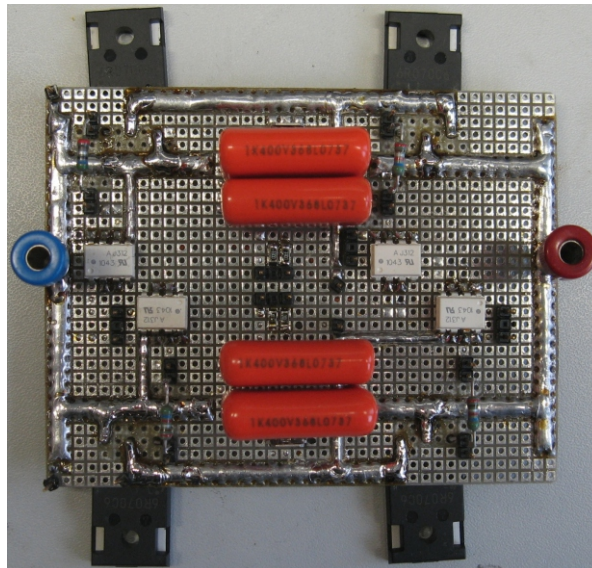


Fig 5.19. Full Bridge – practical implementation.

The value of the capacitance is selected so that the voltage drop across it to be low and the current through each capacitor to be within the limits. The primary winding of the transformer is increased to 20 turn and connected to two terminals in the diagonal of the bridge (Fig. 5.18). The secondary winding is kept 5 turns so that  $n = 4 : 1$ .

The outside view of the designed Full Bridge inverter is shown on Fig. 5.19. The schematic of the power supply stage is shown on Fig. 5.20. A picture of the practical implementation is shown on Fig. 5.21. In Fig. 5.20 the voltage regulators U11 and U14 are used for reducing the output voltage to +15VDC. The middle winding having a voltage of 10.5VAC does not require voltage regulation.

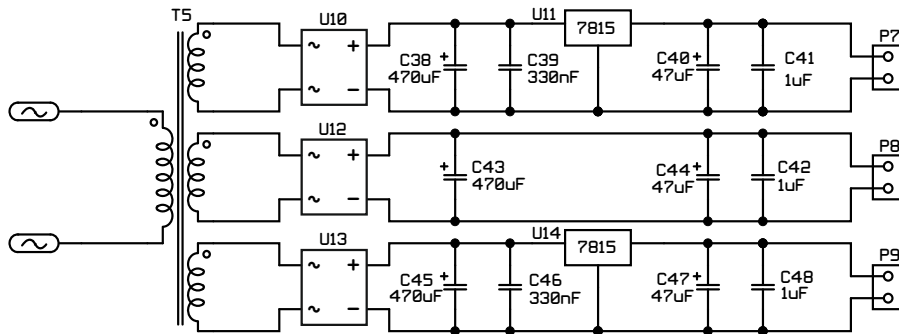


Fig 5.20. Power Supply for the Full Bridge – schematic.

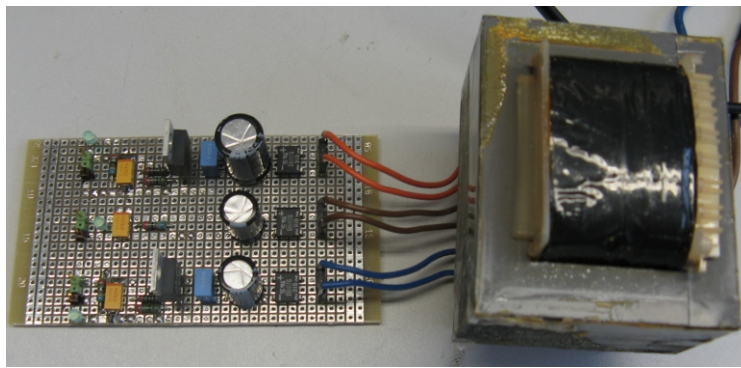


Fig 5.21. Power supply – practical design.

### 5.3.2 Achieved Practical Results

During the tests three different types of MOSFETs were used. Initially the tests were carried out with IPW60R070C6 type of MOSFETs. After that STY80NM60N and SPW47N60CFD MOSFETs were used. The reason for this is explained further in the thesis.

The start up of the inverter, with IPW60R070C6, is shown on Fig. 5.22 and Fig. 5.23. In Fig. 5.22 it can be seen that the IC located the resonant frequency immediately and the start up is excellent. However, in Fig. 5.23 the IC attempted to lock to the resonant frequency for more that 1.7s. The reason for the behavior was described in §5.2.2. Due to limited number of IC samples the problem was not investigated further.

Due to unpredictability of the start up, the starting up in all tests was performed in the following manner: first the power to the IC was applied, the circuit from Fig. 5.10 reset the IC automatically, after that the gate drivers were powered and finally  $U_{dc} \approx 30V$  was applied. In that way the the inverter was started up by pressing the start button of the starting circuit and once the IC locked to the frequency  $U_{dc}$  was increased.

With this precautions the steady state operation of the inverter in case of  $U_{dc} = 200V$ ,  $I_{dc} = 2A$  ( $P_{dc} = 400W$ ) and load of aluminum pan is shown on Fig. 5.24.

Due to destruction of one of the IPW60R070C6 MOSFETs during the test and for sake of testing and comparing different MOSFETs STY80NM60N MOSFETs were bought and

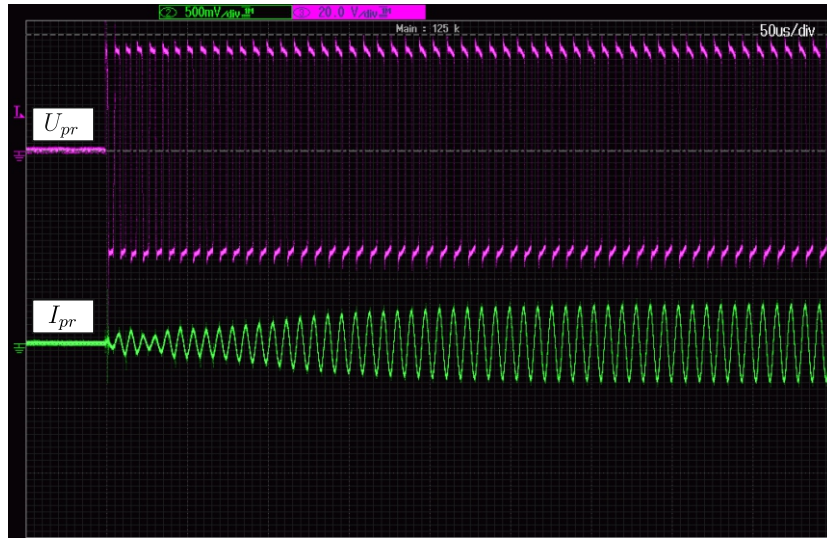


**Fig 5.22.** Good start up of the inverter in case of  $U_{dc} = 30V$ , Aluminum pan and IPW60R070C6.

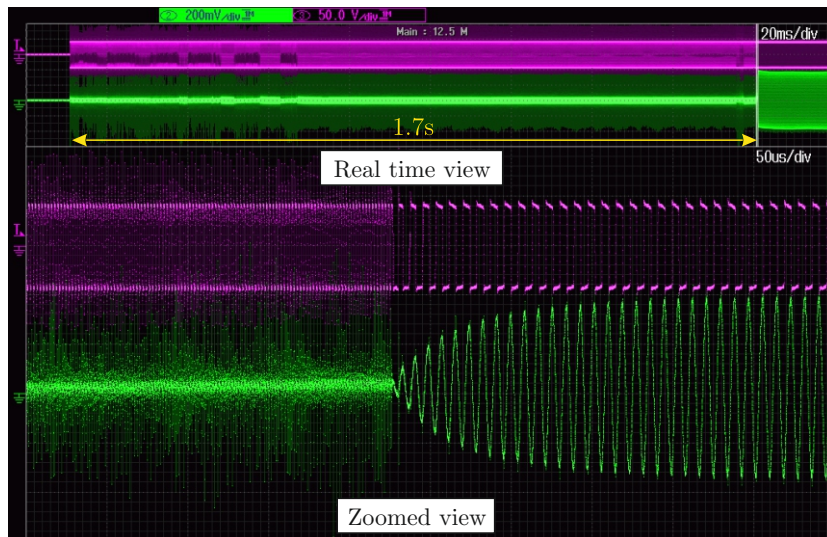


**Fig 5.23.** Bad start up of the inverter in case of  $U_{dc} = 40V$ , Aluminum pan and IPW60R070C6.

mounted in the Full Bridge board.

The parameters of the new MOSFETs together with parameters of IPW60R070C6 and SPW47N60CFD are tabulated in Table 5.1 [67], [77] and [78]. From the table it can be seen that STY80NM60N has lower  $R_{DS,on}$ , higher  $I_D$  and higher power dissipation capabilities than the used IPW60R070C6. These advantages are beneficial from a thermal point of view.

The behavior of the inverter with STY80NM60N is shown on Fig. 5.25. An enhanced

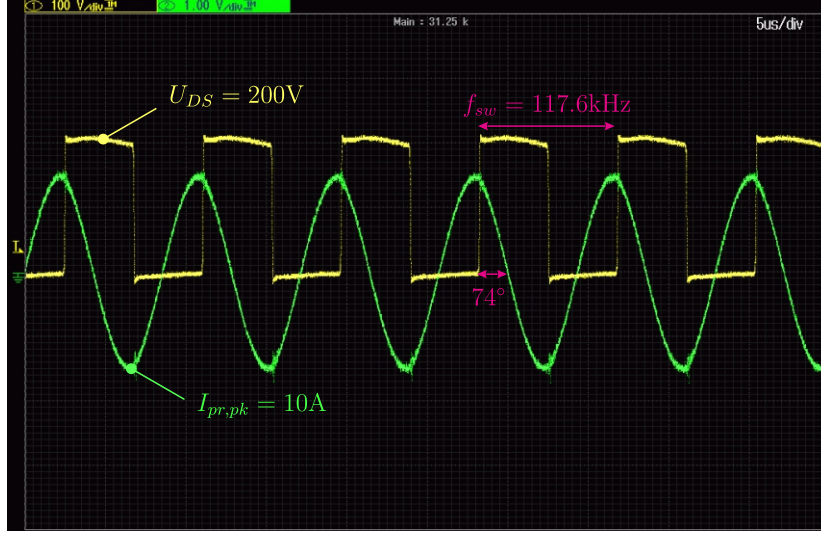


**Fig 5.24.** Steady state operation in case of  $U_{dc} = 200V$ ,  $I_{dc} = 2A$ , aluminum pan and IPW60R070C6.

**Table 5.1.** Parameters of IPW60R070C6, STY80NM60N and SPW47N60CFD used during the practical tests of the Full Bridge topology [67][77] [78].

Parameters								
Mosfet	$U_{DS}$ [V]	$I_D^{(1)}$ [A]	$R_{DS,on}^{(1)}$ [m $\Omega$ ]	$t_{d,off}$ [ns]	$t_f$ [ns]	$P$ [W]	$R_{jc}$ [ $^{\circ}C/W$ ]	Package
IPW60R070C6	600	34	103	83 <sup>(2)</sup>	5 <sup>(2)</sup>	391	0.32	TO247
STY80NM60N	600	46	60	440 <sup>(3)</sup>	200 <sup>(3)</sup>	447	0.28	MAX247
SPW47N60CFD	600	29	103	100 <sup>(4)</sup>	15 <sup>(4)</sup>	417	0.3	TO247

(1) @ 100 $^{\circ}C$

(2) @  $I_{D,test} = 25.8A$ ,  $U_{CE,test} = 400V$ ,  $R_G = 1.7\Omega$  inductive load

(3) @  $I_{D,test} = 37A$ ,  $U_{CE,test} = 300V$ ,  $R_G = 4.7\Omega$  resistive load

(4) @  $I_{D,test} = 46A$ ,  $U_{CE,test} = 400V$ ,  $R_G = 3.3\Omega$  inductive load

view is shown on Fig. 5.26. From the figures it can be seen that for short period of time the output current is stable after which it starts to decline till the IC starts to implement PDM. After this time the IC begins starting up again and the cycle is repeated. A clear reason for the instability was not found. However, during the investigation it was observed that the turn-off propagation delay  $t_{d,off}$  (the time differences between the gate voltage drops to 90% of its maximum value to the time when the  $I_D$  drops to 90% of the specified value [79]) of STY80NM60N is 440ns (Table 5.1). This, combined with the propagation delay of used gate drivers (HCPL-J312), which was measured to be approx. 250ns and is in accordance with the value specified in the datasheet [76] led to total delay of approx. 690ns.

In the current version of the IC the calculation of  $U_{Cr,high}$  and  $U_{Cr,low}$  is done by sampling the voltage at the **Sns Cap** pin short time (between 100ns and 200ns) after turn on signals

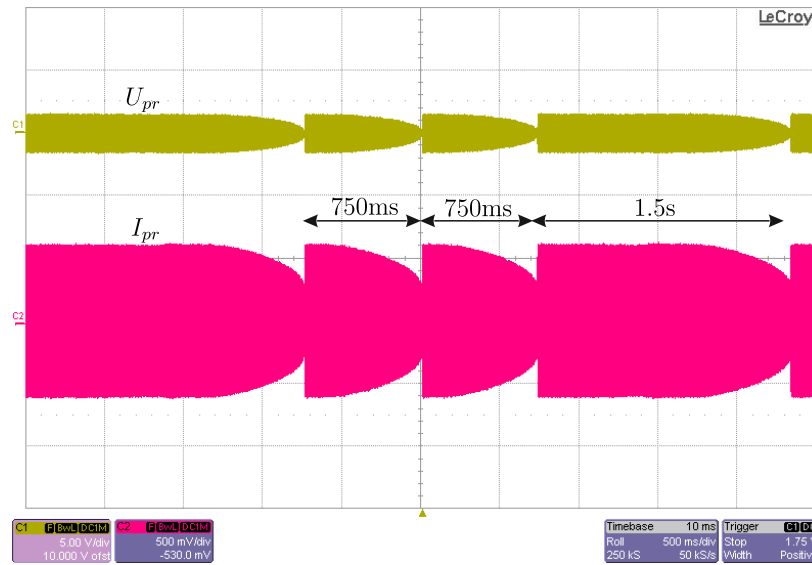


Fig 5.25. Instability with STY80NM60N MOSFETs.

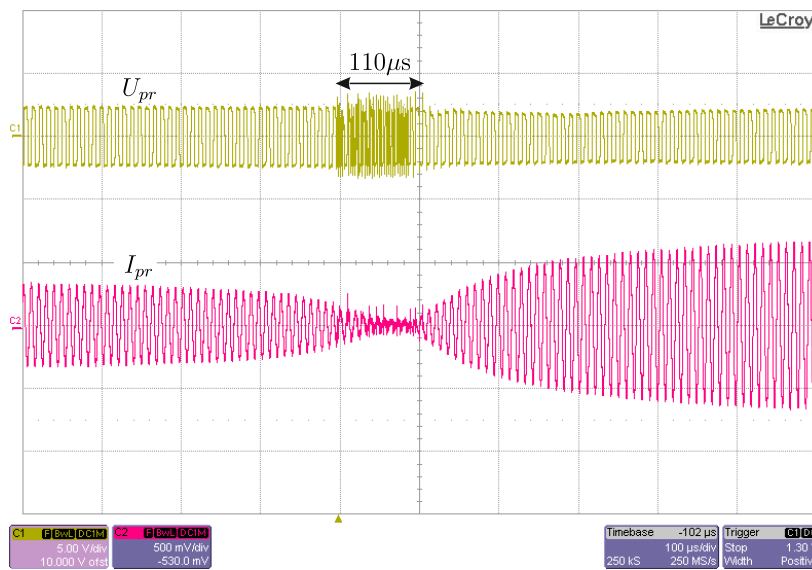


Fig 5.26. Instability with STY80NM60N MOSFETs – enhanced view.

is applied to one of the MOSFETs. The long propagation delay of 690ns forces the IC to measure incorrect value which leads to instability in the internal logic. Because of this, and considering that the problem was not present with IPW60R070C6, it was concluded that long propagation delay is the cause for the instability.

In order the propagation delay to be reduced, new MOSFETs with lower  $t_{d,off}$  have been ordered (SPW47N60CFD Table 5.1) and new gate drivers were designed (Fig. 5.27).

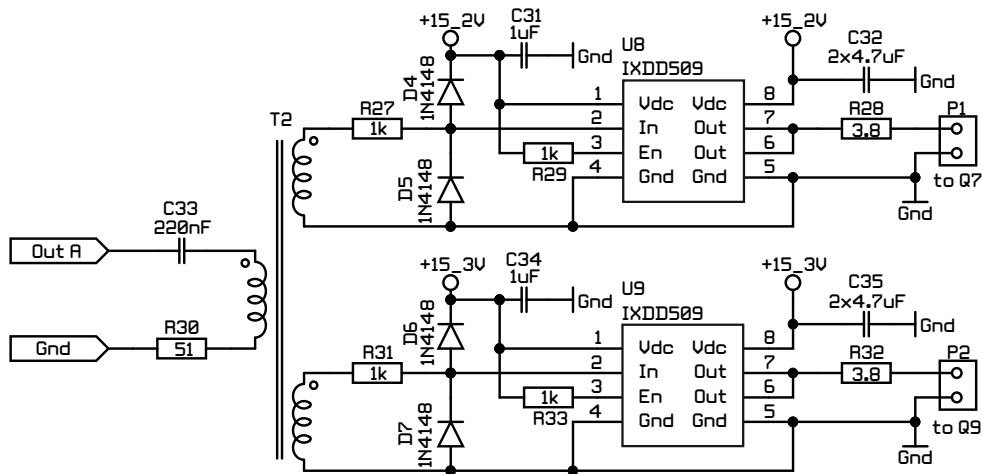


Fig 5.27. Designed new gate drivers with small propagation delay – schematic.

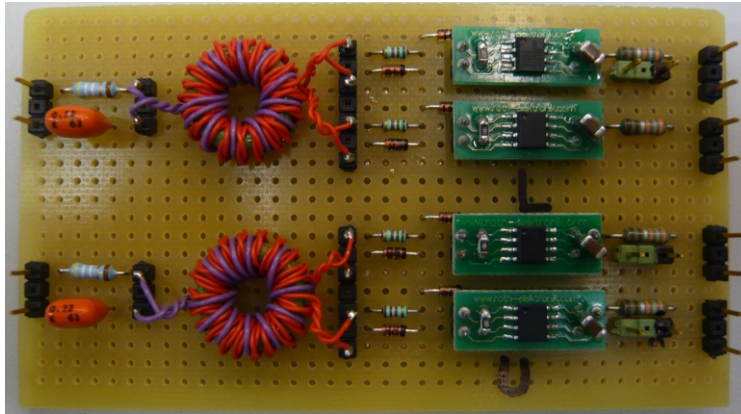


Fig 5.28. Designed new gate drivers with small propagation delay – practical realization.

As can be seen from the table the new MOSFET is faster than STY80NM60N and little bit slower than IPW60R070C6. However, its thermal parameters are slightly better than IPW60R070C6 which can help in the thermal design.

On Fig. 5.27 only one half of the drivers, driving Q7 and Q9, is shown. The other part is identical with the difference that the primary winding is connected to HV and Out B and drives Q8 and Q10. The designed drivers have output peak current of 9A which allowed the value of the gate resistance to be reduced to 3.9Ω, which is close to the recommended lowest value in the datasheet [78]. The practical implementation of the driver is shown on Fig. 5.28.

The propagation delay of the new gate drivers was measured to be 25ns at turn-on and 35ns at turn-off which is a reduction of 7 times in comparison to HCPL-J312.

The waveforms of  $U_{DS}$  and  $I_{pr}$  at maximum achieved power with the new gate drivers and SPW47N60CFD in case of  $U_{dc} = 400V$ ,  $I_{dc} = 1.48A$  and iron pan are shown on Fig. 5.29. The measured DC power was  $P_{dc} = 592W$ , which is below the desired 1.5kW. The reason

for this is the big angle between voltage and current which is approximately  $39^\circ$ . With the current version of the IC the angle could not be reduced further which limited the output power of the iron cooking vessel to  $P_{dc} = 592\text{W}$ . Also the used iron pan covered only 80% of the area of the coil. With iron pan covering the whole area of the coil the power is expected to increase.

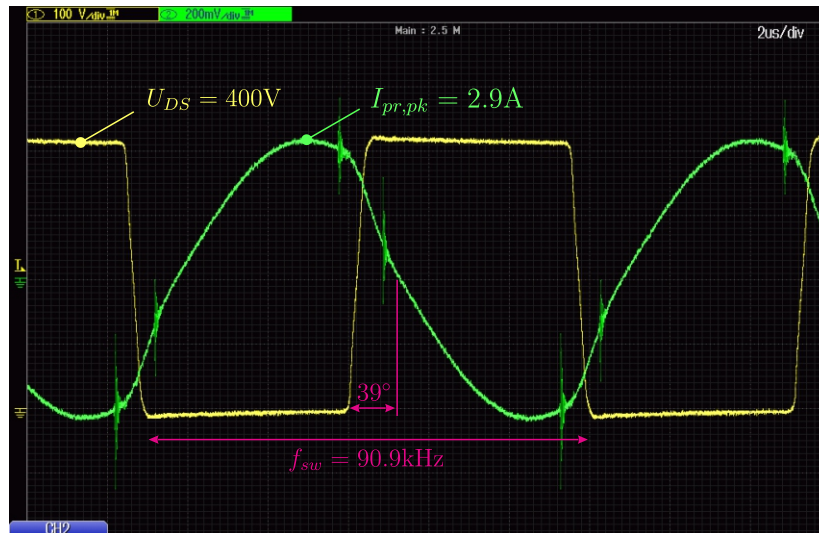


**Fig 5.29.** Achieved results in case of  $U_{dc} = 400\text{V}$ ,  $I_{dc} = 1.48\text{A}$ , iron pan and SPW47N60CFD.

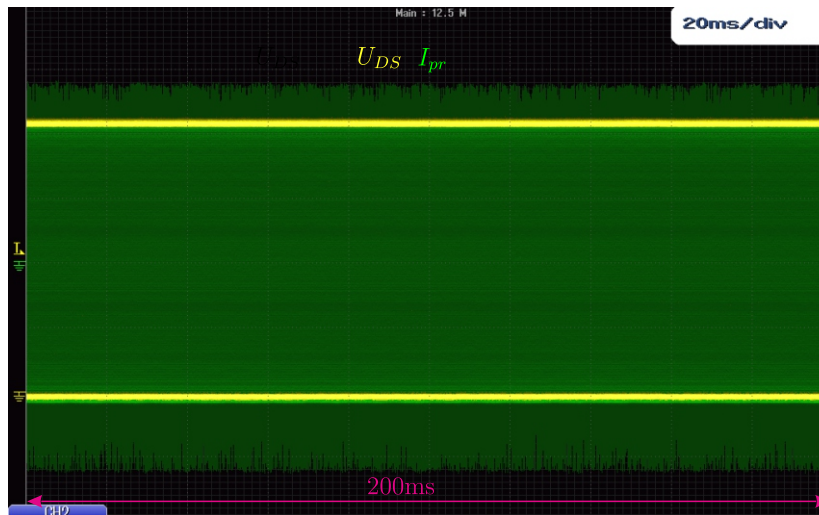


**Fig 5.30.** Achieved results in case of  $U_{dc} = 400\text{V}$ ,  $I_{dc} = 1.48\text{A}$ , iron pan and SPW47N60CFD – steady state.

For the stability of the IC with the new setup, to some extent, can be judged from the



**Fig 5.31.** Achieved results in case of  $U_{dc} = 407V$ ,  $I_{dc} = 4.1A$ , aluminum pan and SPW47N60CFD.

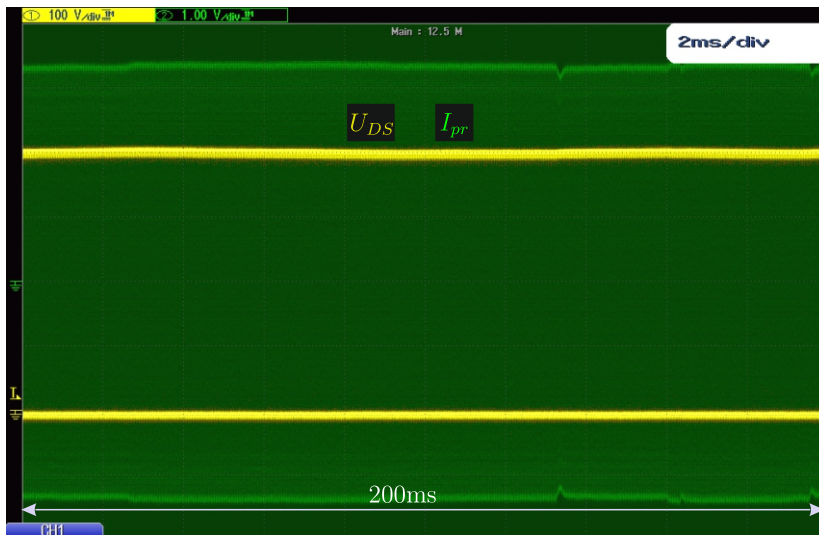


**Fig 5.32.** Achieved results in case of  $U_{dc} = 407V$ ,  $I_{dc} = 4.1A$ , aluminum pan and SPW47N60CFD – long run.

steady state waveforms shown on Fig. 5.30. From the figure it can be seen that instability issue caused by STY80NM60N is eliminated.

The current and the voltage waveforms in case of  $U_{dc} = 407V$ ,  $I_{dc} = 4.1A$  ( $P_{dc} = 1.67kW$  the maximum power which the used power supply can deliver) and Aluminum pan is shown on Fig. 5.31. From the figure it can be seen that theoretically calculated angle  $\alpha$  equals the practically measured one. The difference in the frequency is due to the bigger capacitance

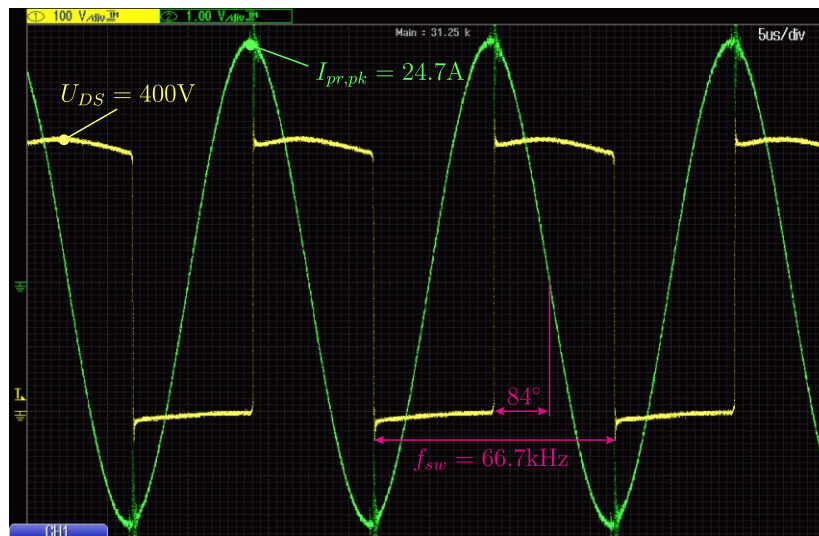


**Fig 5.33.** Waveforms of  $U_{DS}$  and  $I_{pr}$  in case of no load,  $U_{dc} = 400V$ ,  $I_{dc} = 0.9A$  and SPW47N60CFD.

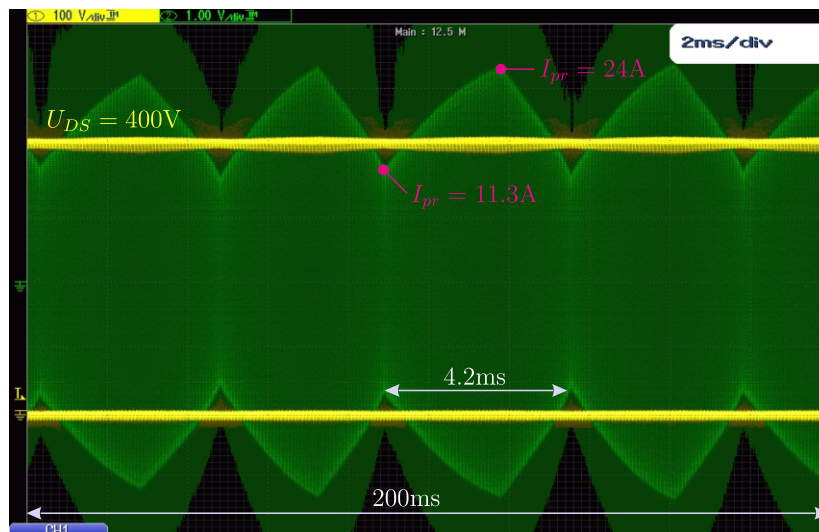


**Fig 5.34.** Instability in case of no load,  $U_{dc} = 400V$ ,  $I_{dc} = 0.9A$  and SPW47N60CFD.

used in the practical realization (106nF vs. 85nF).

The steady state operation of the inverter under aluminum load is shown of Fig. 5.32. In the figure can be seen that the there is no instability issues.

During the test it was observed that the IC is capable to limit the inverter's output current without additional circuit. This allowed the behavior of the IC and the control idea to be investigate in very high  $Q$  factor. The no load quality factor of the systems is:



**Fig 5.35.** Output waveforms in case voltage at **Sns Fb** pin reduced to 1V.  $U_{dc} = 30V$ , aluminum pan and SPW47N60CFD.

$$Q_{no,load} = \frac{2\pi f L_{coil,no,load}}{R_{coil@60kHz}} = \frac{2 \times 3.14 \times 66.6kHz \times 66\mu H}{69.11m\Omega} = 400 \quad (5.14)$$

where:

$R_{coil@66kHz}$  – AC resistance of the coil calculated by (3.16) @66kHz [ $\Omega$ ].

The waveform of  $U_{DS}$  and  $I_{pr}$  in case  $U_{dc} = 400V$  and  $I_{dc} = 0.9A$  ( $P_{dc} = 360W$ ) and no load is shown on Fig. 5.33. The steady state waveforms are shown on Fig. 5.34. From the figure it can be seen that  $I_{pr}$  fluctuates between 11.3A and 24A with  $f_{fluc} = 238Hz$ . Further investigations showed that this behavior is due to implemented control logic inside the IC used for calculation of the turn-off thresholds, rather than the control idea itself. Corroborations of this is given further in the thesis.

For controlling the power delivered to the output in the current version of the IC, as described in §5.2.1, the **Sns Fb** pin is intended to be used. However, it was found that in investigated topology, changing the voltage in the **Sns Fb** pin does not change the power. The only change which occurs is when the voltage is reduced below 1.6V. In this case, as 1.6V being the threshold at which the IC starts implementing PDM, the waveforms presented in Fig. 5.35 were observed. From the figure it can be seen that the waveforms are very distorted and inapplicable for the desired purpose.

During the test it was observed that very good power regulation can be achieved by increasing the voltage in the **Slope Gain** pin from 0V to 1.6V. In that case the IC controls the power by increasing  $f_{sw}$  and only above voltages of 1.6V the IC starts PDM and waveforms as the ones shown on Fig. 5.35 are observable.

On Fig. 5.36 are shown the achieved results when the voltage at **Slope Gain** pin is increased to 1.4V. From the figure it can be seen that the IC increased  $f_{sw}$  to 156kHz which lead to  $P_{dc} = 80W$  ( $U_{dc} = 400V$  and  $I_{dc} = 0.2A$ ).

During the test it was also observable that depending on the voltage at **Slope Gain**

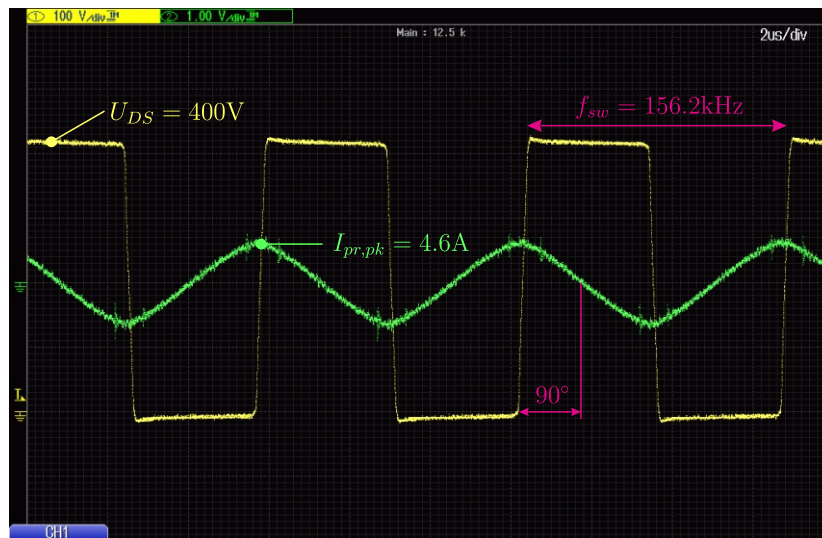


**Fig 5.36.** Power regulation in case voltage at **Slope Gain** pin increased to 1.4V.  $U_{dc} = 400\text{V}$ ,  $I_{dc} = 0.2\text{A}$ , aluminum pan and SPW47N60CFD.

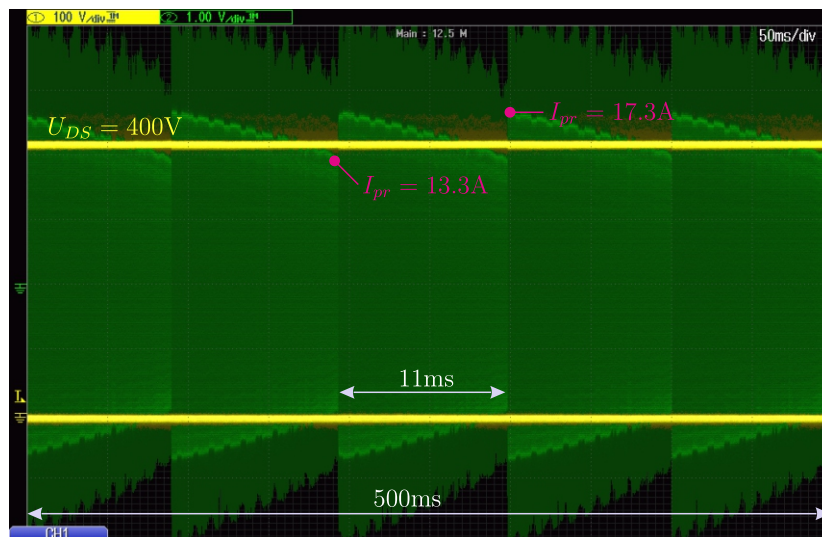


**Fig 5.37.** Instability in case of increased voltage at **Slope Gain** pin so that  $P_{dc} = 800\text{W}$ .  $U_{dc} = 400\text{V}$ ,  $I_{dc} = 2\text{A}$ , aluminum pan and SPW47N60CFD.

pin or  $U_{dc}$  the IC becomes unstable at certain voltages and stabilizes itself once the voltage is increased/decreased above/below the unstable voltage threshold. The behavior was contributed to implemented logic inside the IC and is considered also as the cause for fluctuation in Fig. 5.34.

The above mentioned unstable behavior of the IC is shown on Fig. 5.37 where the power was reduced by increasing the voltage of **Slope Gain** pin so that  $P_{dc} = 800\text{W}$ . After

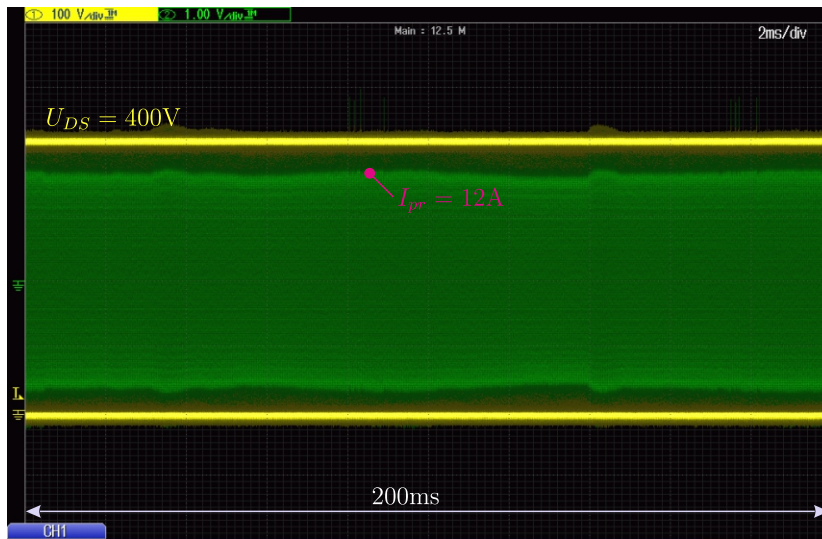


**Fig 5.38.** Stability in case of increased voltage at **Slope Gain** pin so that  $P_{dc} = 400W$ .  $U_{dc} = 400V$ ,  $I_{dc} = 1A$ , aluminum pan and SPW47N60CFD.

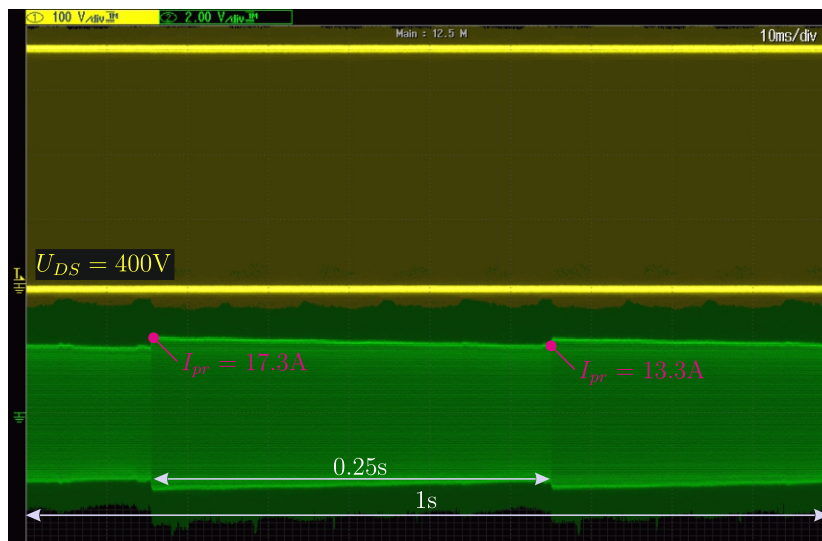


**Fig 5.39.** Instability in case of decrease of  $U_{dc}$  to 350V.  $I_{dc} = 2A$   $P_{dc} = 750W$ , aluminum pan and SPW47N60CFD.

increasing the voltage on **Slope Gain** pin so that  $P_{dc} = 400W$  the IC regain it stability (Fig. 5.38).

Example of the same behavior when  $U_{dc}$  is decreased to 350V and **Slope Gain** voltage is kept 0V is shown on Fig. 5.39. The figure can be compared with Fig. 5.32.

## 5.4 Estimation of Injected Power in the Workpiece

The easiest way of estimating the power injected in the workpiece could be done by subtracting the coil,  $C_r$ , transformer and inverter losses from measured DC power. However, the losses in the coil at load can not be measured directly as the two resistances, the coil's and the workpiece, are connected in series. One way of overcoming the problem is by estimating the coil losses with help of (3.16). However, in order the results to be accurate and reliable the accuracy of (3.16) was first practically verified. For the purpose, DC power at the input of the inverter ( $P_{dc}$ ) at no load was measured and losses due to  $C_r$ , transformer and inverter were subtracted from the measurements. After that the result was compared to the losses calculated by (3.16).

The DC power in case of no load can roughly be estimated from the measurements made in case of no load (5.33 and Fig. 5.34). According to measurements in case of  $f_{sw} = 66.7\text{kHz}$  the DC power is  $P_{dc} = 360\text{W}$ . The theoretical losses in the inverter at full power are  $96.84\text{W}$  (§3.4). The losses in single resonant capacitor at  $66.7\text{kHz}$  according to (5.8) are  $0.27\text{W}$  which makes  $65.69\text{W}$  in total. For simplicity the losses in the transformer will be neglected. In that way the losses in the coil are:

$$P_{coil,pr} = P_{dc} - P_{losses,inv} - P_{C_r,losses} = 360 - 96.84 - 65.69 = 197\text{W} \quad (5.15)$$

The theoretically calculated  $R_{ac}$  of the coil for  $66.7\text{kHz}$  is  $R_{coil@66.7\text{kHz}} = 69.85\text{m}\Omega$ . Because the operation of the IC at no load was unstable and  $I_{pr}$  fluctuates between  $I_{pr,pk,min} = 11.3\text{A}$  and  $I_{pr,pk,max} = 24\text{A}$  the average value of the currents will be used. In that way the losses in the coil are:

$$P_{coil,th} = \left( \frac{n(I_{pr,pk,min} + I_{pr,pk,max})}{2\sqrt{2}} \right)^2 R_{coil@66.7\text{kHz}} = \left( \frac{4 \times (11.3 + 24)}{2\sqrt{2}} \right)^2 69.85\text{m}\Omega = 174\text{W} \quad (5.16)$$

Comparison of result achieved by (5.15) and (5.16) shows that (3.16) gives a good approximation of the losses and can successfully be used for estimation of the injected power in the workpiece. The difference in the results can be accounted with the fact that (5.15) the maximum currents were used while in (5.16) the average one due to fluctuations.

For sake of further corroboration of the injected in the aluminum pan and verification of the approach adopted in §3.2.1.1, a practical measurement was carried out as well. In induction heating application for estimation the amount of generated power in the workpiece a specially designed calorimeters are used [10]. Due to lack of such equipment a simple approach was adopted in the thesis. The amount of power required for increasing the temperature of a body is given by [80]:

$$P = c_p m \frac{dT}{dt} + kAT^4 \quad [\text{W}] \quad (5.17)$$

where:

$c_p$  – specific heat of the body [ $\text{J}/(\text{kg} \cdot \text{K})$ ];  $c_p = 893\text{J}/(\text{kg} \cdot \text{K})$  for AL3004;

$m$  – mass of the body [ $\text{kg}$ ];  $m = 0.8\text{kg}$  for used pan;

$dT/dt$  – amount of temperature rise for unit time [ $\text{K}/\text{s}$ ];

$k$  – Stefan Boltzmann constant  $k = 5.67 \times 10^{-8} [\text{Js}^{-1}\text{m}^{-2}\text{K}^{-4}]$ ;  
 $A$  – area of the body [ $\text{m}^2$ ];  
 $T$  – temperature of the body [K].

The second part in (5.17) accounts for the radiation and convection during the heating of the body. In cases of temperatures below  $50^\circ\text{C}$  the contribution of this part of the equation is small and can be neglected as done here. In this way the temperature rise of the vessel was confined to temperatures below  $50^\circ\text{C}$  and the achieved practical results are tabulated in Table 5.2.

For  $f_{sw} = 116\text{kHz}$  and  $k = 0.85$  (Table 3.2) the calculated equivalent resistance of the aluminum pan is  $R_{ek,AL} = 0.27\Omega$ . In case of  $I_{coil} = 30\text{A}$  this gives  $P_{joule,AL} = 248\text{W}$  which is close to measured one. The difference in the analytically calculated power and the practically measured one can be contributed to inaccuracy in the temperature measurements.

**Table 5.2.** Practical evaluation of generated power in a aluminum pan.

$P_{dc}$ [W]	$dt$ [s]	$dT$ [ $^\circ\text{C}$ ]	$P_{practical}$ [W]
		(39-35)	285.76
350	10	(44-39)	357.2
		(47-44)	214.3
		(50-47)	214.3
		average	3.75
$I_{coil} = 30\text{A}, f_{sw} = 116\text{kHz}$			

The approach was carried out in low powers only due to fast temperature rise of the vessel and the high losses (fast temperature rise) in the coil<sup>2</sup>.

In that way, the estimated power delivered to load at full power with the approach described in §3.2.1.1 is:

$$P_{joule,AL,th} = \left( \frac{nI_{pr,pk}}{\sqrt{2}} \right)^2 R_{ek@116.3\text{kHz}} = \left( \frac{4 \times 22.7}{\sqrt{2}} \right)^2 0.26 = 1072\text{W} \quad (5.18)$$

where:

$R_{ek@116.3\text{kHz}}$  – equivalent resistance of the aluminum pan in case of  $f_{sw} = 116.3\text{kHz}$ .

According to measurements made on Fig. 5.31 and Fig. 5.32 and (5.18) the coil losses are:

$$P_{joule,AL,pr} = P_{dc} - P_{joule,AL,th} = 1668 - 1072 = 596\text{W} \quad (5.19)$$

The theoretically calculated losses in the coil by using (3.16) at  $f_{sw} = 116.3\text{kHz}$  and  $I_{pr} = 22.7\text{A}$  are:

<sup>2</sup>In case of coil with low losses the vessel can be filled with fluid, water as example, and the temperature rise of the fluid to be employed in the estimation.

$$P_{coil,th} = \left( \frac{nI_{pr,pk}}{\sqrt{2}} \right)^2 R_{coil@116.3kHz} = \left( \frac{4 \times 22.7}{\sqrt{2}} \right)^2 168.7m\Omega = 695.4W \quad (5.20)$$

where:

$R_{coil@116.3kHz}$  – the AC resistance of the coil at 116.3kHz.

Comparing both (5.19) and (5.18) shows that the difference in the coil losses is approximately 100W. The difference can be contributed to inaccuracy in the used equipment for measuring  $P_{dc}$  (the DC current and DC voltage was measured with the build-in voltmeter and ammeters of the power supply which are not calibrated), to fact that the coil's outer diameter was slightly bigger than the vessel which is not taken into account in (5.18) and to fact that neither (5.18) nor (5.19) take into account the effect of the second layer in the coil. However, it can be assumed that the injected power in the aluminum vessel was approx. 1kW. The higher power ratings have not been achieved due to limited power capabilities of the used DC Power Source to 1.67kW.

In that way the practical efficiency of the system with used components is:

$$\eta_{pr} \approx \frac{P_{joule}}{P_{dc}} \approx \frac{1000}{1600} \approx 0.62 \quad (5.21)$$

The low efficiency is due to employment of litz wire with large  $d_s = 0.127\text{mm}$  (AWG36) that the theoretically estimated one (Table. 3.5).



## Chapter 6

# Conclusions

In the thesis the applicability of newly developed control approach by NXP Semiconductors for control of induction cookers capable of heating all type of metals was theoretically and practically verified. The verification was carried out first by theoretical design of 1.5kW induction cooker, followed by a computer simulations and finalized by a practical design.

During the theoretical design, it was found that, in case of simple planar coil, the maximum resonant frequency is limited by the coil losses. With the selected number of turns and type of litz wire, the highest possible efficiency of heating was estimated to be 87% at 116kHz. Due to poor impedance matching between the inverters output and the resonant network, the applicability of Half Bridge topology, as a possible solution for the design, was found to be limited. It was estimated that, with state of art low  $R_{ds}$  MOSFETs, the conduction losses are excessive and impose a challenge in design of the cooling system. In case of IGBTs it was observed that the switching losses exceeding 100W per switch. A better efficiency was achieved by Full Bridge which, for the whole system, was theoretically calculated to be 81% at 6.3kVA.

The computer simulations showed that the control idea locates the resonant frequency immediately, tracks the reference power accurately without inclusion of power feedback and response to step changes very quickly with no overshoot.

During the practical verification, it was observed that the control idea is behaving in predictable manner according to simulations. However, several important issues, linked to the fact that the IC is designed for low power LLC DC-DC converters were observed. Firstly, the start up of the IC was unpredictable, leading to uncontrolled switching of the inverter and in destruction of the IC or MOSFETs. The cause of this was contributed to induced noise in the feedback pin of the IC used for controlling the turn-off of the switches. Due to nature of the problem, no means for alleviating it were found. Further, it was observed that the IC becomes unstable in case of long propagation delay in the control signals and MOSFETs. The problem was solved by design gate drivers with low propagation delay drivers and use of MOSFETs with low  $t_{pd,off}$ . Finally it was observed that, depending of the supply voltage of the inverter and the voltage level of some of the signal used for control of the power, the IC becomes unstable at certain levels. The behaviour was contributed to implemented control logic inside of the IC used for calculation of the turn-off threshold of the switches.

In general, the system performed well and was capable of delivering power of approximately 1kW in an aluminum cooking vessel. The injected power was limited by the power rating of used DC power supplies and the litz wire used in the practical design. The power

delivered to a iron vessel was estimated to be approx. 592W and was limited by the minimum phase angle of  $39^\circ$  between the voltage and current set in the IC.

# Appendix A

## Source Code for Calculation of Efficiency of Heating for Different Strand Types

```
clear all

%%%%%%%%%%%%%%%%%%%%%%%%%%%%%%%%%%%%%%%%%%%%%%%%%%%%%%%%%%%%%%%%%%%%%%%%
%inputs

n = 15; % number of turns
fmax = 500e3; % maximum frequency for calculations
FF = 0.95; % fill factor for OD
%%%%%%%%%%%%%%%%%%%%%%%%%%%%%%%%%%%%%%%%%%%%%%%%%%%%%%%%%%%%%%%%%%%%%%%%

d1 = 38e-3;
d2 = 220e-3;
ro = 4.16e-8;
ro_c = 1.68e-8;
d = (d1 + d2)/2;
w = (d2 - d1)/2;
OD = FF*w/n*1e3;
mcl = d*pi; % mean current lenght
mtl = d*pi*n; % mean turn lenght

% diameter of single strand litz wire
ds10 = 0.312;%0.257; %AWG32
ds20 = 0.229;%0.183; %AWG34
ds50 = 0.169;%0.13; %AWG36
ds100 = 0.14;%0.104; %AWG38
ds200 = 0.108;%0.081; %AWG40
ds350 = 0.093;%0.066; %AWG42
ds850 = 0.076;%0.053; %AWG44
ds14 = 0.063;%0.042; %AWG46
ds28 = 0.048;%0.033; %AWG48

% resistance single strand
rs10 = 0.3472;
rs20 = 0.6944;
```

```

rs50 = 1.417;
rs100 = 2.237;
rs200 = 3.781;
rs350 = 5.907;
rs850 = 9.425;
rs14 = 14.908;
rs28 = 23.901;
ds0 = [ds10, ds20, ds50, ds100, ds200, ds350, ds850, ds14, ds28];
rs0 = [rs10, rs20, rs50, rs100, rs200, rs350, rs850, rs14, rs28];

fplot = 1e3:50:fmax;
% generates one fig
figure
color = ['b', 'g', 'r', 'c', 'm', 'y', 'k', 'r', 'c'];

for i = 1:1:9 % for plotting several awg on one fig
    ds = ds0(i);
    rs = rs0(i);
    k = 1;
    for f = 1e3:50:fmax
        if (f >= 1e3 && f <= 350e3)
            s = 1;
        else
            s = 1.0003;
        end

        ns = (OD/(1.2*ds))^2; % number of strands
        rdc(k) = rs*mtl*1.015*1.025/ns; % dc resistance
        fr(k) = 1 + pi^2*(2*pi*f)^2*(pi*4e-7)^2*n^2*ns^2*(ds*1e-3)^6/(768*ro_c^2*w^2);
        delta = sqrt(ro/(pi^2*4e-7*f)); % skin depth work piece
        rwp(k) = ro*mcl/(w*delta); % resistance work piece
        k = k + 1;
    end

    rek = 0.78*n^2*rwp;
    rc = fr.*rdc;
    ni = rek./(rc+rek);

    % plotting plot(fplot, ni, color(i))
    hold on
end
hold off
grid
axis([1e3 fmax 0.4 0.85]);
legend('AWG30', 'AWG33', 'AWG36', 'AWG38', 'AWG40', 'AWG42', 'AWG44', 'AWG46', 'AWG48')
xlabel('f [Hz]')
ylabel('\eta')
ic = sqrt(1500./rek);
pc = ic.^2.*rc;

```

```

% figure
% plot(fplot, pc)
% grid
% xlabel('f [Hz]')
% ylabel('P [W]')

```

```

figure
plot(fplot, ic)
grid
xlabel('f [Hz]')
ylabel('I [A]')

```

## Source Code for Calculation Efficiency of Heating for AWG40, AWG42, AWG44, AWG46

```

clear all
%%%%%%%%%%%%%%%%%%%%%%%%%%%%%%%%%%%%%%%%%%%%%%%%%%%%%%%%%%%%%%%%%%%%%%%%
% inputs
fmax = 500e3; % maximum frequency for calculations
%%%%%%%%%%%%%%%%%%%%%%%%%%%%%%%%%%%%%%%%%%%%%%%%%%%%%%%%%%%%%%%%%%%%%%%%

d1 = 40e-3;
d2 = 220e-3;
ro = 4.16e-8;
ro_iron = 1.1e-7;
ro_c = 1.68e-8;

d = (d1 + d2)/2;
w = (d2 - d1)/2;

OD40 = 0.157*25.4e-3;
OD42 = 0.156*25.4e-3;
OD44 = 0.149*25.4e-3;
OD46 = 0.155*25.4e-3;

bunch = 2;
cabling = 1;
coupling = 0.78; % coupling between pan and coil

mcl = d*pi; % mean current lenght
mtl1 = d*pi*22; % mean turn lenght of the lower
mlt = mtl1;

% diameter of single strand litz wire
AWG40_bare = 0.081e-3; % meters
AWG42_bare = 0.066e-3;

```

```

AWG44_bare = 0.053e-3;
AWG46_bare = 0.042e-3;

ns40 = 1100; % number of strands
ns42 = 1380;
ns44 = 2625;
ns46 = 3525;

% resistance single strand
rs40 = 1.13/304.8; % ohm/meter
rs42 = 1.505/304.8;
rs44 = 1.21/304.8;
rs46 = 1.5/304.8;

fplot = 1e3:50:fmax;

% number of turns
n_40 = 0.95*w/OD40;
n_42 = 0.95*w/OD42;
n_44 = 0.95*w/OD44;
n_46 = 0.95*w/OD46;

% generates one fig
figure
k = 1;
for f = 1e3:50:fmax
    % dc resistance
    rdc_40 = mlt*rs40;
    rdc_42 = mlt*rs42;
    rdc_44 = mlt*rs44;
    rdc_46 = mlt*rs46;

    % ac resistace
    fr_40(k) = 1 + pi^2*(2*pi*f)^2*(pi*4e-7)^2*n_40^2*ns40^2*AWG40_bare^6/(768*ro_c^2*w^2);
    fr_42(k) = 1 + pi^2*(2*pi*f)^2*(pi*4e-7)^2*n_42^2*ns42^2*AWG42_bare^6/(768*ro_c^2*w^2);
    fr_44(k) = 1 + pi^2*(2*pi*f)^2*(pi*4e-7)^2*n_44^2*ns44^2*AWG44_bare^6/(768*ro_c^2*w^2);
    fr_46(k) = 1 + pi^2*(2*pi*f)^2*(pi*4e-7)^2*n_46^2*ns46^2*AWG46_bare^6/(768*ro_c^2*w^2);
    delta = sqrt(ro/(pi^2*4e-7*f)); % skin depth work piece alumin
    rwp(k) = ro*mcl/(w*delta); % resistance work piece alumin
    freq(k) = f; % frequency for plotting

    k = k + 1;
end

% equivalent resistance
rek_40 = n_40^2*rwp*coupling;
rek_42 = n_42^2*rwp*coupling;
rek_44 = n_44^2*rwp*coupling;
rek_46 = n_46^2*rwp*coupling;

```

```

% coil total resistance
rc_40 = fr_40*rdc_40;
rc_42 = fr_42*rdc_42;
rc_44 = fr_44*rdc_44;
rc_46 = fr_46*rdc_46;

% efficiency heating
ni_40 = rek_40./(rc_40+rek_40);
ni_42 = rek_42./(rc_42+rek_42);
ni_44 = rek_44./(rc_44+rek_44);
ni_46 = rek_46./(rc_46+rek_46);

% plotting
plot(fplot, ni_40, 'r')
hold on
plot(fplot, ni_42, 'g')
plot(fplot, ni_44, 'b')
plot(fplot, ni_46, 'k')
hold off
grid
legend('AWG40', 'AWG42', 'AWG44', 'AWG46')
xlabel('f [Hz]')
ylabel('\eta')

% ic = sqrt(1500./rek);
% pc = ic.^2.*rc;
% pc_man = ic.^2.*rc_man;

% figure
% plot(fplot, pc)
% grid
% xlabel('f [Hz]')
% ylabel('P [W]')
%figure
%plot(fplot, ic)
%grid %xlabel('f [Hz]')
%ylabel('I [A]')

```

## Source Code for Calculation Efficiency of Heating for AWG44

```

clear all

%%%%%%%%%%
% inputs
n = 20; % number of turns

```

```

fmax = 500e3; % maximum frequency for calculations
%%%%%%%%%%%%%%%%%%%%%%%%%%%%%%%%%%%%%%%%%%%%%%%%%%%%%%%%%%%%%%%%%%%%%%%%

n_iner = n - 16;
n_outer = 16;

d1 = 38e-3;
d2 = 220e-3;
ro = 4.16e-8;
ro_iron = 1.1e-7;
ro_c = 1.68e-8;

d = (d1 + d2)/2;
d_iner = (d1 + d2 - 48e-3)/2;
dsec = (d2 + d2 - 48e-3)/2;
w = (d2 - d1)/2;
w_1 = (d2 - 48e-3 - d1)/2;
w_2 = (d2 - (d2 - 48e-3))/2;

OD = 5.74e-3;
bunch = 2;
cabling = 1;
coupling = 0.78; % coupling between pan and coil

mcl = d*pi;
mcl_1 = d_iner*pi; % mean current lenght inner
mcl_2 = dsec*pi; % mean current lenght outer
mtl1 = d*pi*(n-8); % mean turn lenght of the lower
mtl2 = dsec*pi*8; % mean turn lenght for the upper 7 windings
mtl = mtl1 + mtl2;

% diameter of single strand litz wire
AWG44_bare = 0.053e-3;

% number of strands
ns44 = 2625;

% resistance single strand
rs44 = 0.747/304.8;

fplot = 1e3:50:fmax;

% generates one fig
figure

k = 1;
for f = 1e3:50:fmax
    rdc = mtl*rs44; % dc resistance
    fr(k) = 1 + pi^2*(2*pi*f)^2*(pi*4e-7)^2*n^2*ns44^2*AWG44_bare^6/(768*ro_c^2*w^2);

```

```

delta = sqrt(ro/(pi^2*4e-7*f)); % skin depth work piece alumin
delta_iron = sqrt(ro_iron/(pi^2*4e-7*f*145)); % skin depth work piece iron
rwp(k) = ro*mcl/(w*delta);
rwp_iron(k) = ro_iron*mcl/(w*delta_iron);
freq(k) = f; % frequency for plotting

k = k + 1;
end

rek = n^2*rwp*coupling*0.9;
rek_iron = n^2*rwp_iron*coupling;
rc = fr*rdc;
ni = rek./(rc+rek);

% plotting
plot(fplot, ni)
hold off
grid
legend('AWG44')
xlabel('f [Hz]')
ylabel('\eta')
ic = sqrt(1500./rek);
pc = ic.^2.*rc;

figure
plot(fplot, pc)
grid
xlabel('f [Hz]')
ylabel('P [W]')

figure
plot(fplot, ic)
grid
xlabel('f [Hz]')
ylabel('I [A]')

```

## Source Code Used in Implemented Algorithm of the Control Idea in Simulink

```

% matlab implementation of NXP control idea
function [out_aa, out_bb] = NXP(hv, vc, P, tout)

% variables
cr = 85e-9; % resonant capacitor
vdc = 2*390/4.4; % Dc voltage of the inverter

```



```

    start = 1;
elseif(start)
    out_a = 0;
    start = 0;
end

% rise comparator
hvh1 = hvh;
if(hv > 370)
    hvh = 1;
else
    hvh = 0;
end

% fall comparator
hvl1 = hvl;
if(hv < -370)
    hvl = 1;
else
    hvl = 0;
end

% ----- edge detectors -----
% rising edges
if(hvh && ~hvh1)
    hv_rise = 1;
else
    hv_rise = 0;
end

% falling edges
if(hvl && ~hvl1)
    hv_fall = 1;
else
    hv_fall = 0;
end

% ----- switching frequency -----
if(hv_fall) % turn on
    freq = 1/t; % calculate the frequency of the switching
    time_old = tout;
else
    t = tout - time_old;
end

% calculation of delta Ucr
v1 = P/(freq*cr*vdc);

if(~start)

```

```
% ----- out a turn on -----
if(hv_rise && ~out_b)
    out_a = 1;
elseif(vc < (vdc - v1)/2)
    out_a = 0;
end

% ----- out b turn on -----
if(hv_fall && ~out_a)
    out_b = 1;
elseif(vc > (v1 - vdc)/2)
    out_b = 0;
end
end

% output signals
out_aa = out_a;
out_bb = out_b;
```

# Bibliography

- [1] Lawrence Berkley National Laboratory, “Technical support document for residential cooking products,” *Potential Impact of Alternative Efficiency Levels for Residential Coking Products*, vol. 2, p. 48.
- [2] P. H. Peters, “A portable cool-surface induction cooking appliance,” *IEEE Transaction on Industry Applications*, vol. IA-10, Issue 6, pp. 814 – 822, 1974.
- [3] Panasonic, “KY-HS30AP,” induction Cooktop. [Online]. Available: [www.panasonic.hk/ha/english/feature\\_378.aspx](http://www.panasonic.hk/ha/english/feature_378.aspx)
- [4] Browne-Halco, “Profesional cookware,” pg. 3.
- [5] National Electronic Alloys Inc., “Stainless Steel 300 Series.” [Online]. Available: [www.nealloys.com/300\\_series\\_alloy.php](http://www.nealloys.com/300_series_alloy.php)
- [6] N. Education, “Conductivity and resistivity values for aluminum and alloys,” 2002.
- [7] Field Precision, “Saturation curves for soft magnetic materials.” [Online]. Available: [www.fieldp.com/magneticproperties.html](http://www.fieldp.com/magneticproperties.html)
- [8] “Grey Cast Iron ASTM40.” [Online]. Available: [www.substech.com/dokuwiki/doku.php?id=grey\\_cast\\_iron\\_astm\\_40](http://www.substech.com/dokuwiki/doku.php?id=grey_cast_iron_astm_40)
- [9] AK Steel, “Product data sheet 304/304l stainell steel,” 2007. [Online]. Available: [www.aksteel.com](http://www.aksteel.com)
- [10] S. Zinn and L. Semiatin, *Elements of Induction Heating. Design, Control and Applications*, 1st ed. ASM International, 1988.
- [11] Kristen, “Stainless Steel: All About Food Grade 304, 18/8 and 18/10,” 09 2011. [Online]. Available: <http://mightynest.com/blog/stainless-steel-all-about-food-grade-304-188-and-1810>
- [12] J. R. Davids, *Aluminum and Aluminum Alloys*. ASM International, 1993.
- [13] J. Davids, *Cast Iron*. ASM International, 1996.
- [14] H. T. Angus, *Cas Iron: Physical and Engineeirng Properties*, 2nd ed. Butterworths, 1976, iISBN: 0-408-70688-0.
- [15] H. Angus, *Physical and Engineering Properties of Cast Iron*, 1st ed. British Cast Iron Research Assosiation, 1960.

- [16] V. S. Popov and S. A. Nikolaev, *Obshtaya Elektrotehnika s osnovami Elektroniki [Common Electrical Engineering with Electronics Background]*, 1st ed. Energiya, 1972, translated from Russian.
- [17] E. J. Dede, J. Jordan, K. Estme, J. Espi, and S. Casans, "Behaviour of series and parallel resonant inverters for induction heating in short-circuit conditions," *Power Electronics and Motion Control Conference. Proceedings. IPEMC 2000. The Third International*, vol. 2, pp. 645–649, 2000.
- [18] E. Dede, J. Jordan, J. Gonzalez, J. Linares, V. Esteve, and E. Maset, "Conception and design of a parallel resonant converter for induction heating," *Sixth Annual Conference and Proceedings on Applied Power Electronics Conference and Exposition. APEC '91.*, vol. 1, pp. 38–44, 1991.
- [19] U. Borisov, D. Lipatov, and U. Zorin, *Elektrotehnika [Elektrotechnics]*, 2nd ed., B. Meniyshov, Ed. Energoatomizdat, 1985, translated from Russian.
- [20] E. J. Dede, V. Esteve, J. V. Gonzalez, J. Garcia, and E. M. D. Ramirez, "A 12 kW/ 250 kHz Series Resonant Converter for Induction Heating," *AFRICON '92 proceedings, 3rd AFRICON Conference*, vol. 1, pp. 91–94, 1992.
- [21] E. J. Dede, V. Esteve, J. G. A. E. Navarro, E. Masedz, and E. Sanchis, "Analysis of Losses and Thermal Design of High-Power, High-Frequency Resonant Current Fed Inverters For Induction Heating," *International Conference on Industrial Electronics, Control, and Instrumentation, 1993. Proceedings of the IECON '93*, vol. 2, pp. 1046–1051, 1993.
- [22] A. M. Manev, "Design and Simulation of Digital PLL for Control of Series Resonant Inverters," *Advances in Bulgarian Science*, vol. 4, pp. 13–18, 2009.
- [23] N. S. Bayndtr, . Kukrer, and M. Yakup, "DSP-based PLL-controlled 50-1 00 kHz 20 kW high-frequency induction heating system for surface hardening and welding applications," *IEE Proceedings. Electric Power Applications*, vol. 150, pp. 365–371, 2003.
- [24] J. Tian, G. Berger, M. S. T. Reimann and, and J. Petzoldt, "A Half-Bridge Series Resonant Inverter for Induction Cookers using a Novel FPGA-based Control Strategy," *2005 European Conference on Power Electronics and Applications*, vol. 1, pp. 9pp. – P.9, 2005.
- [25] E. Dede, J. V. Gonzalez, J. Linares, J. Jordan, V. Esteve, and J. Carrasco, "Conception of parallel resonant transistorized generators for induction heating," *AFRICON '92 proceedings, 3rd AFRICON Conference*, vol. 1, pp. 390–393, 1992.
- [26] S. Zeman, A. Osilov, and A. Yushkov, "Analiz impulsnon-modulacionniyh sposobov regulirovaniya posledovatelnogo rezonansnogo invertora [analysis of pulse-modulated means for regulation in series resonant inverter]," *Silovaya Elektronika*, vol. 4, pp. 88–105, 2007.
- [27] S. Llorente, F. Monterde, J. Burdio, and J. Acero, "A comparative study of resonant inverter topologies used in induction cookers," *Applied Electronics Conference and Exposition, 2002. APEC 2002. Seventeenth Annual IEEE*, vol. 2, pp. 1168 – 1174, 2002.
- [28] S. Danev, *Teoria na Avtomatichnoto upravlienie. Lineyni sistemi [Theory of Automatic Control. Linear Systems]*. Tehnika Sofia, 1987, translated from Bulgarian.

- [29] S. Buso and P. Mattavelli, *Digital Control in Power Electronics*. Morgan & Claypool, 2006.
- [30] M. Hadjiyski, *Avtomatizacia na Tehnologichni procesi. [Automation of Technological processes]*. Tehnika Sofia, 1989, translated from Bulgarian.
- [31] K. Velev, *Teoria na Avtomatichnoto Upravlienie. [Theory of Automatic Control.]*. Mar-tilen Sofia, 1993, translated from Bulgarian.
- [32] Holtek, “Using the HT46R12A in an Induction Cooker,” July 2007.
- [33] N. J. Park, D. Y. Lee, and D. S. Hyun, “Study on the new control scheme of class-E in-verter for IH-Jar application with clamped voltage characteristics using pulse frequency modulation,” *Electrical Power Applications*, vol. 1, pp. 433 – 438, 2007.
- [34] L. Meng, K. W. E. Cheng, and K. W. Chan, “Systematic approach to high-power and energy-efficient industrial induction cooker system: Circuit design, control strategy, and prototype evaluation,” *IEEE Transactions on Power Electronics*, vol. 26, pp. 3754–3765, 2011.
- [35] I. Hirota, H. Omori, K. A. Chandra, and M. Nakaoka, “Practical evaluations of single-ended load-resonant inverter using application specific IGBT & driver IC for induction-heating appliance,” *Power Electronics and Drive Systems*, vol. 1, pp. 531 – 537, 1995.
- [36] Infineon Technologies, “IHW30N160R2,” November 2009, datasheet.
- [37] On Semiconductor, “NGTB40N120IHLWG,” September 2012, datasheet.
- [38] Fairchild Semiconductor, “High-Efficiency IGBTs for Induction Heating,” 2013.
- [39] Infineon Technologies, “IGBT Selection Guide. Common IGBT Applications and Tech-nologies,” August 2012.
- [40] H. Yonemori and M. Kobayashi, “On the heating characteristic and magnetic flux of a double-coil drive type induction heating cooker,” *IEEE Industrial Electronics, IECON 2006 - 32nd Annual Conference on*, vol. 1, pp. 2488 – 2493, 2006.
- [41] F. Monterde, P. Hernandez, J. M. Burdio, and J. R. Garcia, “Unipolar voltage-cancellation control of resonant inverters for induction cooking appliances,” *Industrial Electronics Society. IECON '98. Proceedings of the 24th Annual Conference of the IEEE.*, vol. 2, pp. 820 – 824, 1998.
- [42] D. Puyal, C. Bernal, J. M. Burdio, J. Acero, and I. Millan, “High frequency inverter design for large-signal characterization of domestic induction heating load,” *IEEE In-dustrial Electronics, IECON 2006 - 32nd Annual Conference*, vol. 1, pp. 2706 – 2711, 2006.
- [43] G. I. Atabekov, *Teoreticheskie Osnoviy Elektrotehniki. Lineynij Elektricheski Cipi [The-oretical Fundamentals of Electrical Engineering. Linear Electrical Circuits]*. lany, 2009, translated from Russian.
- [44] J. W. Nilsson and S. A. Riedel, *Electric Circuits*, 9, Ed. Prentice Hall, 2011.
- [45] R. E. Haimbaugh, *Practical Induction Heat Treating*, 1st ed. ASM International, 2001.

- [46] M. Paraliev, "Air-core transformer electrical modeling," Jan 2007, Paul Scherrer Institute - Villiger.
- [47] L. Meng, K. Cheng, and P. Luk, "Field analysis of an induction cooker with square 9-coil system by applying diverse exciting patterns," *6th IET International Conference on Power Electronics, Machines and Drives (PEMD 2012)*, pp. 1–5, 2012.
- [48] L. C. Meng, K. Cheng, and K. Chan, "Heating performance improvement and field study of the induction cooker," *3rd International Conference on Power Electronics Systems and Applications, 2009. PESA 2009*, pp. 1–5, 2009.
- [49] L. C. Meng, K. W. E. Cheng, and S. L. Ho, "Multicoils design for induction cookers with applying switched exciting method," *IEEE Transactions on Magnetics*, vol. 48, pp. 4503 – 4506, 2012.
- [50] P. Kalantov and L. Cejtin, *Raschet Induktivnostej [Calculations of Inductions]*, 3rd ed., N. Tihodiev, Ed. Leningrad: Energoatomizdat, 1986, translated from Russian.
- [51] HM Wire International, Inc. . [Online]. Available: [www.litz-wire.com](http://www.litz-wire.com)
- [52] T. Tanaka, "A new induction cooking range for heating any kind of metal vessels," *IEEE Transactions on Consumer Electronics*, vol. 35, pp. 635–641, 1989.
- [53] W. Conel and T. McLyman, *Transformer and Inductor Design Handbook*, 3rd ed. Marcel Dekker, Inc., 2004.
- [54] R. W. Erickson and D. Maksimovic, *Fundamentals of Power Electronics*. Kluwer Academic Publisher, 2001.
- [55] HM Wire International, Inc., "Formulas for the OD Standart Litz Wire Configuration."
- [56] Elektrisola, "Techical data for enamalled coper wire, based on IEC60317," Januvarly 2012.
- [57] New England Litz Technologies, "Litz Wire Technical Information," April 2003.
- [58] C. R. Sullivan, "Optimal choice for number of strands in a litz-wire transformer winding," *IEEE Transactions on Power Electronics*, vol. 14, pp. 283–291, 1999.
- [59] New England Wire Technologies. [Online]. Available: [www.newenglandwire.com](http://www.newenglandwire.com)
- [60] Celem Power Capacitors Ltd, "CSP 120/200 Conduction Cooled Capacitors," April 2012.
- [61] Infineon Technologies, "IPW65R037C6 Datasheet," October 2011, rev. 02.
- [62] Fairchild Semiconductor, "FGH60N60SMD datasheet," March 2011, rev. A1.
- [63] Infineon Technologies. [Online]. Available: [www.infineon.com](http://www.infineon.com)
- [64] Fairchild Semiconductors. [Online]. Available: [www.fairchildsemi.com](http://www.fairchildsemi.com)
- [65] Panasonic, "PGS Graphite Sheet EYGA091203RV," December 2011.
- [66] R. Naayagi, R. Shuttleworth, and A. Forsyth, "Investigating the effect of snubber capacitor on high power igtb turn-off," *1st International Conference on Electrical Energy Systems (ICEES) 2011*, vol. 1, pp. 50–55, 2011.

- [67] Infineon Technologies, "IPW60R070C6 datasheet," Februari 2010, rev. 2.1.
- [68] A. Device, "ADuM4223/ADuM3223, Isolated Precision Half-Bridge Driver," 2012-2013, rev. A.
- [69] Plexim Inc., "Plecs." [Online]. Available: [www.plexim.com](http://www.plexim.com)
- [70] Ferroxcube, "Data Handbook Soft Ferrites and Accessories," September 2008. [Online]. Available: [www.ferroxcube.com/appl/info/HB2009.html](http://www.ferroxcube.com/appl/info/HB2009.html)
- [71] Fairchild Semiconductors, "Design and application guide of bootstrap circuit for high-voltage gate-drive ic," Application Note AN-6067, August 2008.
- [72] Philips Semiconductor, "BD135, BD137 and BD139 NPN power tranzistors," April 1999.
- [73] Vishay BCcomponents, "AC and Pulse Metallized Polypropylene Film Capacitors KP/MKP Radial Lacquered Type," August 2010.
- [74] Epcos, "Film Capacitors. General Technical Information," May 2009.
- [75] B. W. Williams, *Principles and Elements of Power Electronics. Devices, Drivers, Applications, and Passive Components*. Barry W Williams, 2006.
- [76] Avago Technologies, "HCPL-3120/J312, HCNW3120 2.5 Amp Output Current IGBT Gate Drive Optocoupler," July 2008.
- [77] STMicroelectronics, "STY80NM60N datasheet," July 2011, rev. 6.
- [78] Infineon Technologies, "SPW47N60CFD datasheet," April 2008, rev. 1.3.
- [79] Advanced Power Technologies, "Application Note APt-0403," March 2006, rev. B.
- [80] V. Rudnev, D. Loveless, R. Cook, and M. Black, *Handbook of Induction Heating*, 1st ed., M. I. and B. G., Eds. Marcel Dekker, Inc., 2003.